

***In Vivo* Optical Projection Tomography in Biological Model
Organisms**

***In vivo* Optische Projectie Tomografie in biologische
modelorganismen**

Proefschrift

ter verkrijging van de graad van doctor aan de

Erasmus Universiteit Rotterdam

op gezag van de

rector magnificus

Prof.dr. H.G. Schmidt

en volgens besluit van het college voor promoties.

De openbare verdediging zal plaatsvinden op

Vrijdag 15 januari 2010 om 9.30 uur

Door

Heiko Meyer

geboren te Hameln (Duitsland)



Promotiecommissie

Promoter: Prof.dr. F.G. Grosveld

Overige leden: Dr. N.J. Galjart
Dr. A.B. Houtsmuller
Prof. dr. C. Wyman

Copromoter: Dr. J. Ripoll

TABLE OF CONTENTS

TABLE OF FIGURESiii

LIST OF ABBREVIATIONS..... vi

1 INTRODUCTION..... 1

 1.1 TOMOGRAPHIC IMAGING 1

 1.2 AIM AND STRUCTURE OF THIS THESIS 2

 1.3 OTHER LINEAR EXCITATION BASED 3D MICROSCOPY TECHNIQUES 4

 1.3.1 CONFOCAL MICROSCOPY 4

 1.3.2 CONFOCAL THETA MICROSCOPY 6

 1.3.3 SPIM AND ULTRAMICROSCOPY 7

 1.4 DEVELOPMENT OF MICROSCOPY AND TOMOGRAPHY 10

 1.5 OPT IN THE PAST, PRESENT AND FUTURE 13

2 THEORY 16

 2.1 BEAM PROPAGATION IN ABSORBING MEDIA..... 16

 2.2 THE RADON TRANSFORM 21

 2.3 OPTICAL RESOLUTION..... 31

 2.4 FREQUENCY WINDOWS..... 38

 2.5 SAMPLE ILLUMINATION..... 40

3 MATERIALS AND METHODS 43

 3.1 OPT EXPERIMENTAL SETUP..... 43

 3.2 CAMERA 47

 3.3 FLUORESCENT FILTERS..... 48

 3.4 SAMPLE PREPARATION 50

 3.5 ABSORPTION COEFFICIENT..... 52

 3.6 DATA RECONSTRUCTION..... 53

4 RESULTS AND DISCUSSION 61

 4.1 DROSOPHILA MELANOGASTER 61

TABLE OF CONTENTS

4.2	<i>CAENORHABDITIS ELEGANS</i>	66
4.3	<i>PARHYALE HAWAIENSIS</i>	71
5	CONCLUSIONS AND FUTURE ASPECTS	76
5.1	<i>CONCLUSION</i>	76
5.2	<i>FUTURE APPLICATIONS</i>	77
	ACKNOWLEDGEMENTS	79
	REFERENCES	81
	BLUEPRINTS	87

TABLE OF FIGURES

Fig. 1.1.1: The principle of Optical Projection Tomography	2
Fig. 1.3.1: Principle of Confocal Microscopy.....	5
Fig. 1.3.2: Principle of Confocal Theta Microscopy.....	7
Fig. 1.3.3: Principle of Selective Plane Illumination Microscopy.....	8
Fig. 1.3.4: Principle of Ultramicroscopy.....	9
Fig. 2.1.1: Illustration of Eq. (1)	16
Fig. 2.1.2: Graphic representation of <i>Beer's law</i>	20
Fig. 2.2.1: Concept of a ray integral as defined in Eq. (22).....	21
Fig. 2.2.2: Parallel beam projection	22
Fig. 2.2.3: Illustration of the geometrical interpretation of Eq.26	23
Fig. 2.2.4: Geometry and notation for the determination of a two- dimensional object function $f(\rho)$ from parallel projections.	26
Fig. 2.2.5: Illustration of the notation to reconstruction of planar cross-sections of the object function $f(\rho)$	28
Fig. 2.2.6: Schematic of corresponding $I(P)$ of each pixel in a CCD raw (which implies the corresponding radon transform) for a light sheet based illumination.	29
Fig. 2.2.7: Backprojection for different number of projections.....	30
Fig. 2.3.1: Diffraction pattern of a laser beam from a circular aperture	31
Fig. 2.3.2: Dependence of the numerical aperture from the variation of the depth of field in the presence of air and immersion liquids with different refractive indices n	32
Fig. 2.3.3: Schematic of a conventional OPT setup.....	33
Fig. 2.3.4: Refractive index dependent resolution vs. the depth of field	34
Fig. 2.3.5: n dependent resolution vs. the emitted wavelength.....	36
Fig. 2.3.6: Principle of optical projection tomography	37
Fig. 2.4.1: UBP) image of the original and FBP image.....	38

TABLE OF FIGURES

Fig. 2.4.2: Reconstructed slice of the fluorescent salivary glands from a <i>Drosophila melanogaster</i> early stage pupa.....	39
Fig. 2.4.3: Frequency response of a Ram-Lak, Hann and Hamming filter	40
Fig. 2.5.1: Raw images of 3 μ m diameter GFP fluorescent microspheres.....	41
Fig. 2.5.2: Distribution of $I(P)$ in correspondence to the distance from the C.O.R.	42
Fig. 3.1.1: Schematic drawing of the OPT setup.....	44
Fig. 3.1.2: Detailed laboratory OPT setup.....	45
Fig. 3.1.3: Sample holder and imaging vessel.....	46
Fig. 3.2.1: Schematic of a binning procedure.....	47
Fig. 3.2.2: Subjection of the mean background intensity in dependence of cooling temperature	48
Fig. 3.3.1: Excitation and emission spectra for eGFP	49
Fig. 3.3.2: Excitation and emission spectra for dsRed	49
Fig. 3.3.3: Fluorescence spectra of GFP and dsRed in prescence of HbO ₂ and Hb	50
Fig. 3.4.1: Micro capillary sizes from intraMARK™.....	51
Fig. 3.5.1: Average absorption coefficient of grounded <i>D. melanogaster</i> samples.	53
Fig. 3.6.1: Initial window of the general user interface (GUI).....	54
Fig. 3.6.2: Verification of the initial projection vs. the final projection	55
Fig. 3.6.3: Display of aof error of the initial an final projection.....	56
Fig. 3.6.4: Definition of the ROI from the raw data.....	57
Fig. 3.6.5: GUI for radon transformation settings.....	58
Fig. 3.6.6: Artifacts form an inccorectly indetified position of the rotational axis position.....	60
Fig. 4.1.1: Lifecycle of <i>Drosophila melanogaster</i>	62
Fig. 4.1.2: White light raw images acquired with OPT.....	63

TABLE OF FIGURES

Fig. 4.1.3: Reconstruction of the white light and fluorescence data taken <i>in vivo</i> from a day 5 state <i>Drosophila melanogaster</i> larva	64
Fig. 4.1.4: In-vivo results from an early stage (4-5th day) pupa of the <i>Drosophila melanogaster</i> enhancer trap line GR2x	65
Fig. 4.2.1: Schematic presentation of <i>C. elegans</i> ' anatomy.....	67
Fig. 4.2.2: Reconstructed data acquired with white light illumination from <i>C. elegans</i>	68
Fig. 4.2.3: 3D reconstruction of <i>Caenorhabditis elegans</i>	69
Fig. 4.2.4: <i>In silico</i> slice through <i>C. elegans</i> with GFP expression under control of the <i>daf-6</i> promoter and dsRed expression under control of <i>pqn-21</i> promoter.	70
Fig. 4.2.5: 3D reconstruction of GFP expression under control of <i>daf-6</i> promoter	71
Fig. 4.3.1: Overview of <i>Parhyale</i> development.....	72
Fig. 4.3.2: 2D image acquired with a fluorescence microscope.	73
Fig. 4.3.3: Superimposed reconstruction of the exoskeleton and dsRed expression from the 3XP3 promoter in the muscular system of a <i>Parhyale hawaiiensis</i>	74
Fig. 4.3.4: 3D reconstruction of the exoskeleton of the <i>P. hawaiiensis</i> s.....	75

LIST OF ABBREVIATIONS

LIST OF ABBREVIATIONS

μMRI: Micro Molecular Resonance Imaging

μOPT: Micro Optical Projection Tomography

ART: Algebraic Reconstruction Technique

BABB: benzyl benzoate – benzyl alcohol (aka Murrays clear at a 2:1 mixture)

CLSM: Confocal Laser Scanning Microscopy

COR: Center of Rotation

CT: Computed Tomography

IR-A: Infrared A (780-1400nm)

DICM: Differential Interference Contrast Microscopy

DNA: Deoxyribonucleic acid

DPSS: Diode Pumped Solid State

CCD: Charged Coupled Device

dsRed: Red fluorescent Protein

EMCCD: Electron Multiplier Charged Coupled Device

FBP: Filtered Back Projection

GFP: Green Fluorescent Protein

GUI: General User Interface

Hb: Hemoglobin

HbO₂: Oxy-Hemoglobin

ICCD: Intensified Charged Coupled Device

LacZ: β-Galactosidase

MRI: Molecular Resonance Imaging

mRNA: Messenger Ribonucleic acid

MSBB: methyl salicylate – benzyl benzoate

ND: Neutral Density

OCM: Optical Coherence Microscopy

OCT: Optical Coherence Tomography

LIST OF ABBREVIATIONS

OD: Optical Density

OPT: Optical Projection Tomography

PSF: Point spread function

RNA: Ribonucleic acid

ROI: Region of Interest

SHG: Second Harmonic Generation

SNR: Signal to Noise Ratio

SPIM: Selective Plane Illumination Microscopy

TE: Thermo Electric (cooling)

UBP: Unfiltered Back Projection

VIS: Visible wavelength region (450-780nm)

NA: Numerical Aperture

X-gal: 5-Brom-4-chlor-3-indoxyl- β -D-galactopyranosid

1 INTRODUCTION

1.1 TOMOGRAPHIC IMAGING

The term “tomography” is composed of the two Greek words “τόμος“, which can be translated as “cut” or “slice” and “γραφία” which is the Greek term for “picture”. The image that is produced by a tomograph is called a tomogram. In order to achieve information from a tomogram, one needs to reconstruct the data set by using a reconstruction algorithm, which then computes the tomographic slices of the object. These slices can be stacked together and form a 3D stack of the object of interest.

Starting with Johann Radon’s work *On the determination of functions from their integral values along certain manifolds* [1, 2] in 1917, different tomographic devices have been developed [3-18]. During the past decade, optical tomographic imaging with visible and near infrared light has become an increasingly interesting area due to development of fluorescent markers such as fluorescent proteins, novel techniques such as MRI or X-ray computed tomography and easy to use and affordable equipment. The principle of Optical Projection Tomography is depicted in figure 1.1.1. Light traverses through an optical diffuser to achieve a homogeneous illumination of the specimen. Inside the specimen, it can be a.) absorbed and scattered due to the specimen’s optical properties, or b.) absorbed by certain contrast agents such as colored dyes or fluorescent probes. Light that is influenced by the specimen’s optical properties results in an absorption tomogram which can be assumed of as a topographic map of the absorption coefficients of the specimen. In case of fluorescent contrast agents the interest is in the emitted light of the fluorescent probes. For its detection, a fluorescent filter is placed in front of the detector, so that the excitation light is filtered and only fluorescence light is detected. The major advantage of OPT in contrast to other

3D imaging techniques is that in OPT one already achieves full volumetric information of the specimen from a single projection. This becomes clear from fig. 1.1.1. The light that is detected by the imaging system and builds up a projection of the specimen has travelled through it before. Thus it contains information of the complete depth of the specimen.

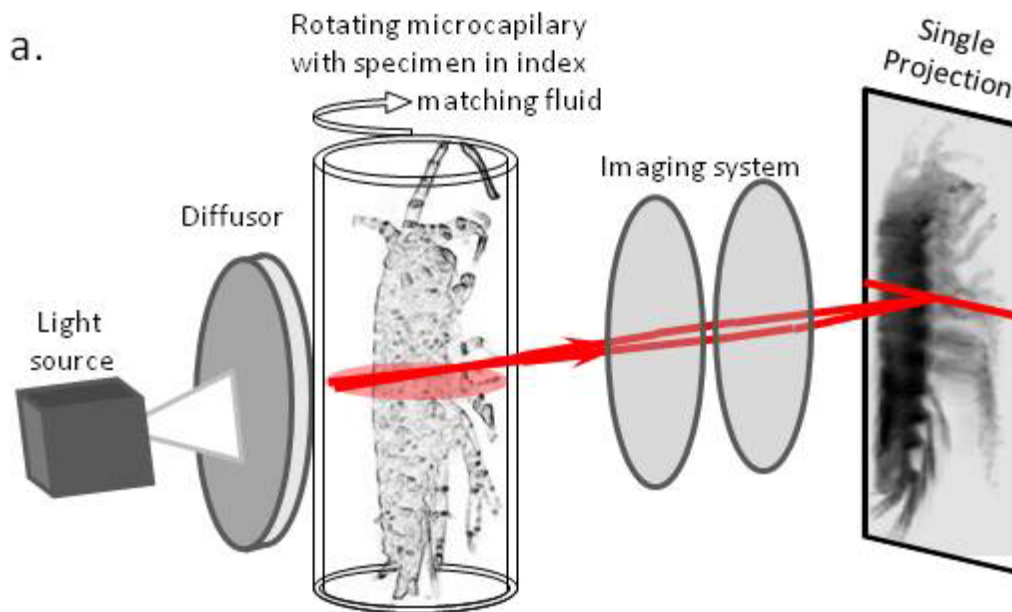


Fig. 1.1.1: The principle of the application of light to a sample and its detection in Optical Projection Tomography. The light from a light source is transmitted through a diffuser in order to apply a homogeneous illumination to the object of the complete field of view of the detector sided imaging system. One single projection contributes the data from the whole depth of the sample and thereby it already contains full volumetric information.

1.2 AIM AND STRUCTURE OF THIS THESIS

The aim of the work presented in this thesis was to design and develop a tomographic device enabling transmission and emission optical projection tomography *in vivo* in biological samples such as *Drosophila melanogaster* and *Caenorhabditis elegans* in different developmental states. This required sample preparation *without* using organic solvents [67] e.g. benzyl alcohol – benzyl benzoate (BABB / Murray’s clear) or methyl salicylate – benzyl

benzoate (MSBB) to clarify biological tissues, thus raising the issue of dealing with the natural optical properties of the specimen, the absorption and scattering coefficients, which so far had not been done in Optical Projection Tomography.

This thesis is structured as follows: this chapter represents a brief introduction to optical projection tomography, its development within the past few years, and a list and comparison of commonly used microscopy techniques for achieving volumetric data information, namely confocal microscopy, Selective Plane Illumination Microscopy (SPIM) and Ultramicroscopy. The second chapter includes the theory used in OPT and some additional information on the correction of artifacts in OPT generated by using standard backprojection algorithm and some additional information about fluorescent proteins and probes used during this work. In Chapter 3 I present the technical setup with its features, namely the time stability, camera linearity and binning as well as the used filters for fluorescence detection and a brief introduction to the different model organisms used for this thesis and finally the sample preparation for OPT. In Chapter 4 I present the reconstruction of the different model organisms and describe the results of the measurements in OPT as performed during this work. In chapter 5 I present the conclusions of the presented results and a brief future outlook of this work.

This thesis is focused on in-vivo high resolution Optical Projection Tomography (OPT) which uses simple and cost effective setups with the capability of fluorescence imaging as well as providing anatomical information of the specimen [19, 20] using the information given by the specimen's absorption properties. Instead of optical sectioning of the specimen as applied in Selective Plane Illumination Microscopy (SPIM), OPT makes use of back projecting images acquired from a rotating specimen using a Radon Transform algorithm [2] traditionally developed for X-Rays offering magnification dependent resolution down to 1-5 μm [21-23]. In contrast to

other techniques, its major advantage is the immediate acquisition of data from the whole specimen with only one projection.

In this work I present the design and development of a custom Optical Projection Tomography setup. I further show its imaging capability in the absence of optical clearing agents and thereby its potential of *in vivo* imaging of small living organisms such as *Drosophila melanogaster* and *Caenorhabditis elegans*. These examples address the important problem of acquiring images from absorbing and scattering objects, which has not been performed using Optical Projection Tomography to date.

1.3 OTHER LINEAR EXCITATION BASED 3D MICROSCOPY TECHNIQUES

1.3.1 CONFOCAL MICROSCOPY

Confocal Microscopy was introduced first by M. Minsky in 1955 [24] but became a standard technique by the development of lasers as Laser Scanning Confocal Microscopy in the 80's. The field of confocal laser scanning microscopy (CSLM) has evolved ever since with the development of scanning discs (Nipkow disc) and the implementation of femtosecond pulse sources that enable the generation of multi harmonic signals in biological tissues. Since its introduction to the field of volumetric imaging and imaging analysis of cells as well as their organization inside biological tissues and organisms, the technique of optical sectioning has replaced physical sectioning in many cases. Due to anisotropic resolution, meaning axial resolution is a factor of 3 lower than lateral resolution, volumetric data evaluation becomes complicated and severely limited. To solve the problem of low axial resolution, Shaw et al. introduced a technique called axial tomography [25]. Rotation of the specimen in the focal plane of an optical system with high resolution enabled obtaining additional information about specimen structure

and has been applied not only in Widefield Microscopy [25-27] but also has significant advantages in Confocal Microscopy [26, 28]. In 1997 CLSM underwent significant modifications by the implementation of two-photon excitation, a technique whose concept was first described by Göppert-Mayer in 1931 but it took another 31 years until its first observation by Abella in 1962. Denk and Webb finally pioneered the first 2 photon microscope [29], thus delivering the ability of imaging second harmonic generation signals (SHG) with the advantage of higher penetration depth due to excitation wavelength shift towards the near-infrared region. Figure 1.3.1 shows the principle of Confocal Microscopy.

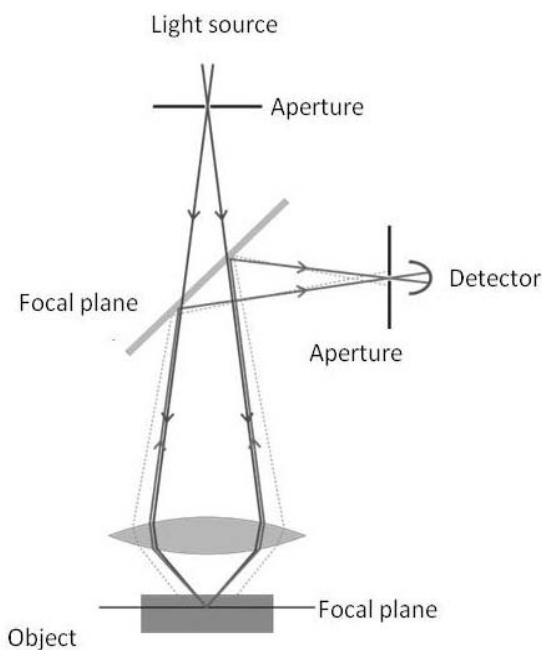


Fig. 1.3.1: Principle of Confocal Microscopy. In a conventional (i.e., wide-field) fluorescence microscope, the entire specimen is illuminated by a light source. All parts of the specimen in the optical path are excited and the resulting fluorescence is detected as background signal. In contrast, a confocal microscope uses point illumination and a pinhole in an optically conjugate plane in front of the detector to eliminate out-of-focus light. As only light produced by fluorescence very close to the focal plane can be detected the image resolution,

particularly in the sample depth direction, is much better than that of wide-field microscopes. However as much of the light from sample fluorescence is blocked at the pinhole this increased resolution is at the cost of decreased signal intensity so long exposures are often required

However, the depth limit of Confocal Microscopy is reported to be approximately 1 mm, which is insufficient for imaging larger specimens intact. Even recent developments of equivalent techniques such as Multi

Photon Microscopy did not lead to sufficiently better penetration depths. A further drawback is Confocal Microscopy's lack of imaging colored dyes that are powerful reporters in biomedical assays, and it is not clear how other absorption contrast agents can be used.

1.3.2 CONFOCAL THETA MICROSCOPY

An advanced scanning technique derived from Confocal Microscopy is Confocal Theta Microscopy. The modification is the perpendicular arrangement of the excitation and the detection path as depicted in figure 1.3.2. This collocation achieves a convolution of the point-spread function (PSF) defined by the optics in the excitation path and the PSF of the detection sided optics. This technical approach results in an almost isotropic point spread function of the system and thereby to a substantially improved resolution in contrast to conventional Confocal Microscopy. It is assumed that the limitations of Confocal Theta Microscopy are similar to those of conventional Confocal Microscopy that are based on the lack of imaging absorbing non-emitting contrast agents and inability to enable the acquisition of volumetric absorption data sets from a specimen of interest.

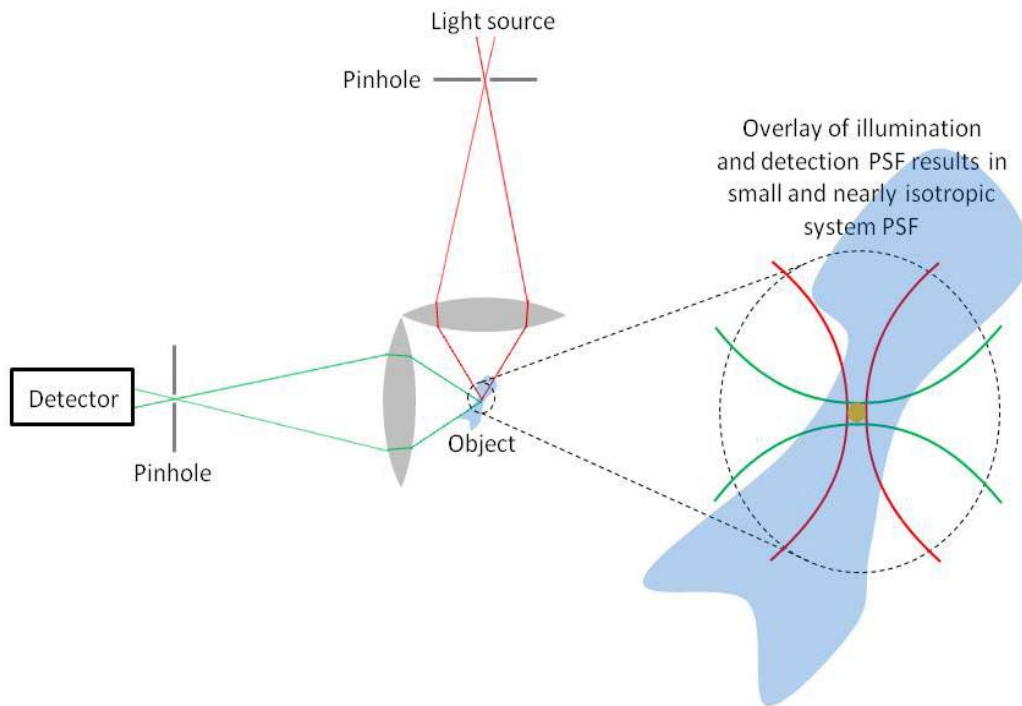


Fig. 1.3.2: Basic layout of a Confocal Theta Fluorescence microscope. Two separate optical systems are used for the illumination of a small object and the detection of the fluorescence light. The point-spread functions generated by the optics of the excitation as well as of the detection path are both elongated along their respective optical axes defined by the Rayleigh range of the optical system. However, only fluorophores in their common volume can contribute to the signal.

(source: www.lmg.embl.de/confocaltheta.html)

1.3.3 SPIM AND ULTRAMICROSCOPY

Selective Plane Illumination Microscopy (SPIM) and Ultramicroscopy offer optical sectioning, reduced fluorophore bleaching, fast, highly efficient image recording, but small depth penetration, especially when multiple views are combined. Both techniques perform well in large samples such as fish or fly embryos which are naturally transparent or which have been cleared with clearing agents such as BABB (benzyl alcohol - benzyl benzoate) or MSBB (methyl salicylate – benzyl benzoate) to reduce their opacity.

Both principles are universal and have been successfully applied using objective lenses with magnifications from 5x to 100x. Sample sizes from

several millimeters down to the cell level can be covered with isotropic resolutions from $10\mu\text{m}$ to $0.5\mu\text{m}$. This range is similar to the specimen sizes and resolution that can be achieved with OPT and μOPT respectively. However, light sheet based illumination techniques as SPIM and Ultramicroscopy require a full scan of the specimen of interest, whereas in OPT and μOPT respectively.

It is reported that the resolution in SPIM as well as in Ultramicroscopy degrades in large specimen imaging for focusing deep inside due to light scattering, which is assumed to arise from residual variations of the refractive index of cleared tissue [30]. The schematics of SPIM and Ultramicroscopy are represented in the figures 1.3.3 and 1.3.4 respectively.

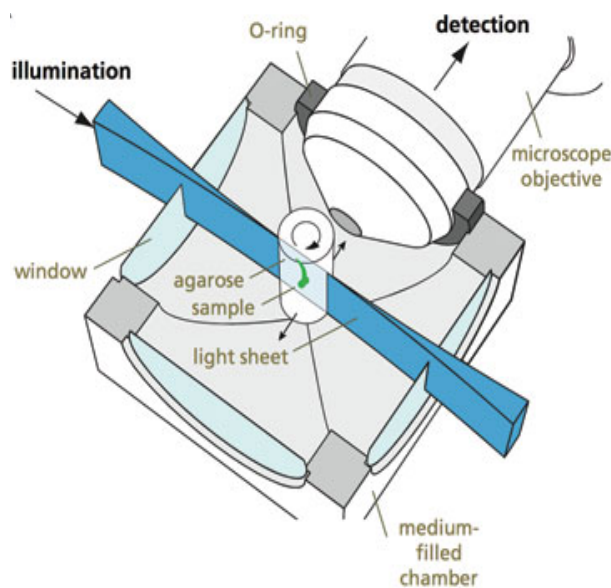


Fig. 1.3.3: Principle of Selective Plane Illumination Microscopy (SPIM) (source: <http://www.scienceinschool.org>).

The principle of SPIM is based on a light sheet illumination perpendicular to the detection arm. The specimen is fixed in an agarose cylinder and suspended in medium filled chamber with its rotation center coincident to the light sheets focus. The major drawback of this technique is the required transparency of the

specimen. To date, it has only been applied to highly transparent specimens such as Zebrafish embryos or specimens that have been treated with optical clearing agents to change the specimen's opacity and make it more transparent.

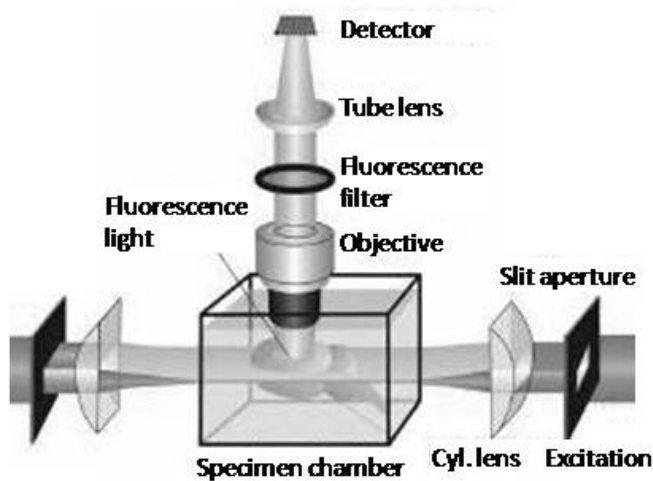


Fig. 1.3.4: Principle of Ultramicroscopy. The sample is illuminated by a laser forming a thin sheet of light. Fluorescent light is thus emitted only from a thin optical section and collected by the objective lens. (source: <http://www.cg.tuwien.ac.at>) The principle of illumination in Ultramicroscopy: Light is being focused by a cylinder lens resulting in a light sheet similar

to SPIM. In the area where the beam is focused maximally a quoin-like description is not appropriate and the profile of the illumination beam stays relatively constant. The sample is immersed in the same liquid used to gain transparency. This assures that the illumination beam is not diffracted on the surface of the sample and propagates straight, even inside the sample. By moving the sample, different z-positions can be illuminated and recorded afterwards resulting in a 3D image stack.

SPIM as well as Ultramicroscopy [30] achieve optical sectioning by generating a light sheet along an axis orthogonal to the axis of detection, which has been demonstrated to improve axial resolution [31-35]. The excitation light is focused by a cylindrical lens to create a sheet of light only in the focal plane of a detection optic, thus suppressing out-of-focus fluorescence excitation. The only difference between these techniques is that in contrast to SPIM, objects images with Ultramicroscopy are illuminated from both sides. The effect of illuminating with a light sheet is similar to Confocal Microscopy but in contrast, excitation is not only in a focal spot but in the whole area of detection. A further drawback of CLSM is, that bleaching occurs along the whole optical axis of excitation, therefore in the whole specimen. Whereas in SPIM, bleaching only occurs in the plane of observation, thus reducing the total number of fluorophore excitations to a minimum compared to CLSM. Summarizing, light sheet illumination combined with a common optical wide

field microscope enables imaging of fluorescence patterns deep inside specimens up to several millimeters both *in-* and *ex vivo* and also shows potential in the fields of 3D cultured cells [36] and 3D cell migration [37]. However a major drawback is that in contrast to OPT, one only images one plane at a time, whereas in OPT the information from the whole specimen is achieved in a single projection. Thus, obtaining only a few projections already allows a full volumetric reconstruction of the specimen by using different reconstruction algorithms, such as iterative functions. Yet another drawback of SPIM and Ultramicroscopy is the lack of available contrast agents since light sheet illumination techniques are limited to fluorescence imaging, thus delivering no anatomical information given by the absorption of biological probes as OPT does, or by other contrast agents as i.e. colored dyes.

1.4 DEVELOPMENT OF MICROSCOPY AND TOMOGRAPHY

In the field of microscopy and tomography, *in vivo* imaging techniques have developed rapidly within the last decade [38-40], most of which are based on optical sectioning (e.g. Confocal Microscopy techniques [41]). Other applications have also been developed using contrast enhancing techniques such as Differential Interference Contrast Microscopy (DICM) [42, 43] and Optical Coherence Microscopy and Tomography [44, 45] (OCM and OCT). Although these techniques have resulted in enormous progress in the field of 3D microscopy, they have significant limitations when it comes to high resolution whole specimen imaging and/or imaging of multiple contrast agents or fluorescent proteins.

In 2002 a new technique was developed: Optical Projection Tomography (OPT) [3, 19, 20] covering an imaging gap between Confocal Microscopy and MRI with specimen sizes from 1-15 mm. In addition to OPT,

Selective Plane Illumination Microscopy (SPIM) [46, 47] is also of great interest in the field of high resolution 3D imaging. A major progress in biomedical imaging was the discovery of fluorescent proteins such as GFP (Green Fluorescent Protein), which was discovered by O. Shimomura in 1961, and other fluorescent proteins later.

Fluorescent proteins have become a major tool in optical imaging, allowing the non-invasive recording of fluorescent signals from within intact organism and thus monitoring of gene products. Most of them are non-toxic in almost all eukaryotic cells and are therefore widely used as non invasive probes to study different biological models from single cells to whole organisms. The use of GFP enables tracking the protein of interest through many aspects of biological function: expression, localization, movement, interaction and activity in the cell, tissue or organism. A transgenic organism can be made with the gene encoding GFP attached to the target gene, providing a directly visible display of the gene's expression pattern in the living organism.

This thesis presents the first 3D *in vivo* images applying OPT on non-cleared specimens such as *C. elegans* and especially in millimeter sized organisms such as *D. melanogaster* [48] and *P. hawaiiensis*. I would like to emphasize that such an imaging study using fluorescent protein-expressing transgenics could not be performed using optical clearing agents such as benzyl alcohol – benzyl benzoate (BABB) for specimen clearing as found so far in OPT related literature, although OPT has successfully been used to image growing mouse limbs in culture.

Another 3D imaging technique to image specimens of sizes up to 2-3 mm is Optical Coherence Tomography (OCT) [49], however it is still not suitable to image whole mouse embryos, and to date it is not clear how contrast agents, such as fluorescent or absorbing probes, can be used in OCT since this technique is based on detecting changes in the refractive index of a

specimen. A technique that has been derived from Magnetic Resonance Imaging (MRI) has also shown significant potential in developmental biology [50]. New μ MRI devices allow imaging specimens at the millimeter range with micrometer resolution. Although high contrast agents for *in vivo* detection of LacZ reporter expression have recently been reported [51], its inability to image commonly used biomedical assays (as mentioned above) and its complexity and expense makes μ MRI unsuitable for general applications.

There are two principles in gathering volumetric data of an object. In currently used 3D optical microscopy systems, the principle is to generate an optical section or slice by focusing in a particular plane of an object and thereby reducing noise from regions which are out-of-focus, as for example in Confocal Microscopy, Selective Plane Illumination Microscopy [46, 52, 53] and ultra microscopy [30, 54, 55]. These slices already contain volumetric information and can therefore directly be converted into 3D space.

In contrast to these techniques, the raw data obtained with OPT represent only pictures taken from various angles and therefore no real 3D information. It requires mathematical transformation to acquire the original object [56]. Other issues are the tissue optical properties that strongly depend on the wavelengths used in optical tomographic devices. X-rays, as used in computerized tomography (CT) undergo almost no significant refraction or scattering events while passing through biological tissue, thus making them suitable for imaging high density tissues such as bone.

The emerging field of diffuse optical tomography uses red (650 – 780nm) or near infrared (IR-A: 780 – 1400nm) wavelengths that can traverse as much as 10 cm of living biological tissue, because the absorption band of biological tissue in these wavelengths decreases by 2-3 orders of magnitude in contrast to the visible (VIS) wavelengths in the blue (457 – 488nm) or green (514 – 532nm), that are usually used in single photon excitation of fluorescent

probes. However the resulting scattering of light means that only low-resolution reconstructions are possible [57]. OPT in contrast does not suffer from lack of axial resolution since it detects rays that propagate straight through a whole specimen. Due to the rotation of the specimen, resolution of the acquired data is only limited by lateral resolution of the imaging device.

1.5 OPT IN THE PAST, PRESENT AND FUTURE

It has been shown that the information gathered from analyzing the volumetric tissue information is invaluable for understanding embryonic development. A new approach was volumetric mapping of gene expression patterns and the superimposition of these patterns with the anatomical information obtained from measuring the tissue optical properties [58].

This ability of simultaneous representation of anatomical and functional sample information encompasses not only the 3D representation of different labeled tissues but includes also additional information about cell or gene interaction. Obtaining this data has become a great challenge in the era of genomics and various techniques have been developed or improved substantially to provide volumetric data acquisition of biological tissues [38, 39, 49-51, 59], while other methods for reconstruction have become more and more automated [38, 59]. However, imaging and optical sectioning of specimens with dimensions of several millimeters in size still requires some hundred serial or optical individual sections, thus resulting in large data sets of some hundred megabytes up to some gigabytes of data.

The increasing demand for comprehensive gene expression data has led to the creation of large-scale bioinformatics databases, some of which aim to store data on the 3D expression patterns of thousands of genes [38]. It is believed that Optical Projection Tomography will dramatically increase the

rate at which such data is gathered as well as facilitate the detailed examination of mutant phenotypes from large-scale mutagenesis screens.

In addition to its use in developmental biology, OPT has the potential for use in medical applications for which knowledge of the 3D structure of a specimen may be useful, but not readily accessible from histopathological sections. It has shown great potential in the analysis of biological specimens from the cell level up to sub-centimeter sized samples and in filling the imaging gap between Confocal Microscopy and Magnetic Resonance Imaging (MRI).

Throughout the past 6 years, OPT has been applied in imaging of embryonic development [20], fluorescent immunohistochemistry [60], gene expression imaging [61], transgenic imaging [62] and phenotyping [63] in various tissues and organisms [64-66] from whole animals down to the cellular scale. Apart from Lee, Avondo et al. (2006), where *in vivo* imaging in plant development is presented, in all the other cases measurements could not be performed *in vivo* due to sample preparation in order to change the specimen's elemental optical properties (clear the specimen) strongly reducing its absorption coefficient and scattering properties. This is done by clearing the tissue with a 1:2 mixture of Benzyl Alcohol - Benzyl Benzoate [3, 67] (BABB) (Murray's clear) once the specimen has been fixed. Even though this approach gives the best results in terms of resolution and sensitivity, its main drawback is that due to its aggressive characteristics as an organic solvent, *in vivo* imaging of cleared specimens becomes impossible and so does imaging of fluorescent proteins, since these are degraded by the BABB. Additionally it should be denoted, that these organic solvents are highly toxic and should be handled with care. Another application of OPT has been shown in single cell imaging achieving sub-micron resolution in the reconstructed images as well as the rendered data [4], using not only the projections by rotating the sample but also the microscopes ability of scanning through the specimen creating so

called ‘pseudoprojections’. It has further been shown that fixed and labeled imaging in murine organs is also feasible using OPT [68, 69].

2 THEORY

2.1 BEAM PROPAGATION IN ABSORBING MEDIA

This chapter mathematically describes the propagation of a beam in absorbing media. If one considers a homogeneous medium the absorption coefficient can be derived by a first order differential equation. However, the following explanation is based on a more complex derivation from Maxwell's equations and takes into account the refractive index shows the derivation taking into account the refractive index n of a medium and a

Before introducing the reconstruction of rays which propagated through a medium, one has to consider the way the beam is influenced by the optical properties of the medium. If we consider the real refractive index n of the medium to be constant and homogeneous, the variation of the space-dependent parts of a complex monochromatic electromagnetic field of frequency ω along each ray in the beam is given by

$$\mathbf{E}_2 = \mathbf{E}_1 e^{ik_0 n l}, \quad \mathbf{H}_2 = \mathbf{H}_1 e^{ik_0 n l} \quad (1)$$

with $k_0 = \omega/c$ being the free-space wave number and l the distance between two typical points P_1 and P_2 on the ray as illustrated in figure 2.1.1.

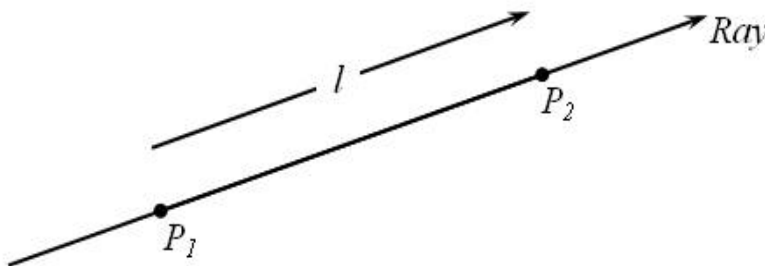


Fig. 2.1.1: Illustration of Eq. (1)

E_1 and E_2 are the space – dependent parts of the electric fields at the points P_1 and P_2 respectively while H_1 and H_2 are the corresponding space-dependent parts of the magnetic fields at these points.

If we now suppose a weakly absorbing medium, the absorption may be taken into account by replacing the real refractive index n by the complex one, which is here denoted by \hat{n} ,

$$\hat{n} = n(1 - i\kappa) \quad (2)$$

where κ is a real constant just like n . The constant κ is called the *attenuation index* but is better known as the *extinction coefficient* of the medium. The quantities of n and κ can be expressed in terms of the materials constants ϵ , μ and σ considering the equations for non-conducting media, if in the latter the dielectric constant ϵ is replaced by

$$\hat{\epsilon} = \epsilon + i \frac{4\pi\sigma}{\omega} \quad (3)$$

while ϵ , in a good approximation, was shown to be real for frequencies of ω that are close to a resonance.

Introducing a complex phase velocity \hat{v} and a complex refractive index \hat{n} additionally to the complex wave number \hat{k} and the complex dielectric constant $\hat{\epsilon}$, the phase velocity derived from Maxwell's equations and the 'absolute refractive index' n of a medium can be written as

$$\hat{v} = \frac{c}{\sqrt{\mu\hat{\epsilon}}}, \quad \hat{n} = \frac{c}{\hat{v}} = \sqrt{\mu\hat{\epsilon}} = \frac{c}{\omega} \hat{k} \quad (4)$$

If we now square Eq. (2), we receive

$$\hat{n}^2 = n^2(1 + 2i\kappa - \kappa^2) \quad (5)$$

which, after inserting the equations of (4), can be written as

$$\hat{n}^2 = \mu\hat{\epsilon} = \left(\epsilon + i \frac{4\pi\sigma}{\omega} \right). \quad (6)$$

However since σ , just like ϵ , is not a true constant but is frequency dependent, it is to a good approximation real. If we now assume that ϵ is also

real, the following relations can be obtained upon equating the real and imaginary parts in Eq. (5) and Eq. (6):

$$n^2(1 - \kappa^2) = \mu\varepsilon \quad (7)$$

$$n^2\kappa = \frac{2\pi\mu\sigma}{\omega} = \frac{\mu\sigma}{\nu} \quad (8)$$

From (7) and (8) follows that

$$n^2 = \frac{1}{2} \left(\sqrt{\mu^2\varepsilon^2 + \frac{4\mu^2\sigma^2}{\nu^2}} + \mu\varepsilon \right) \quad (9)$$

and

$$n^2\kappa^2 = \frac{1}{2} \left(\sqrt{\mu^2\varepsilon^2 + \frac{4\mu^2\sigma^2}{\nu^2}} - \mu\varepsilon \right) \quad (10)$$

Since n and $n\kappa$ are real, the sign of the square roots can be taken positive, and consequently n^2 as well as $n^2\kappa^2$ must be positive.

If we now take the wave equation with a complex wave number into account, the simplest solution is that of a plane, time-harmonic wave

$$\mathbf{E} = \mathbf{E}_0 e^{i[\mathbf{k}\mathbf{r}\cdot\mathbf{s} - \omega t]}, \quad (11)$$

where \mathbf{s} denotes a unit vector in the direction of propagation.

Substitution of $\hat{\mathbf{k}}$ by $\omega\hat{\mathbf{n}}/c$ which equals $\omega n(1 + ik)/c$, (11) becomes

$$\mathbf{E} = \mathbf{E}_0 e^{-\frac{\omega}{c}n\kappa\mathbf{r}\cdot\mathbf{s}} e^{i\omega\frac{n}{c}\mathbf{r}\cdot\mathbf{s} - t} \quad (12)$$

where the real part of this expression, namely

$$\mathbf{E} = \mathbf{E}_0 e^{-\frac{\omega}{c}n\kappa\mathbf{r}\cdot\mathbf{s}} \cos \left\{ \omega \left[\frac{n}{c} \mathbf{r} \cdot \mathbf{s} - t \right] \right\} \quad (13)$$

represents the electric vector and is a plane wave with wavelength $\lambda = 2\pi c/\omega n$ and attenuation given by the exponential term. Since the energy density w of the wave is proportional to the time average of \mathbf{E}^2 , it follows that w decreases in accordance with the relation

$$w = w_0 e^{-\chi\mathbf{r}\cdot\mathbf{s}} \quad (14)$$

where

$$\chi = \frac{2\omega}{c} n\kappa = \frac{4\pi\nu}{c} n\kappa = \frac{4\pi}{\lambda_0} n\kappa = \frac{4\pi}{\lambda} \kappa \quad (15)$$

λ_0 being the wavelength in vacuum and λ the wavelength in the medium. Here the constant χ denotes the *absorption coefficient* usually written as α . The energy density drops to $1/e$ of its value after the wave has advanced a distance d where

$$d = \frac{1}{\chi} = \frac{\lambda_0}{4\pi n\kappa} = \frac{\lambda}{4\pi\kappa} \quad (16)$$

This quantity is usually a very small fraction of the wavelength.

If one now identifies the intensity of the field with the absolute value of the Poynting vector, for example

$$I = \frac{c}{8\pi} |\mathcal{R}(E \times H^*)| \quad (17)$$

where \mathcal{R} denotes the real part, it follows from Eq. (1), with n replaced by Eq. (2), that

$$E_2 \times H_2^* = E_1 \times H_1^* e^{-2k_0 n\kappa l}. \quad (18)$$

From Eq. (17) and (18) follows, that the intensities at the points P_1 and P_2 are related by

$$I_2 = I_1 e^{-\alpha l} \quad (19)$$

where the constant

$$\alpha = 2k_0 n\kappa \quad (20)$$

is called the *absorption coefficient* of the medium and l is the distance between P_1 and P_2 .

Since the absorption coefficient of an object cannot be considered to be constant but rather varies with position, one introduces the more general Equation

$$I_2 = I_1 \exp \left(- \int_{p_1}^{P_2} \alpha(\mathbf{r}) dl \right) \quad (21)$$

which is commonly known as *Beer's law* and which is frequently derived by quasi-geometrical arguments of the theory of radiative energy transfer. A simplified description of the radiative energy transfer theory is, that a beam of radiation travels through a medium loses energy due to absorption, gains energy by emission and redistributes energy by scattering.

Figure 2.1.2 depicts the decrease of an incident ray of intensity I of a specimen of a homogeneous distributed absorption coefficient α and a defined thickness l .

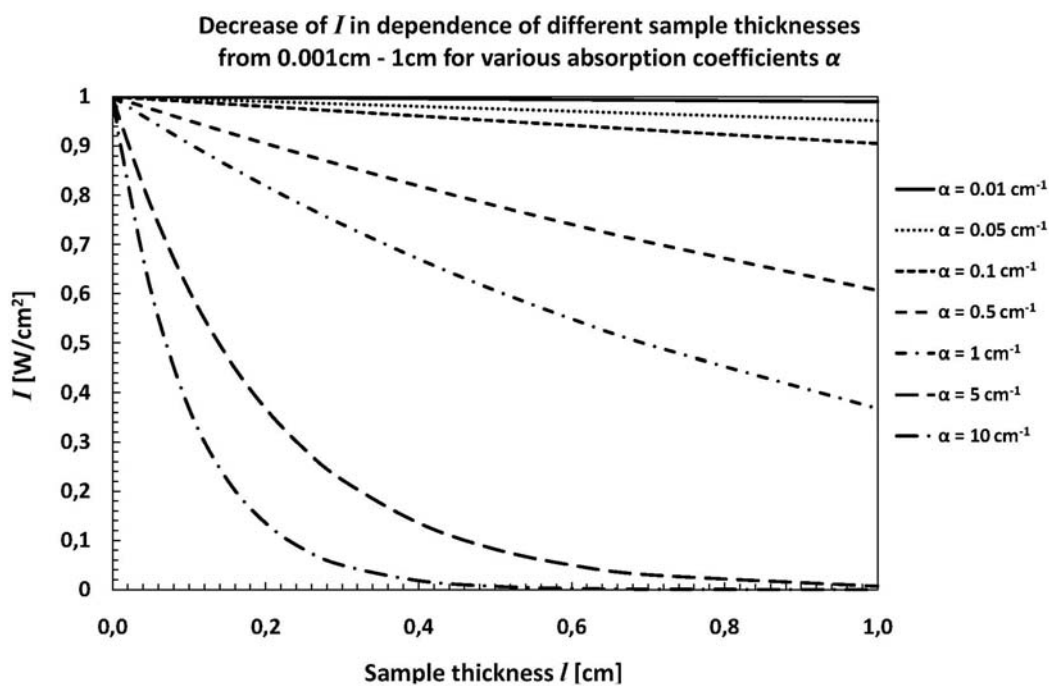


Fig. 2.1.2: Graphic representation of *Beer's law*. Shown is the decrease of an incident intensity $I_0 = 1 \text{ W/cm}^2$ after traversing through an object with a defined thickness for different absorption coefficients α . With increasing absorption coefficient, the ability of an imaging system to generate proper absorption tomograms degrades. Considering an average absorption coefficient of 5 cm^{-1} , which is close to the mean absorption coefficient of an adult *D. melanogaster* (see fig. 3.5.1) and a size of the specimen of 1mm, would still result in approximately 30% of transmitted light.

2.2 THE RADON TRANSFORM

Defined by Johann Radon in 1917 and named after him later, the linear integral transformation has played a fundamental role in computed tomography for the reconstruction of 2D functions from one-dimensional projections since the early 70's. Here I would like to present the demonstrative geometrical interpretation of the Radon transform, thus allowing its application to solve problems in image processing. A further advantage is the correlation between the Radon transform and the 2D Fourier transform by the *central slice theorem*, thus enabling an efficient calculation of the Radon transform under consideration of the Fast Fourier Transform (FFT).

One of the principal quantities which provides information about biological tissues is the absorption coefficient $\alpha(\mathbf{r})$, which has been described in 2.1. Knowing the distribution of $\alpha(\mathbf{r})$ delivers the anatomical information of the subject. If we suppose that a beam of monochromatic light traverses through a specimen from a source point P_0 to a detector located at a point P (see figure 2.2.1), which measures the intensity, denoted by I , we know from Beer's law that I follows the equation

$$\int_{P_0}^P \alpha(\mathbf{r}) ds = -\ln \frac{I(P)}{I(P_0)}. \quad (22)$$

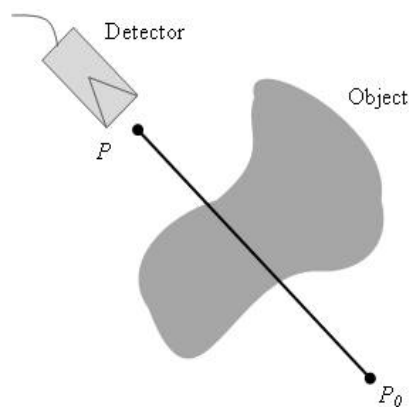


Fig. 2.2.1: Illustration of the concept of a ray integral as defined in Eq. (22).

Measuring the intensity $I(P)$ at the detector and knowing the intensity $I(P_0)$ at the source point P_0 , we can now deduce the value of the integral of the absorption coefficient from P_0 to P along the ray which is defined on the left-hand-side of Eq.22. This integral is called the *ray integral*. A suitable set of ray integrals is said to form a *projection*. In practice, if we consider a CCD chip as a detector, each pixel detects the attenuated light defined by a ray integral. This thesis only concentrates on the so-called parallel projections as defined in figure 2.2.2.

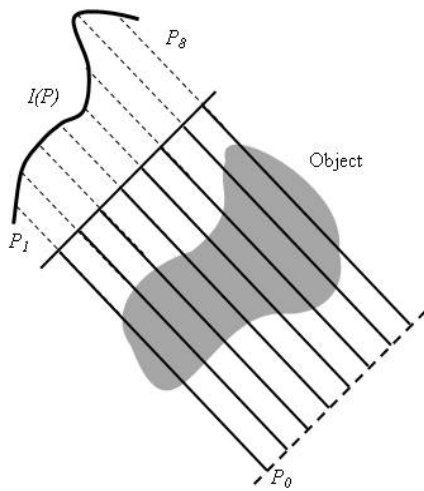


Fig. 2.2.2: Parallel beam projection

The basic goal is now to deduce the spatial distribution of the absorption coefficient $\alpha(\mathbf{r})$ through a specimen from a sufficient number of projections.

The mathematical solution was given by Johann Radon [1], but first applied fifty years later with the rising field of computerized tomography.

The Radon transform of an arbitrary function $f(x)$ is defined by

$$F(\xi, p) = \int f(\mathbf{x}) \delta(p - \xi \cdot \mathbf{x}) d^N x \quad (23)$$

with δ being the one-dimensional Dirac delta function, p an arbitrary scalar and assuming that the integration extends over the whole \mathbf{x} -space. Furthermore consider that \mathbf{x} and ξ being N-dimensional vectors,

$$\mathbf{x} \equiv (x_1, x_2, \dots, x_N) \quad (24)$$

$$\boldsymbol{\xi} \equiv (\xi_1, \xi_2, \dots, \xi_N) \quad (25)$$

and

$$\boldsymbol{\xi} \cdot \mathbf{x} \equiv \xi_1 x_1 + \xi_2 x_2 + \dots + \xi_N x_N \quad (26)$$

being the scalar product of the two vectors.

The presence of the Dirac delta function in the integrand in (23) implies that the function $F(\boldsymbol{\xi}, p)$ contains only those contributions from $f(\mathbf{x})$ for which the end points of the vector \mathbf{x} are constrained to lie on the point

$$\boldsymbol{\xi} \cdot \mathbf{x} = p \quad (27)$$

If we now consider a two dimensional space, the locus is a straight line, whereas in a three dimensional space it is a plane. Generally one can say that the point is an $(N-1)$ -dimensional hyperplane (Π) in an N -dimensional space. For illustration purposes the three dimensional case is shown in figure 2.2.3.

This plane is perpendicular to the vector $\boldsymbol{\xi}$ and is pointed to by the end points of the \mathbf{x} -vectors. The distance of the plane from the origin, measured along the normal to the plane, is

$$d = \frac{p}{|\boldsymbol{\xi}|}. \quad (28)$$

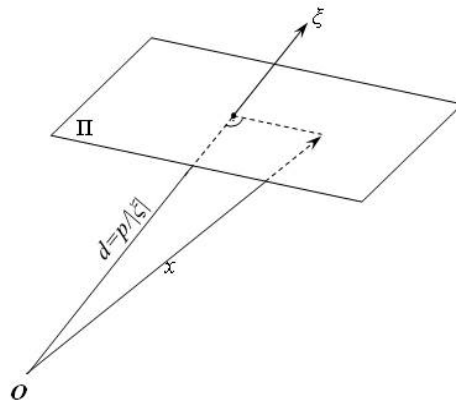


Fig. 2.2.3: Three dimensional illustration of the geometrical interpretation of Eq.26, where the plane Π is the locus of \mathbf{x} at the distance $d=p/|\boldsymbol{\xi}|$ from the origin O perpendicular to the vector $\boldsymbol{\xi}$.

A simple and rather useful property of the Radon transform is, if we consider β to be a real parameter different from zero

$$F(\beta\xi, \beta p) = \int f(\mathbf{x}) \delta(\beta p - \beta\xi \cdot \mathbf{x}) d^N x. \quad (29)$$

Using a known property of the Dirac delta function and the definition (23) one obtains the formula

$$F(\beta\xi, \beta p) = \frac{1}{|\beta|} F(\xi, p). \quad (30)$$

This equation (30) is also known as the scaling law for Radon transforms.

Due to the simple property of Eq. (30) we may restrict ξ , without loss of generality, to be an N-dimensional real unit-vector $\mathbf{n}^2 \equiv (n_1^2, n_2^2, \dots, n_N^2)$,

$$\mathbf{n}^2 \equiv n_1^2 + n_2^2 + \dots + n_N^2 = 1 \quad (31)$$

and employ, instead of (23) the following definition of the Radon transform of $f(\mathbf{x})$:

$$F(\mathbf{n}, p) = \int f(\mathbf{x}) \delta(p - \mathbf{n} \cdot \mathbf{x}) d^N x \quad (32)$$

which is the standard form of the *Radon transform*.

The function $F(\mathbf{n}, p)$ represents the projection of $f(\mathbf{x})$ onto the direction specified by the unit vector \mathbf{n} , and is the set of integrals of $f(\mathbf{x})$, labeled by p , taken over all hyperplanes defined by the equation

$$\mathbf{n} \cdot \mathbf{x} = p, \quad (\mathbf{n}^2 = 1) \quad (33)$$

at a fixed unit vector \mathbf{n} .

The integral on the left-hand side in equation (22) represents the Radon transform of the absorption coefficient $\alpha(\mathbf{r})$ in two dimensions, when the path of integration in (22) is taken along a line which is perpendicular to the unit vector \mathbf{n} at a distance p from the origin.

Knowing the initial intensity $I(P_0)$ and measuring the intensity $I(P)$ attenuated by an object at the detector plane, results the value of the ray integral of (22). This follows, that the reconstruction problem of tomographic

imaging using the Radon transform is the determination of the function $f(\mathbf{x})$, which often represents the absorption coefficient $\alpha(\mathbf{r})$, knowing a set of Radon transforms of $f(\mathbf{x})$ from a set of projections (ray integrals) of $f(\mathbf{x})$. This can be performed as follows.

The delta function in the integrand of equation (32) can also be written as a Fourier integral

$$\delta(p - \mathbf{n} \cdot \mathbf{x}) = \frac{1}{2\pi} \int_{-\infty}^{\infty} e^{-iu(p - \mathbf{n} \cdot \mathbf{x})} du \quad (34)$$

Substituting 34) into (32) and interchanging the order of integrations results in

$$F(\mathbf{n}, p) = \frac{1}{2\pi} \int_{-\infty}^{\infty} \tilde{f}(u\mathbf{n}) e^{-iup} du, \quad (35)$$

where $\tilde{f}(\mathbf{K})$ is the N-dimensional Fourier transform of $f(\mathbf{x})$, written as

$$\tilde{f}(\mathbf{K}) = \int f(\mathbf{x}) e^{-i\mathbf{K} \cdot \mathbf{x}} d^N \mathbf{x}. \quad (36)$$

Inverting equation (35) results the important formula

$$\tilde{f}(u\mathbf{n}) = \int_{-\infty}^{\infty} F(\mathbf{n}, p) e^{iup} dp. \quad (37)$$

This formula shows, that the N-dimensional Fourier transform $\tilde{f}(\mathbf{K})$ with the argument $\mathbf{K} = u\mathbf{n}$, of the unknown function $f(\mathbf{x})$ is just the one-dimensional Fourier transform, taken with respect to the scalar parameter p , of the Radon transform $F(\mathbf{n}, p)$ of $f(\mathbf{x})$. This result is independent to the x-space dimensionality N.

Knowing that the Radon transform $F(\mathbf{n}, p)$ represents the projection of the function $f(\mathbf{x})$ onto the direction \mathbf{n} , one can now continue with the reconstruction of the of the function $f(\mathbf{x})$. Knowing all projections of $f(\mathbf{x})$, and thus the equivalent Radon transform for all values of its arguments, one is now able to calculate all Fourier components $\tilde{f}(\mathbf{K})$ using equation (37), and by knowing these Fourier components, one can now synthesize the unknown function $f(\mathbf{x})$ by inverting eq. (36).

One special case to achieve a reconstruction of the absorption coefficient of a specimen is the arrangement of parallel projections in the case where the dimension of the domains of interest (planar cross-sections) equals $N = 2$. The transmitted intensity is then measured on lines which are perpendicular to the ray directions as depicted in figure 2.2.2.

It is convenient to denote the two-dimensional vector which specifies the points in the object by $\boldsymbol{\rho}$ (corresponding to \boldsymbol{x} in the general case) and denote its Cartesian components by x and y (rather than by x_1 and x_2), as presented in figure 2.2.4. and referring to the function $f(\boldsymbol{\rho})$ as the object function where, in this case, the quantities of interest are the absorption coefficient α or the fluorescence emission, respectively.

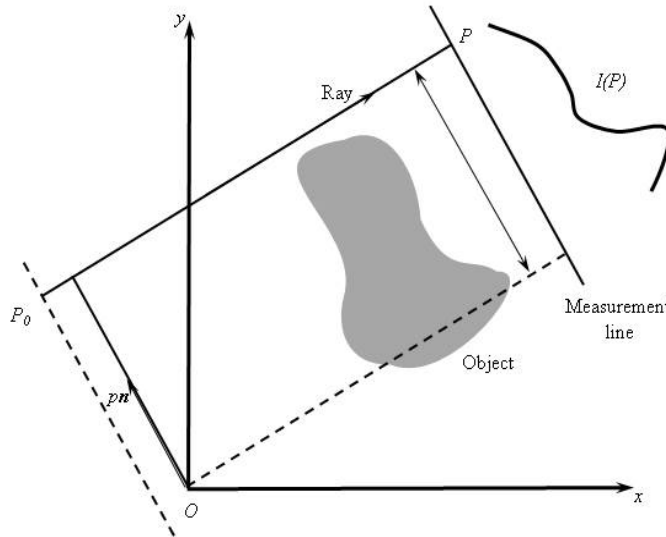


Fig. 2.2.4: Geometry and notation for the determination of a two-dimensional object function $f(\boldsymbol{\rho})$ from parallel projections.

The projection of the object function onto the unit \boldsymbol{n} direction perpendicular to the ray is given by the two-dimensional Radon transform

$$F(\boldsymbol{n}, p) = \int_{-\infty}^{\infty} f(\boldsymbol{\rho}) \delta(p - \boldsymbol{n} \cdot \boldsymbol{\rho}) d^2 \boldsymbol{\rho}, \quad (38)$$

The two-dimensional Fourier transform $\tilde{f}(\boldsymbol{\kappa})$ of $f(\boldsymbol{\rho})$, where $\boldsymbol{\kappa}$ denotes a two-dimensional vector analogue of the N-dimensional vector \mathbf{K} in Fourier space,

$$\tilde{f}(\boldsymbol{\kappa}) = \int f(\boldsymbol{\rho}) e^{i\boldsymbol{\kappa} \cdot \boldsymbol{\rho}} d^2 \rho, \quad (39)$$

and the one-dimensional Fourier transform of the Radon transform $F(\mathbf{n}, p)$ with respect to the p variable, which is

$$\tilde{F}(\mathbf{n}, u) = \int_{-\infty}^{\infty} F(\mathbf{n}, p) e^{iup} dp. \quad (40)$$

The compact form of Eq. 37 specialized for the two-dimensional case can now be written as

$$\tilde{f}(u\mathbf{n}) = \tilde{F}(\mathbf{n}, u), \quad (41)$$

which is often referred to as the slice along the \mathbf{n} direction in the Fourier domain (the $\boldsymbol{\kappa}$ -plane) of the object function $f(\boldsymbol{\rho})$.

This is the set of values of $\tilde{f}(u\mathbf{n})$ for all u values with a fixed direction \mathbf{n} . Eq. (41) then implies that the one-dimensional Fourier transform $\tilde{F}(\mathbf{n}, u)$ of the projection $F(\mathbf{n}, p)$ on \mathbf{n} of the object function $f(\boldsymbol{\rho})$ is equal to the slice $\tilde{f}(\boldsymbol{\kappa})$ of the object taken along the line $\boldsymbol{\kappa} = u\mathbf{n}$ through the origin of the Fourier domain. This statement is also known as the projection-slice theorem or the Fourier slice theorem.

Considering Eq. (41) one can now express the object function $f(\boldsymbol{\rho})$ in terms of its parallel projections in a more explicit form, which is more common to be used in practice.

Choosing a rectangular coordinate system with axes O_{x0} , O_{y0} in the x, y – plane and the angle enclosed by the unit normal \mathbf{n} and the positive x_0 -axis denoted with φ , as depicted in figure 2.2.5

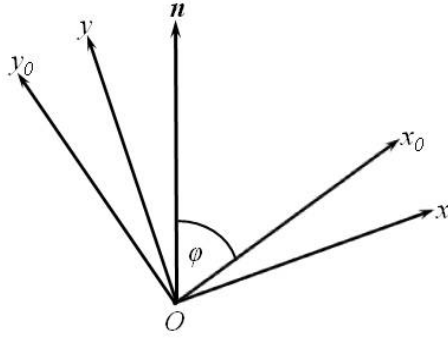


Fig. 2.2.5: Illustration of the notation to reconstruction of planar cross-sections of the object function $f(\boldsymbol{\rho})$.

results that

$$\mathbf{n} = \hat{\mathbf{x}}_0 \cos\varphi + \hat{\mathbf{y}}_0 \sin\varphi, \quad (42)$$

where $\hat{\mathbf{x}}_0$ and $\hat{\mathbf{y}}_0$ are the unit vectors along the x_0 and y_0 directions respectively, and

$$\tilde{f}(u\mathbf{n}) = \tilde{f}(u \cos\varphi, u \sin\varphi). \quad (43)$$

The inverse Fourier transform of Eq. (39) may then be written in the form

$$f(\boldsymbol{\rho}) = \frac{1}{(2\pi)^2} \int_0^{2\pi} d\varphi \int_0^{\infty} \tilde{f}(u \cos\varphi, u \sin\varphi) e^{-i u \mathbf{n} \cdot \boldsymbol{\rho}} u \, du. \quad (44)$$

If one now uses the relations $\cos(\varphi + \pi) = -\cos\varphi$, $\sin(\varphi + \pi) = -\sin\varphi$ and substituting for \tilde{f} on the right-hand side from the basic relation (41), then Eq. (44) becomes

$$f(\boldsymbol{\rho}) = \frac{1}{(2\pi)^2} \int_0^{2\pi} d\varphi \int_0^{\infty} F(\mathbf{n}, u) e^{-i u \mathbf{n} \cdot \boldsymbol{\rho}} |u| \, du. \quad (45)$$

where \mathbf{n} is given by Eq. (42).

To determine the unknown object function $f(\boldsymbol{\rho})$ throughout the $\boldsymbol{\rho}$ -plane from the one-dimensional Fourier transforms $\tilde{F}(\mathbf{n}, u)$ of the projections $F(\mathbf{n}, p)$ of $f(\boldsymbol{\rho})$ can now be done by using Eq. (45) which is called the *back-projection algorithm for parallel projections*.

Applying this in a tomographic setup, this could be measured for example by moving an infinite small single laser beam and a single pixel from a CCD camera used as the detector along parallel lines on the opposite sides of an object. A more practice orientated description is presented in figure 2.2.6. Considering a light sheet transmitted through an object, each grey value of a pixel in the corresponding row represents the integrated values and thereby the delta function of the appropriate volume of the sample. All projections of $\varphi_i \in [0^\circ, 360^\circ]$ of a single slice are denoted as the Radon transform.

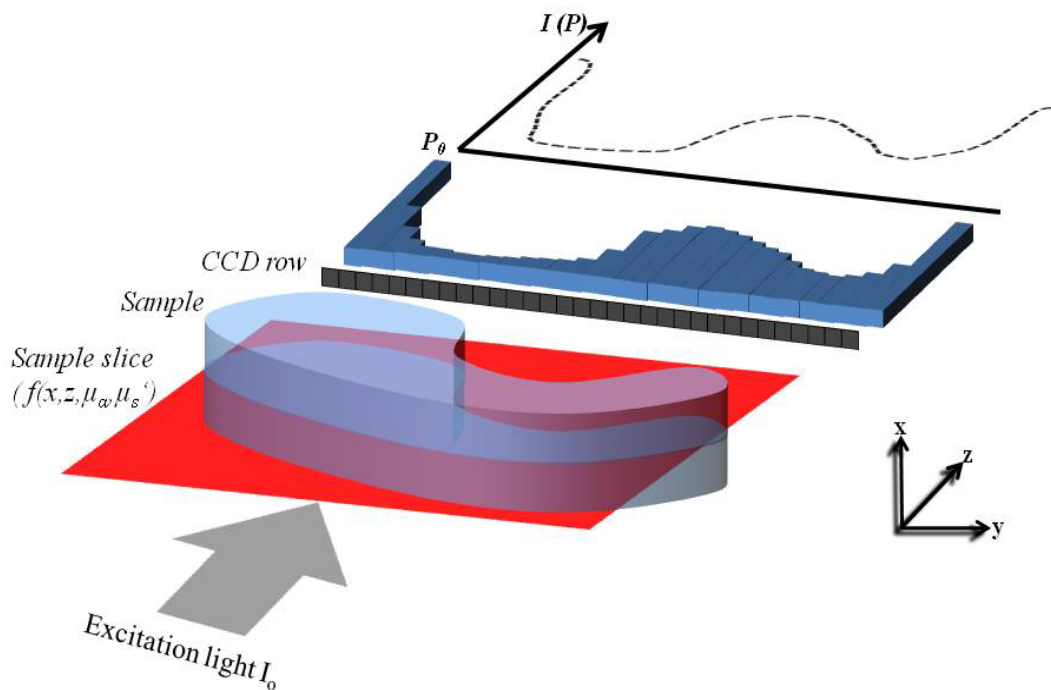


Fig. 2.2.6: Schematic of corresponding $I(P)$ of each pixel in a CCD row (which implies the corresponding radon transform) for a light sheet based illumination. Let's assume the illumination of a sample of given properties and a CCD as a detector. Each grey value of a pixel of the CCD corresponds a value $I(P)$ following equation (23). The Radon transform can then be written as $A(\xi, p) = \int \alpha(\mathbf{x}) \delta(p - \xi \cdot \mathbf{x}) d^N \mathbf{x}$ which, implemented in Beer's law gives $I(\xi, p) = I_0 e^{-A(\xi, p)}$. Scattering can be neglected, since the mean free path length of a photon is larger than the samples size.

Figure 2.2.7 represents the reconstruction formation in a single slice for the fluorescence data of the salivary glands from a drosophila larva for an

increasing number of projections. In contrast to the result from 500 projections, in the result for 128 and 256 projections, the salivary gland on the left seems to disappear due to missing contributing projections. This can happen for areas of interest which are partially covered by highly absorbing areas in contributing projections.

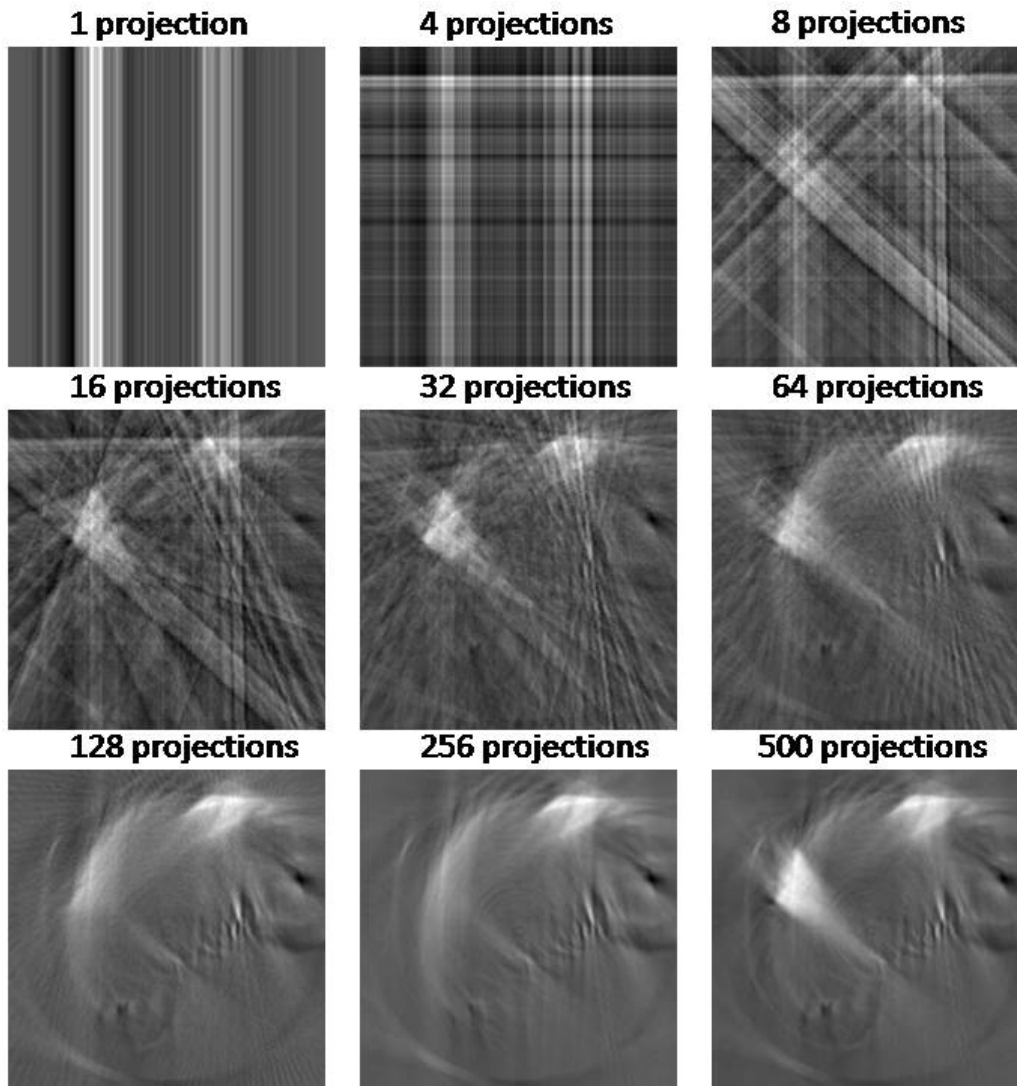


Fig. 2.2.7: Backprojection for different number of projections. An increasing number of added projections ameliorate the image quality. In contrast to the result from 500 projections, in the result for 128 and 256 projections, the salivary gland on the left seems to disappear due to missing contributing projections from areas that are not covered by areas of high absorption.

2.3 OPTICAL RESOLUTION

Considering a perfectly accurate optical system, the resolving power is only limited by the diffraction of light. Figure 2.3.1 presents the result obtained by diffraction of a laser beam on a circular aperture. The lateral resolution is defined by the diameter of the first minimum of the diffraction pattern, the Airy disc. This represents the minimum distance of two enclosed objects that can be resolved,

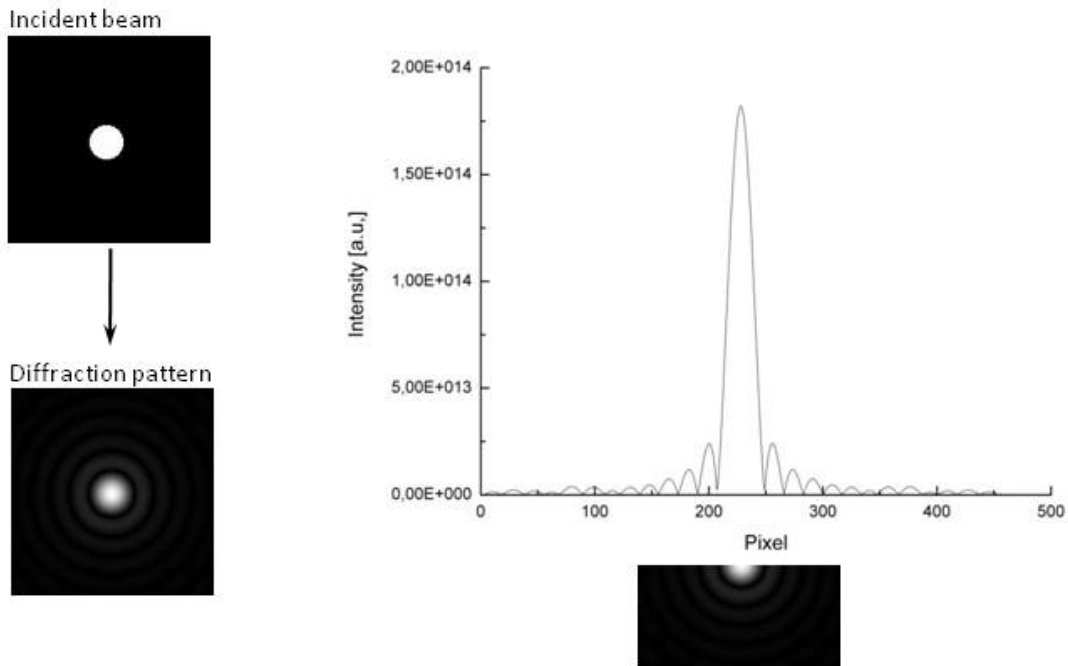


Fig. 2.3.1: Diffraction pattern of a laser beam from a circular aperture

The resolving power of an imaging system is mainly influenced by the objective properties and the tube lens system, or in case of implemented in a microscope setup, by the microscopes properties. It can be described by the Rayleigh criterion, which is:

$$R = \frac{1.22 \lambda}{2n \sin \alpha} \quad (46)$$

with λ being the wavelength, n the refractive index of the medium (air = 1) and α the half cone angle of the objective [70], where $n \sin \alpha$ represents the numerical aperture (NA) of the objective. R denotes the resolution and hence

the spot size of an imaging system. Since high focal depth (DOF) is required to enable large samples to be completely in focus, the axial resolution of the system decreases extremely. But contrarily to common 3D microscopic imaging technique, tomographic imaging does not rely on high axial resolution, but in this case on parallel beam rays. The resolution is only defined by the lateral resolution.

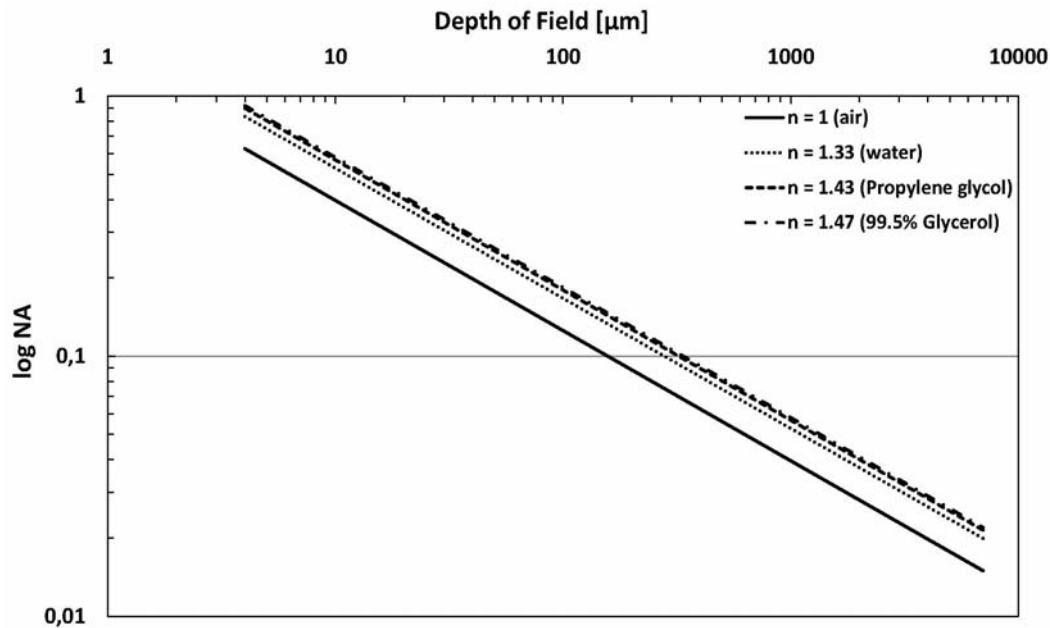


Fig. 2.3.2: Dependence of the numerical aperture from the variation of the depth of field in the presence of air and immersion liquids with different refractive indices n . The logarithmic scale is chosen for illustration purposes. The numerical aperture defined by the optical system is constant. The only change is the immersion liquid inside the capillary in which the specimen of interest is embedded, and the surrounding medium of the capillary.

In order to achieve true parallel projections from the object of interest, an introduction of a variable aperture in the back focal plane (see figure 2.3.3) of the objective lens has shown great advantage. In previously published work, the focal plane of the objective lens has been placed between the object's surface and the rotation axis, thus, the data obtained is influenced by scattering events from the non-focal areas of the object (see also [23]).

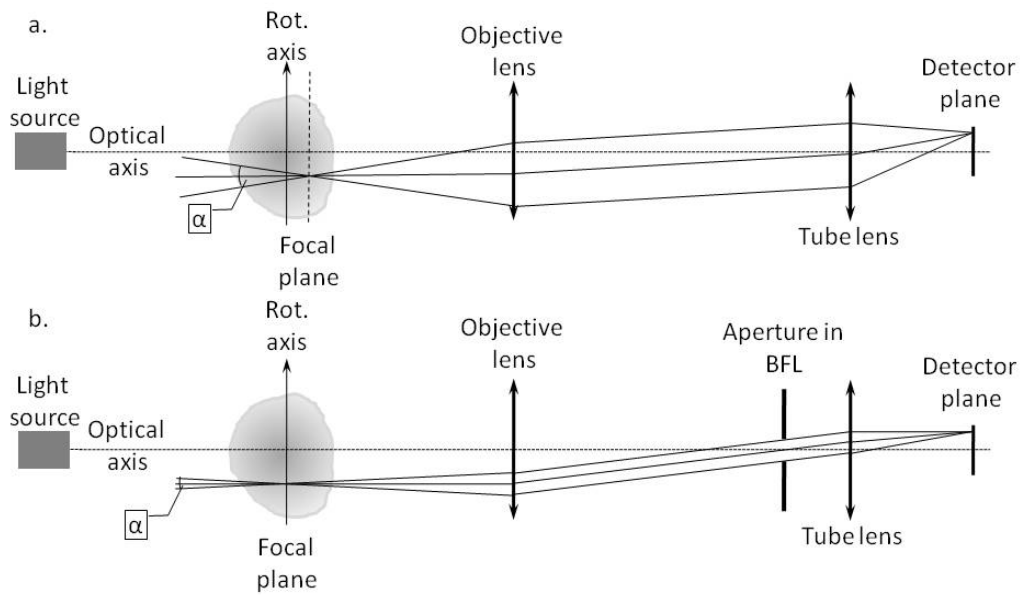


Fig. 2.3.3: Schematic of a conventional OPT setup a) and the improved OPT setup used in this work b). Note that in depiction b) the rotation axis and focal plane overlap. The advantage of application b) is the extended depth of field over the whole specimen, which results that the specimen is completely in focus. Contrarily application a.) results in noise from out of focus light, which consequently will disturb reconstruction images.

The influence of the increased focal depth on the numerical aperture of the objective lens, and hence the lateral resolution of the system, is shown in figure 2.3.4.

Additionally, the implementation of a variable aperture permits the adaption of the required focal depth for different objective lenses, and thus, the object size. A major drawback though, is the reduction in collected light, which means that the acquisition time for each projection, has to be increased. Hence, the projections acquired represent data which were completely in focus.

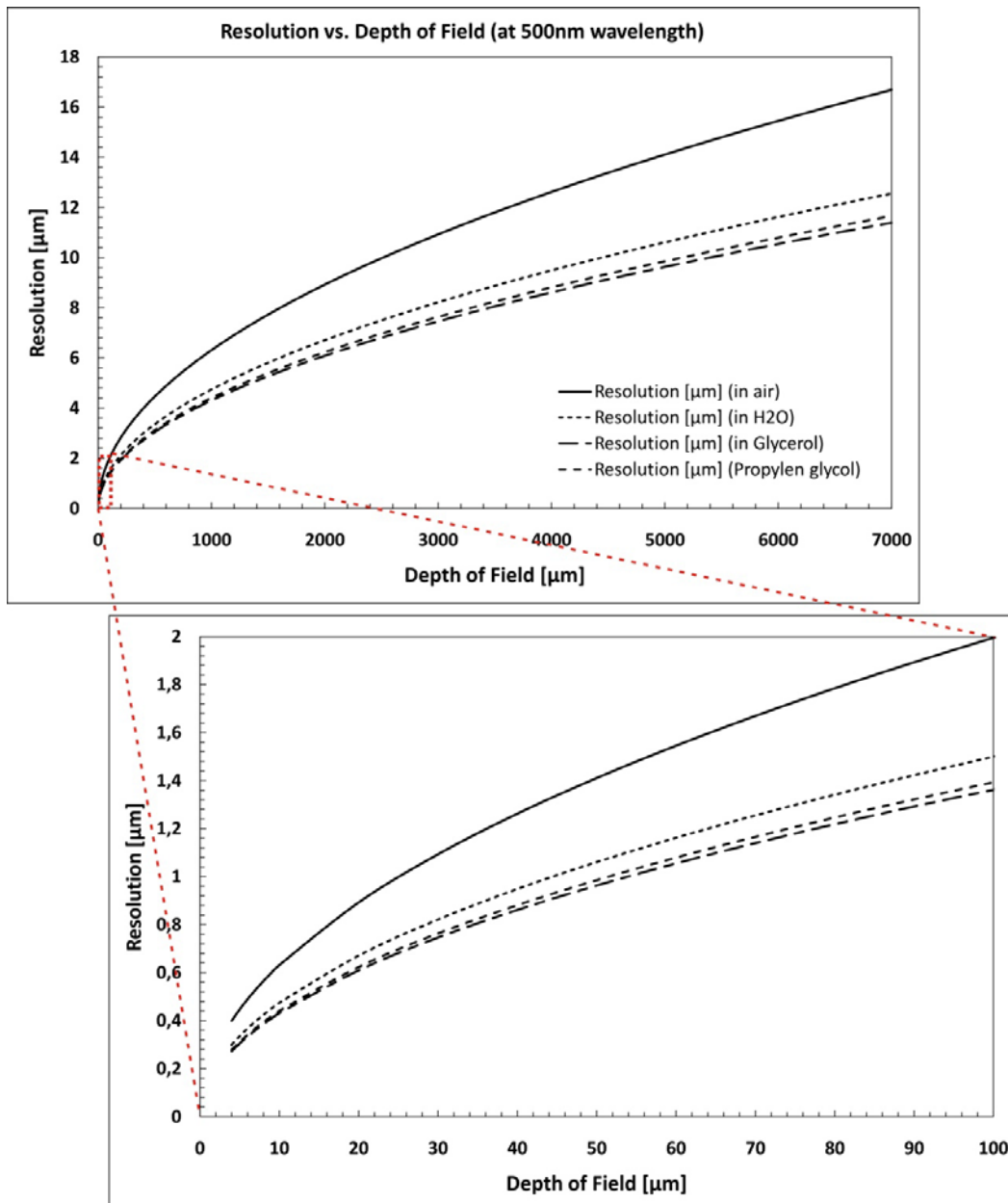


Fig. 2.3.4: Refractive index dependent resolution vs. the depth of field (Rayleigh range) at 500nm emission wavelength in the presence of various environmental media in which the specimen could be immersed. The upper graph shows the calculated refractive index dependent resolution versus Rayleigh range from 4 μm to 7mm, whereas, for better representation, the lower graph depicts the Rayleigh range from 4 μm to 100 μm (solid line: medium air ($n=1$); dotted line: medium H₂O ($n=1.33$); small dashed line: medium propylene glycol ($n=1.432$); long dashed line: medium 99.5% glycerol ($n=1.474$)).

Considering sample sizes of 100 μm for *C. elegans* and 500 μm for large samples i.e. *D. melanogaster*, and a center wavelength of 520 \pm 12.5nm given by the emission filter, one can now calculate the spot size of the imaging system by

$$w_0 = \sqrt{\frac{z_R \cdot \lambda}{\pi}} \quad (47)$$

where z_R is the Rayleigh range of the imaging system which has to be at least the length of the specimens width, λ is the wavelength given by the emission filter and w_0 is the beam waist and hence the spot size of the focus.

In case of a sample size of 100 μm the beam waist was calculated to be 4.086 \pm 0.055 μm whereas for the sample size of 500 μm the beam waist was 9.097 \pm 0.123 μm .

Figure 2.3.4 depicts the variation of the numerical aperture of an imaging system in the presence of different immersion liquids. Since the low alteration of the refractive index for commonly used immersion liquids, the axes of the graph are logarithmic scaled for illustration purposes. It is shown that imaging in presence of media with higher refractive indices one can achieve higher numerical apertures than in air, resulting in higher resolution while maintaining the depth of field.

Figure 2.3.5 shows the refractive index dependent resolution in respect to the wavelength used in an imaging system for a 10 μm depth of field. The refractive indices are $n = 1.33$ for water, $n = 1.47$ for 99.5% glycerol and $n = 1.432$ for propylene glycol.

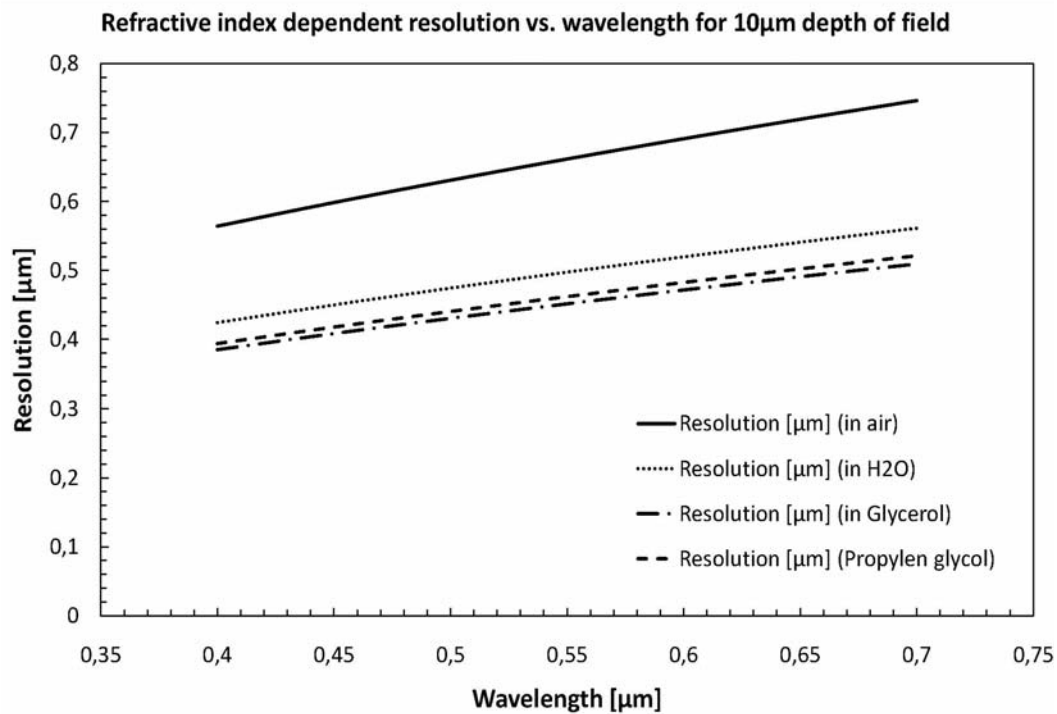


Fig. 2.3.5: Refractive index dependent resolution vs. the emitted wavelength at a depth of field (Rayleigh range) of 10 μ m for various environmental media in which the specimen could be immersed.

Optimal reconstructions were achieved with values of α varying from 5.74° for 0.1 NA to 4.47° for 0.078 NA and 2° for 0.035 NA where α is the cone angle (depicted in fig. 2.3.2.) which is defined by the focal length f of the objective and the diameter of the iris in the back focal plane by D/f . The calculated values for α are in good agreement with recently published experimental data [22, 71] and [23].

Figure 2.3.6 represents the principle of optical projection tomography. The light is projected onto the sample passing through a diffuser to acquire a homogeneous illumination.

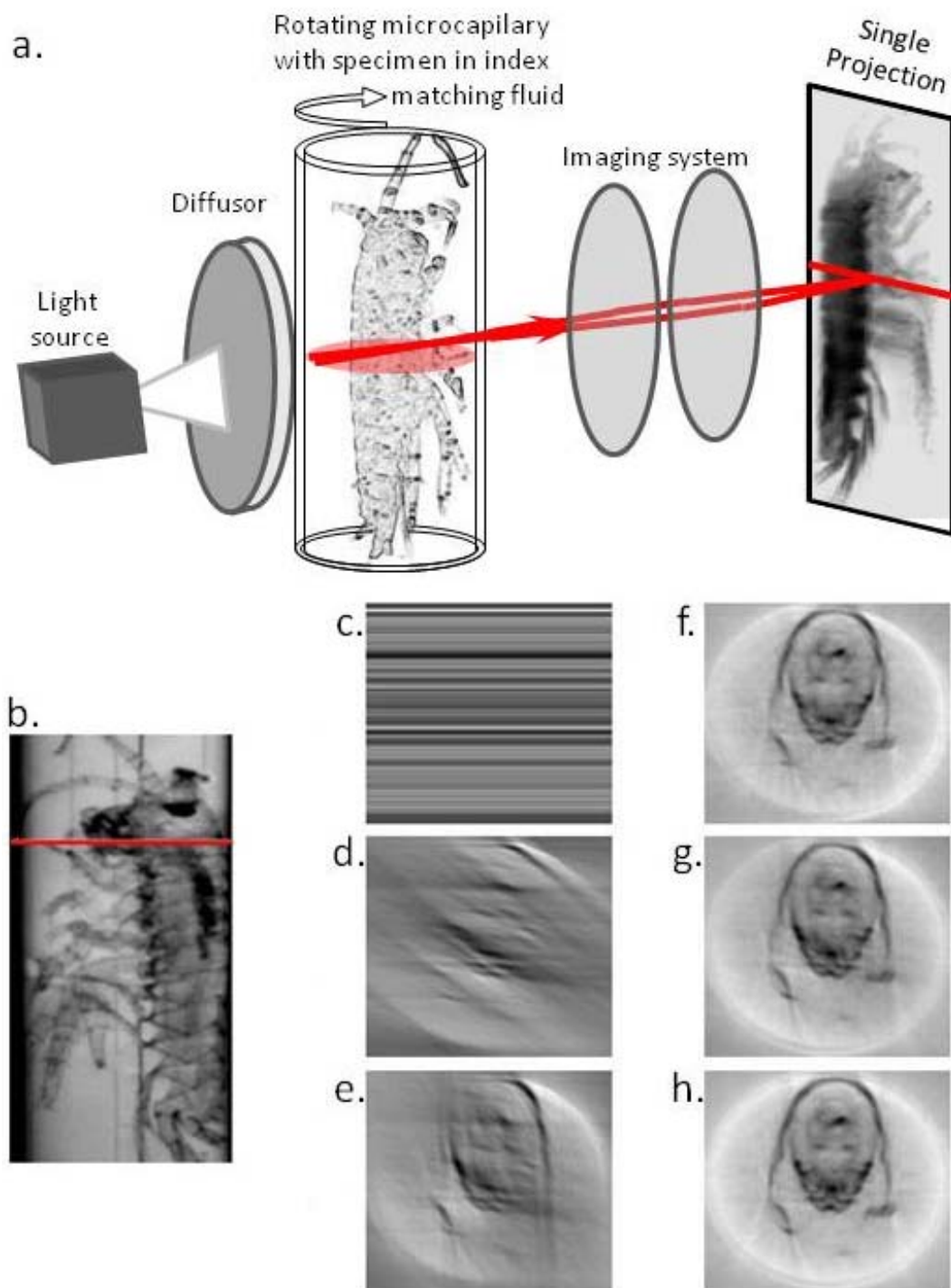


Fig. 2.3.6: a) principle of optical projection tomography, b.) raw transmission data of a *Parhyale hawaiiensis*, c) - h) filtered back projection of the marked area (red line in depiction b)) for 0°, 45°, 90°, 180°, 270° and 360° (one full revolution corresponds to 500 projections. Note that, in contrast to previous publications, there's still an increase in the reconstructed details from inset f) – h).

2.4 FREQUENCY WINDOWS

For back projection data acquired with OPT, one uses a filtered back projection method. To acquire the value of a point $b(x)$, all values of the Fourier transformed projections which cross each other in that specific point have to be summed up, which then results in a tomogram if the inverse Fourier transform of $r(u, \varphi)$ is applied. The drawback of the summation results in a diverse amplitude weighting in the Fourier space, thus rays closer to the center of rotation take a higher weighting than rays which are further away. In correspondence to the original image, this results in higher weighting of the frequency shares in the center of the Fourier transform, which represents the low frequency signals in the back projected image. Therefore, low frequency signals in the frequency domain acquire intensified amplitude contrary to high frequency signals, which results in an image blur (see figures 2.4.1.a and 2.4.2.a).

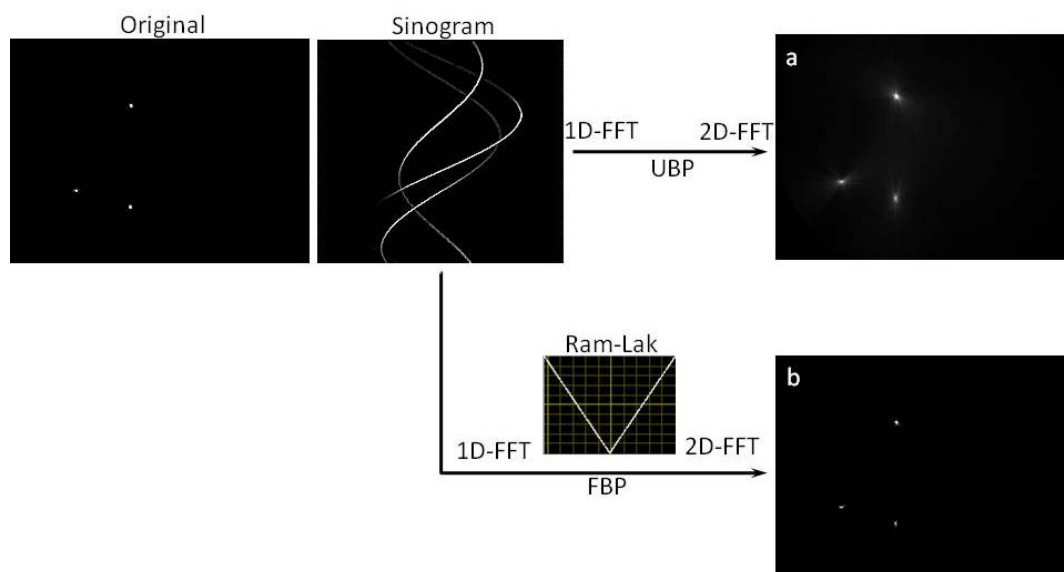


Fig. 2.4.1: a) unfiltered backprojection (UBP) image of the original, and b) the filtered backprojection (FBP) image using a Ram-Lak filter. All projections of one slice can be placed in an image and result in a sinogram. It represents the projection of each point in a specimen at every angle of acquisition. The Fourier filter suppresses low frequencies since these do not contribute in high details in the reconstruction, as depicted in inset a).

Figure 2.4.2 constitutes the image blur using an unfiltered back projection (a) and a filtered backprojection using a Ram-Lak filter (b). Both images are taken from an early stage pupa of *Drosophila melanogaster* exhibiting the GFP fluorescence in the salivary glands.

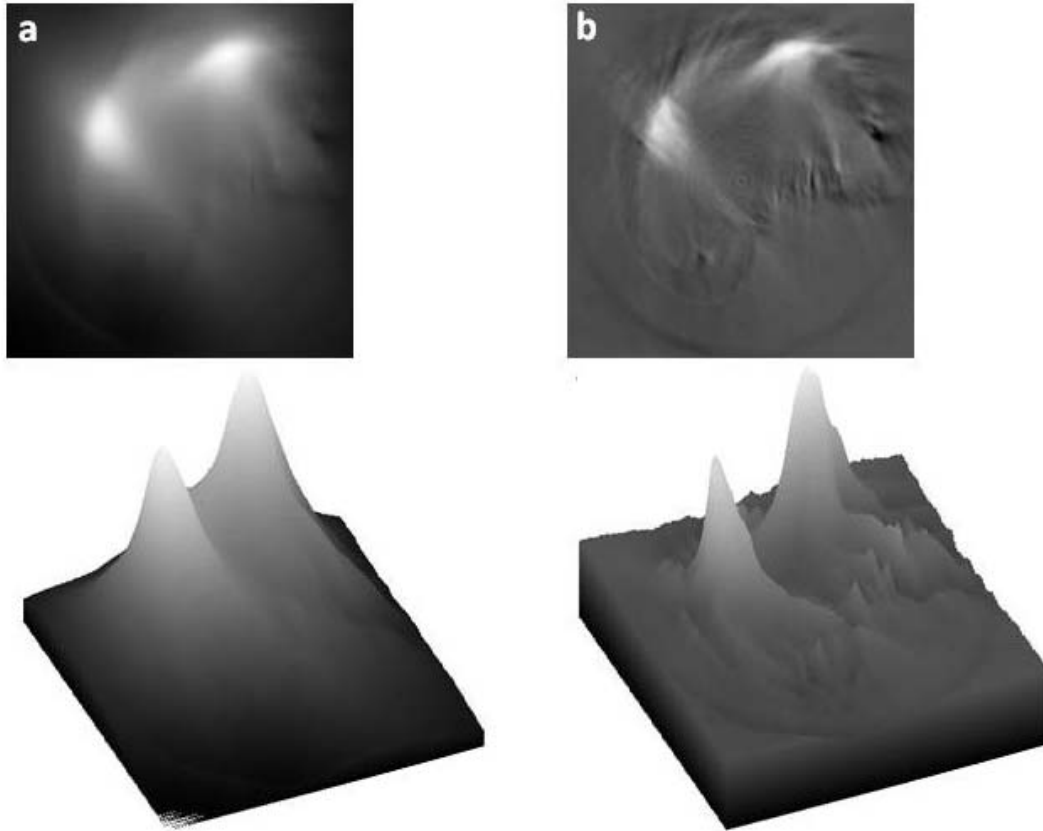


Fig. 2.4.2: Reconstructed slice of the fluorescent salivary glands from a *Drosophila melanogaster* early stage pupa, a.) unfiltered backprojection, b.) filtered backprojection using a Ram-Lak filter (ramp filter) and corresponding surface plots. Note the enhanced detail in the filtered backprojection of b.) by suppressing low frequencies in the Fourier domain in contrast to the high contribution of low frequencies in a.) which result in fuzzy reconstructions. The lower depictions of a) and b) are the corresponding 3D surface plots of the intensities of a) and b).

Considering its application in real data sets, the filtered backprojection in combination with a ramp filter (Ram-Lak filter) is not a straight forward solution, since it only solves the problem of fuzziness from the unfiltered backprojection. The frequency response of a Ram-Lak filter is the absolute

value of $|f|$. Because this filter is sensitive to noise in the projections, it is often combined with a Hann or Hamming filter as depicted in figure 2.4.3. These filters multiply the Ram-Lak filter by a window that deemphasizes high frequencies. To resolve noise, another issue which goes together with signal detection, other filters have shown increased benefit. Since the quenching of low frequencies by the Ram-Lak filter, other filters should provide conformation of the remaining frequency area, thus, also the parts which correspond to noise. In the reconstructions presented in this work, all data has been processed using a combination of a Ram-Lak and a Hann filter (figure 2.4.3.). This assures the maintenance of high frequencies but also good suppression of side lobes which arise as artifacts using only a Ram-Lak filter.

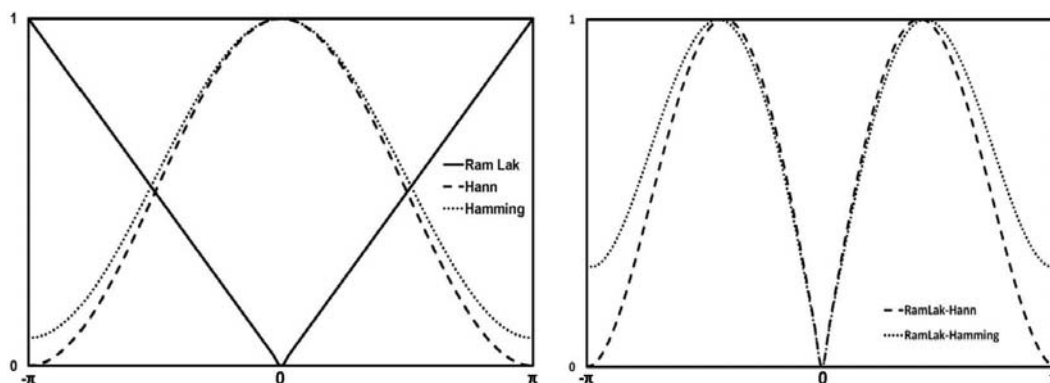


Fig. 2.4.3: Left: depiction of the frequency response of a Ram-Lak filter (solid line) Hann filter (dashed line) and Hamming filter (dotted line). The depiction on the right shows the frequency response combining Ram-Lak and Hann filter (dashed line) and combination of Ram-Lak and Hamming filter (dotted line).

2.5 SAMPLE ILLUMINATION

The sample illumination has been performed using a 5x beam expander in order to achieve a quasi-homogeneous illumination of the sample. As shown in figure 2.5.1, the illumination with a straight laser beam is not sufficient to enable an illumination of the whole field of view of the imaging system, which would result in streak artifacts in the reconstructed data, since objects are not present in each projection. Another drawback would be a

weighting of the tissue optical properties due to inhomogeneous illumination. Objects closer to the center of rotation would take higher weighting in the grey values than objects further to the edge of the sample.

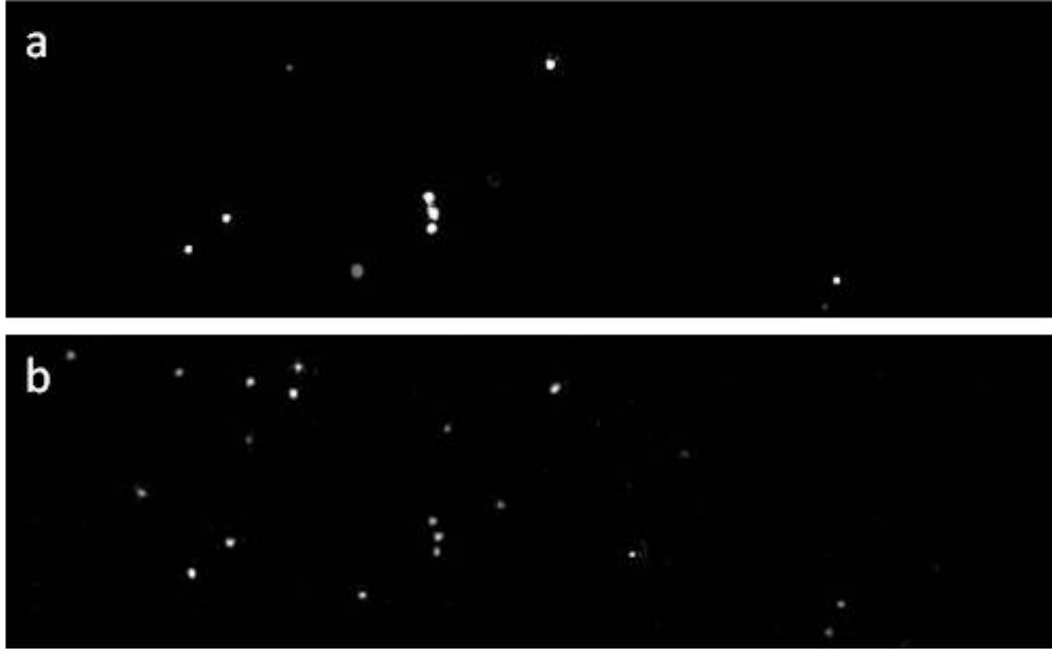


Fig. 2.5.1: Raw images of $3\mu\text{m}$ diameter GFP fluorescent microspheres embedded in 2% agarose solution in a $290\mu\text{m}$ O_{in} capillary with excitation from 473 nm laser, a.) illumination with straight beam (beam O 1mm), b.) illumination with 5x beam expander (beam O 5mm).

Figure 2.5.2 illustrates the intensity distribution in correspondence to the distance from the center of rotation for illumination using a straight laser beam (dashed line and crosses) in contrast to illumination using a 5x beam expander (solid line and circles). This shows that light has to be homogenized in order to achieve a uniform illumination of the specimen and thereby a more quantified emission of a fluorescent probe. This goal also for the acquisition of a quantified absorption distribution of the specimen of interest.

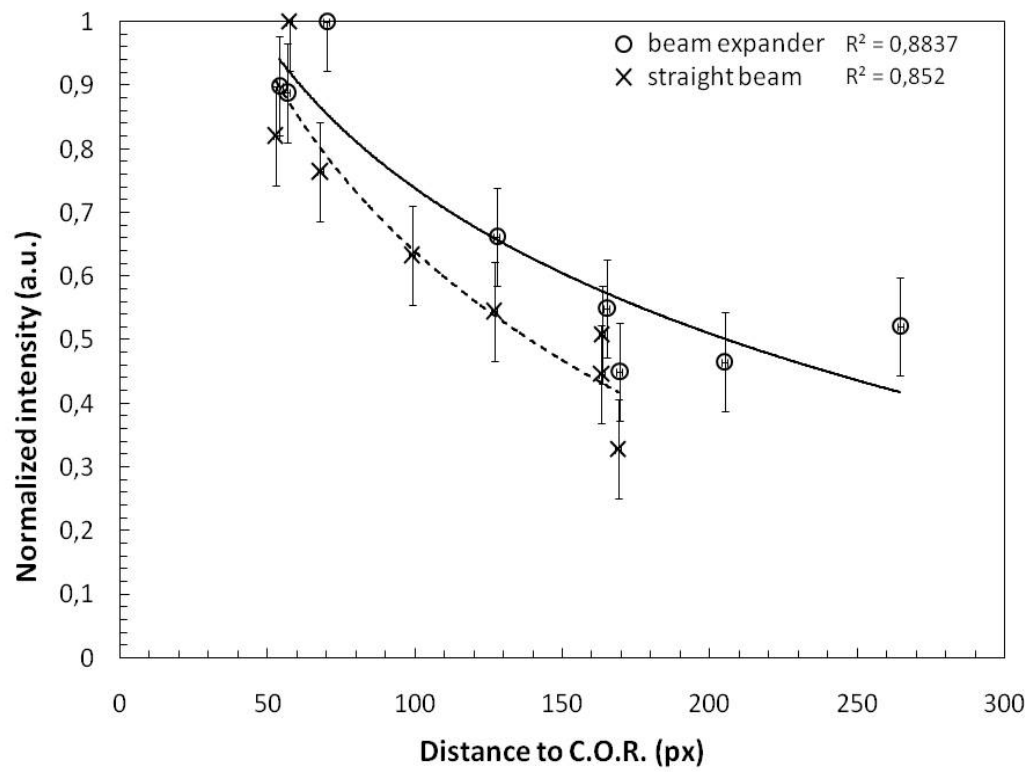


Fig. 2.5.2: Intensity distribution in correspondence to the distance from the center of rotation. Illumination using a straight laser beam (dashed line and crosses) in contrast to illumination using a 5x beam expander (solid line and circles).

3 MATERIALS AND METHODS

3.1 OPT EXPERIMENTAL SETUP

The experimental setup shown in Fig. 1 consists of two DPSS Lasers (100mW cw emitting at 473nm and 30mW cw emitting at 532nm, Laserlight, *Berlin/Germany*) [i.]. A fast laser shutter (LS 6, UniBlitz, *Rochester, NY*) [ii.], and a 5x beam expander (Edmund Optics Inc., *Karlsruhe/Germany*) [iii.] which is used to control the beam exposure and to enlarge the beam from 2mm to a 10mm spot size for quasi homogeneous illumination of the area of interest. The sample holder is based on a rotation system, containing a stepper motor (Oriental Motors) [iv.] with 500 steps per revolution with a custom made capillary holder that can accommodate standard single-use micro capillaries. with a refractive index $n_D = 1.474$ at 589 nm (Blaubrand® - intraMARK, BRAND GmbH, *Wertheim, Germany*) with inner diameters of 0.29mm (1-5 μ l), 0.58mm (20 μ l), 0.91mm (50 μ l) and 1.19 mm (100 μ l). This capillary is immersed in a custom made index matching vessel [vi.] using 50x24x0.15mm borosilicate cover slips ($n_D = 1.474$ at 589 nm) containing 87% glycerol solution as an index matching fluid ($n_D = 1.47$ at 589 nm) or halo carbon oil to minimize internal reflection and refraction of the excitation and emission light. The imaging unit consists of a lens tube system (InfiniTube™, Infinity, *Boulder CO., USA*) [x.] containing a custom made filter slide [viii.] for 25mm dia. fluorescence filters (525 \pm 17.5nm for GFP, 593 \pm 20nm for dsRed, both Semrock®, *Rochester NY., USA*). At the sample side of this tube we may optionally attach a 5x (NA 0.14) or a 10x (NA 0.28) infinity corrected microscope objective [vii.] (Mitutoyo, *Kawasaki, Japan*), whose choice were given by the sample size and therefore the required field of view, finally having a TE cooled intensified CCD with 1002 x 1004 pixel

resolution [xi.] (DV885 ANDOR™Technology, *Belfast, Northern Ireland*) at the image side. The focal depth of the system can be selected using a variable aperture [ix.] that has been placed behind the microscope objective [22]. An x-y-z translation stage system [3 x 8MT167-100, STANDA, *Vilnius/Lithuania*] was applied to control the sample position with respect to the optical setup.

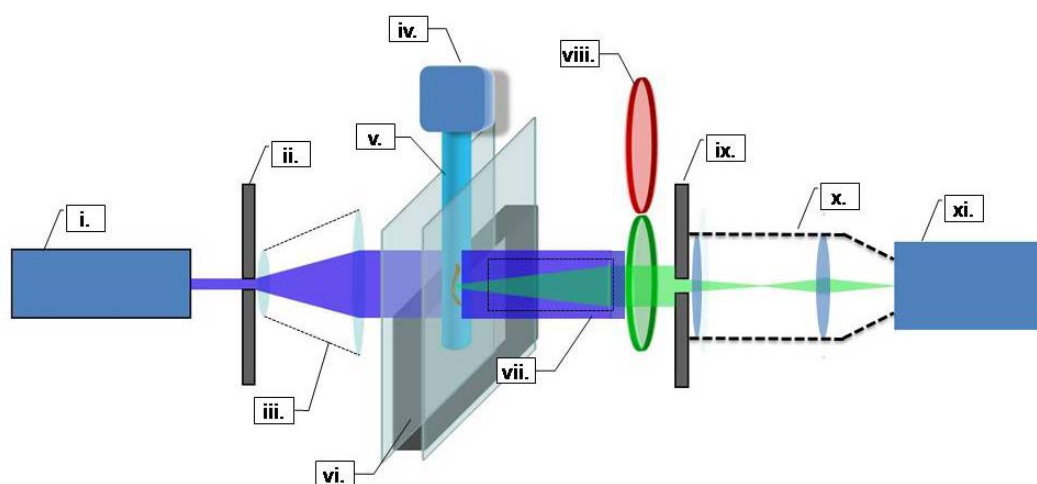


Fig. 3.1.1: Schematic drawing of the OPT setup, [i.] laser, [ii.] shutter, [iii.] beam expander, [iv.] stepper motor, [v.] capillary mount with micro capillary, [vi.] index matching vessel, [vii.] microscope objective, [viii.] filter slide with fluorescence filters, [ix.] variable aperture, [x.] lens tube system, [xi.] ICCD camera.

The iris [ix.] at the back focal plane of the objective lens reduces the detected divergence of the transmitted and emitted light to true parallel beams. This leads to low numerical apertures of the imaging system, thus also to the drawback of the reduction in lateral resolution as described in section 2.3.

Figure 3.1.2 represents the detailed laboratory OPT setup simulated with Autodesk Inventor®.

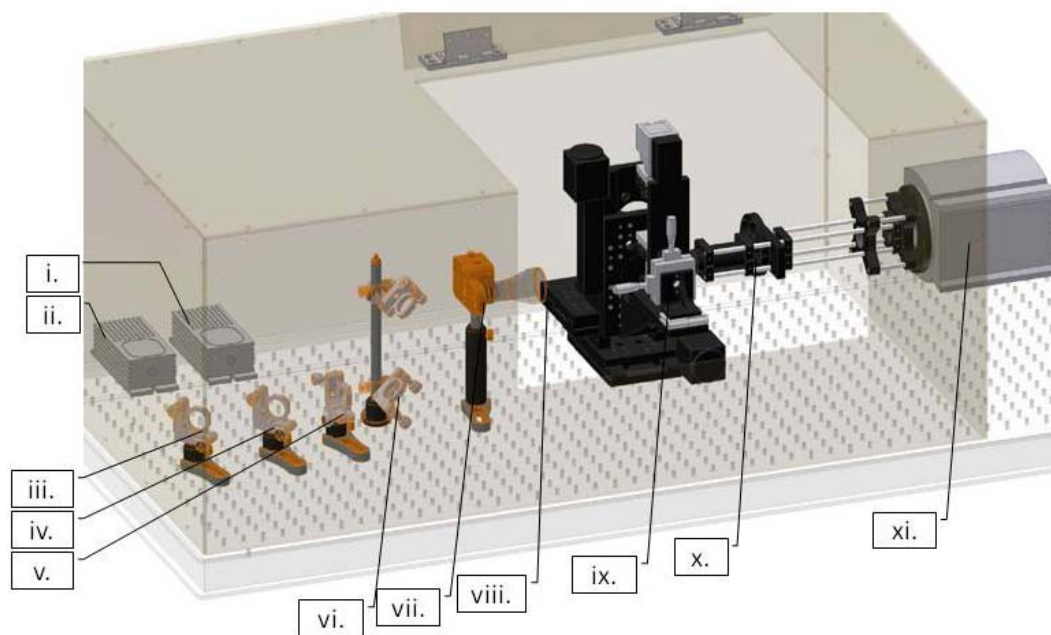


Fig. 3.1.2: Detailed laboratory OPT setup, *i.*) 473nm DPSS laser, *ii.*) 532nm DPSS laser, *iii.*) HR mirror (473nm), *iv.*) dichroic mirror (HR 532nm/T 473nm), *v.* IR filter, *vi.*) Periscope, *vii.* Shutter, *viii.*) 5x beam expander, *ix.*) x-y-z translation stage system in combination with high resolution stepper motor, sample holder and imaging vessel, *x.*) imaging system containing microscope objective, fluorescence filter and tube lens system, *xi.*) EMCCD camera.

The imaging system is completely isolated from ambient light by a 3mm blackened aluminum box (grayish transparent in fig 3.1.2), which is enclosed with a large lid for easy accessibility of all components. All motorized components are controlled by a custom LabView™ program. The stepper motor with the capillary holder is mounted on a hinge, so that the whole part could be flapped down for easy access and placement/replacement of the capillary holders and the micro capillary tube (see fig. 3.1.3). After assembling of a capillary containing a sample, the whole part is carefully lowered, so that the tube would not break the vessel windows. In case of misalignment, the holder can be precisely adjusted relatively to vessel by the y-z translation stages (see *iv.* in depiction 3.1.3 a.). After that, the whole probe holder has to be aligned relatively to the optical axis by the x-y-z translation

system (*i.*, *ii.*, *iii.* in depiction 3.1.3 a.) using the corresponding tool in our in house developed LabView™ program. While aligning the setup, the EMCCD can be cooled down to its working temperature of -85°C , which takes approximately five minutes. The next step is the bias of the capillary's rotation center, which is arranged by using the designated adjustment screws of the upper and lower capillary mount.

After that the optimum acquisition time has to be set, so that there is no saturation, but also ensuring, that the camera's whole dynamic range of 14 bit is used. A more detailed depiction of *ix.*) is shown in figure 3.1.3. The imaging vessel consists of a u-shaped stainless steel frame with two 24x50mm size 1 cover glasses (Marienfeld-Superior, *Lauda-Königshofen, Germany*), made of Borosilicate glass alike the micro capillary to achieve a proper refractive index match using 87% glycerol solution.

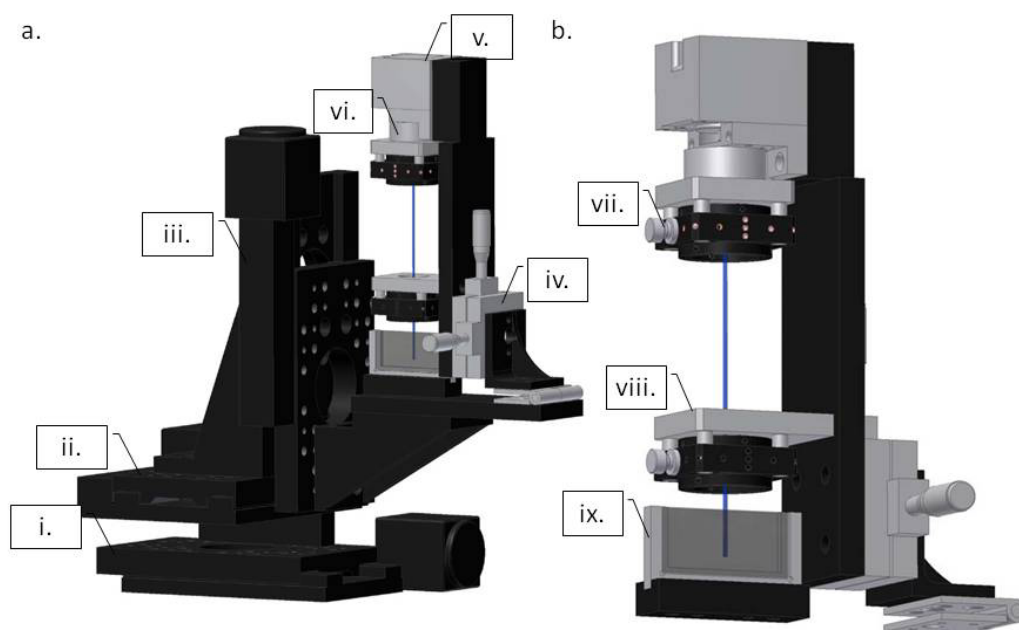


Fig. 3.1.3: Sample holder and imaging vessel, a.) *i.- iii.*) motorized x-y-z translation stages for positioning of the imaging vessel relatively to the optical axis of the imaging system, *vi.*) capillary holder, *v.* high resolution stepper motor, *iv.*) y-z fine adjustment of the capillary relatively to the imaging vessel, b.) *vii.*) upper adjustment of the rotation axis, *viii.*) lower adjustment of the rotation axis, *ix.*) imaging vessel.

3.2 CAMERA

The advantage of using binning is the reduction of signal noise and thereby an increase of the signal-to-noise ratio (SNR) which describes the information content. Whenever a detector is exposed to light, there is always a certain amount of noise associated with the image. Read noise is generated due to the process of downloading the image from a chip, which, due to imperfection of information transfer, creates an uncertain noise, which is intrinsically random and unavoidable. Another major noise source is the dark noise, which is reduced by cooling the temperature of the CCD chip respectively to the ambient temperature.

The benefit of binning is the amplification of the signal-to-noise ratio. Considering that each pixel is noise afflicted, the adding of 4 pixels (as shown in figure 3.2.1) will result in an increased signal SNR by a factor $(4 \cdot \text{signal} / \sqrt{4 \cdot \text{noise}})$ since larger pixel areas constitute larger SNR's. Noise adds as the square root since it's a random process. This results in a higher sensitivity of the camera.

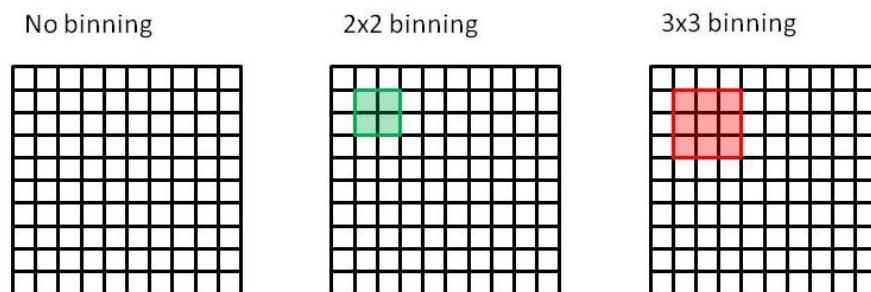


Fig. 3.2.1: Schematic of a binning procedure, no binning (left), 2 by 2 binning (center) and 3 by 3 binning (right).

Although binning increases the SNR, its drawback is the loss of resolution. Larger pixels detect more portions of an object. Thus, this always requires an agreement between resolution and signal detection.

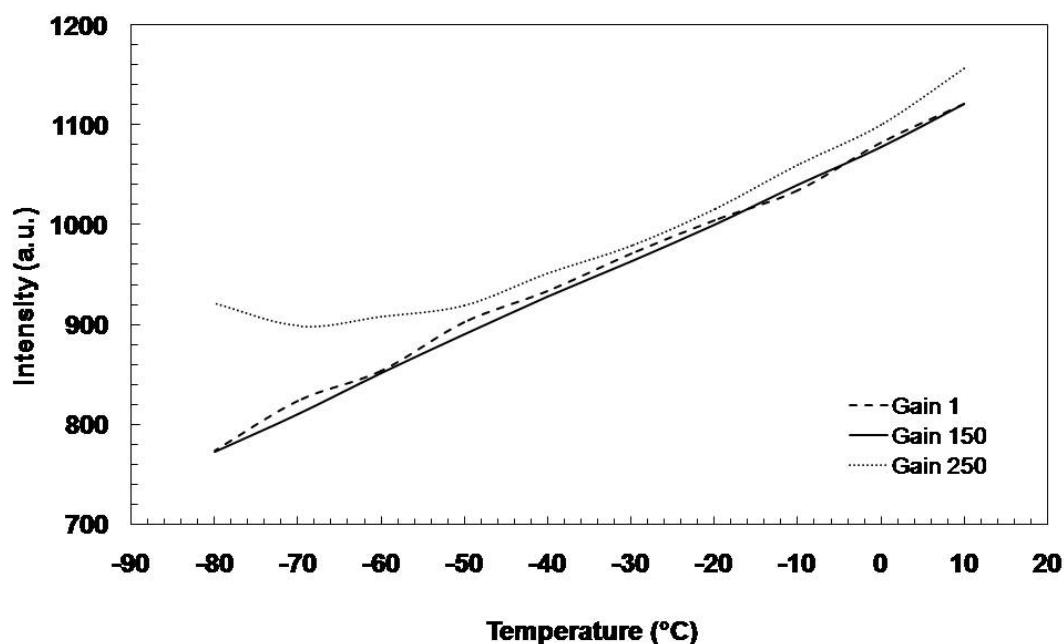


Fig. 3.2.2: Subjection of the mean background intensity in dependence of cooling temperature for commonly used electron multiplier gains. Mean Background Intensity for gain 1, 150, 250.

3.3 FLUORESCENT FILTERS

Fluorescence filters have been chosen according to the emission spectra of the used fluorescent proteins, namely eGFP and dsRed. Figures 3.5.3 and 3.5.4 represent the excitation and emission spectra of eGFP and dsRed in combination with the applied fluorescence filters. The suppression of the excitation light was given by the manufacturer's specifications to be at least 5-6 optical densities (O.D.).

The shift of the emission spectrum of dsRed to the red made it applicable for *in vivo* studies in organisms and tissues since due to a reduced absorption of oxyhaemoglobin as shown in figure 3.7.2. However, it also has some major drawbacks, such as strong oligomerization and slow maturation and in contrast to GFP or other green fluorescent proteins or probes, its emission is more influenced by hemoglobin and oxyhemoglobine.

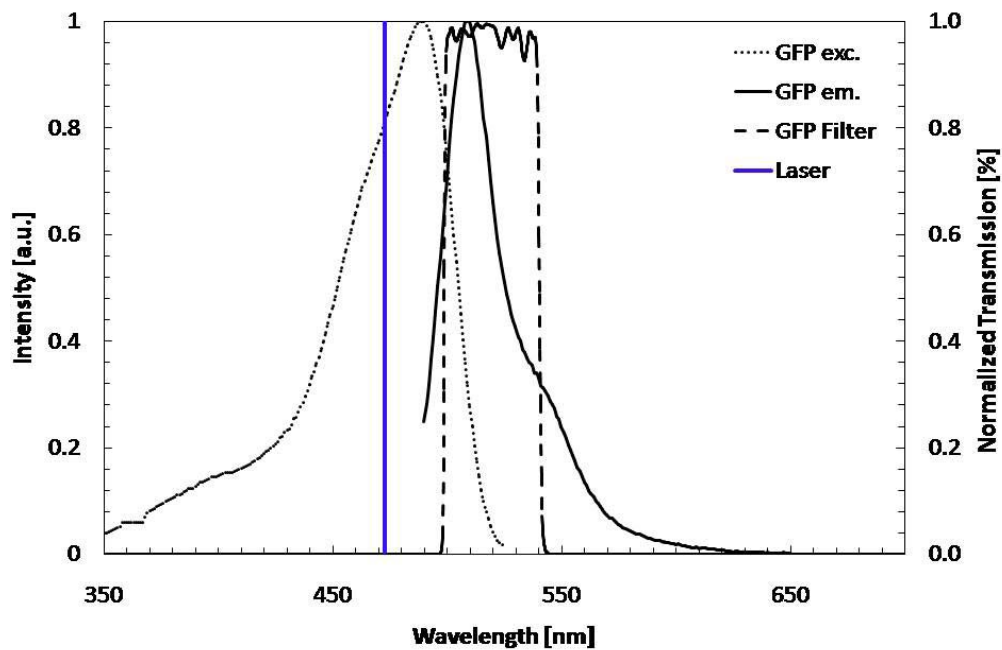


Fig. 3.3.1: Excitation (dotted) and emission (solid) spectra for eGFP. Excitation was provided by a 473nm DPSS laser (blue line) and fluorescence signal detection by a single band fluorescence filter (Semrock FF01-520/35-25)

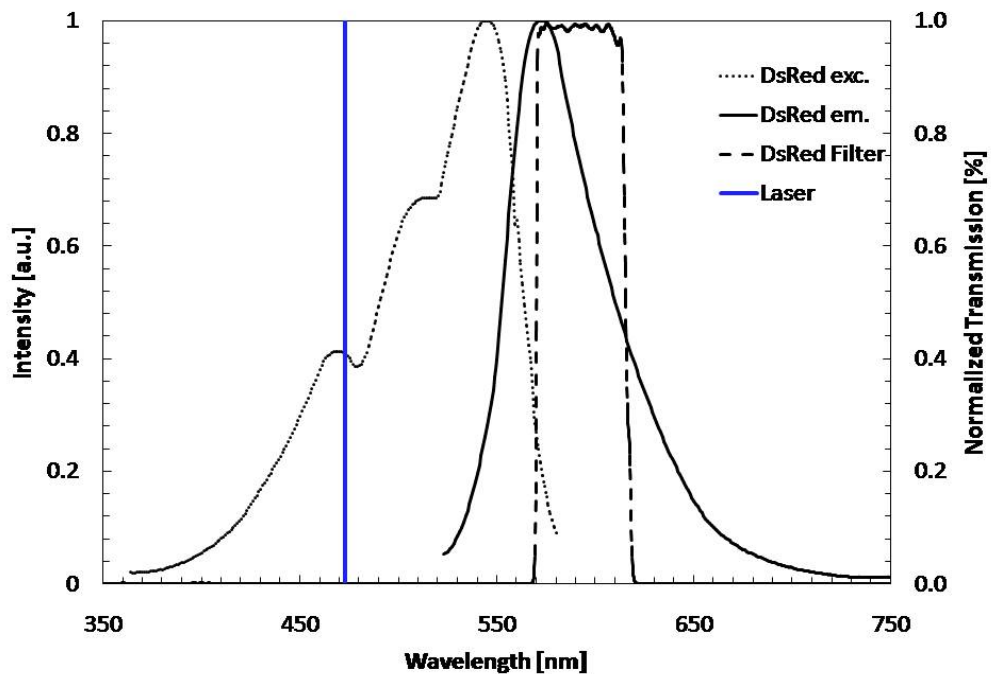


Fig. 3.3.2: Excitation (dotted) and emission (solid) spectra for dsRed. Excitation was provided by a 473nm DPSS laser (blue line) and fluorescence signal detection by a single band fluorescence filter (Semrock FF01-593/40-25).

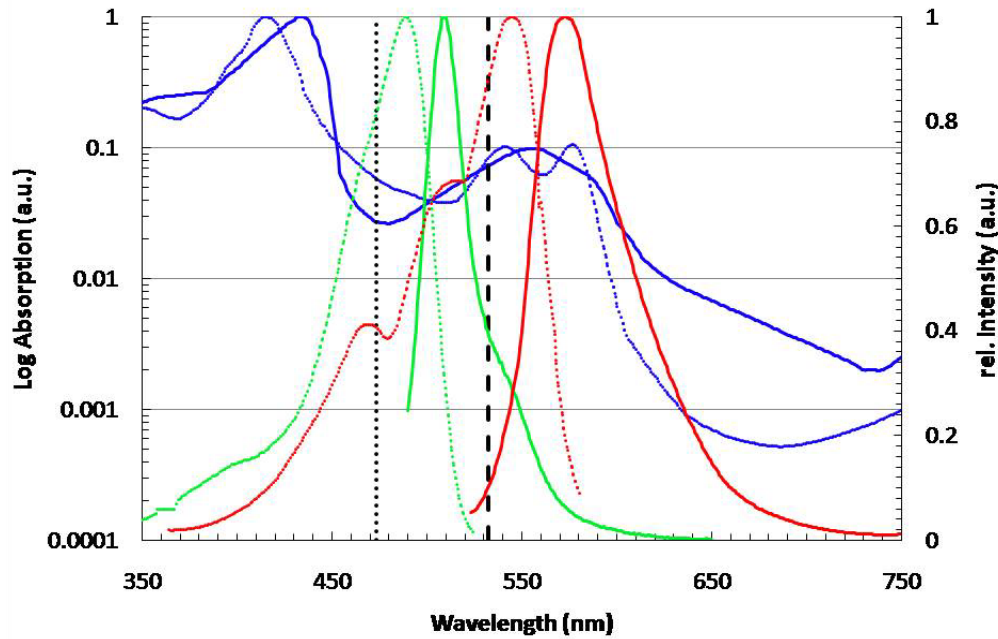


Fig. 3.3.3: Fluorescence spectra of GFP absorption (dotted green) and emission (solid green), dsRed absorption (dotted red) and emission (solid red) as well as the log scaled absorption of HbO₂ (dotted blue) and Hb (solid blue). The two vertical lines represent the possible laser lines for the excitation of the fluorescent proteins of 473nm (dotted) and 532nm (dashed). Note that the absorption of dsRed is reduced by one order of magnitude.

3.4 SAMPLE PREPARATION

In previously published OPT results on samples in the mm scale [3, 19, 20, 67], BABB (benzyl alcohol-benzyl benzoate), i.e. Murray's clear, was used to change the opacity of the sample. This eases the signal acquisition and significantly reduces the scattering present in the sample, but does not allow *in vivo* imaging. Since our goal is *in vivo* imaging, different procedures of sample preparation had to be investigated. Using an 87% glycerol solution or Halocarbon Oil 700 (Sigma-Aldrich, *Saint-Luis (MO), USA*) we found provided several advantages since it can be applied as index matching fluid, having an index of refraction of $n_D = 1.47$ at 589 nm. In early experiments, large samples such as *Drosophila melanogaster* in various developmental states have been placed in 87% glycerol solution as index matching fluid, later

in Halocarbon oil. According to [72] the organisms are alive for a period of at least 3 hours and therefore during the whole duration of the measurements (typically 5 minutes per channel). However this method should not be considered equally to common tissue clearing methods such as using BABB or MSBB, but rather an index matching method between the probe surface and the capillary. As mentioned previously, the specimens are placed in standard single use micro-capillaries with refraction index $n_D = 1.474$ at 589 nm (Blaubrand® - intraMARK, BRAND GmbH, *Wertheim, Germany*) with inner diameters of 0.29mm (1-5 μ l), 0.58mm (20 μ l) and 1.19 mm (100 μ l). This capillary is immersed in a custom made index matching vessel (see [vi.] in Fig. 3.1.3 inset b.) using 50x24x0.15mm borosilicate cover slips ($n_D = 1.474$ at 589 nm) containing 87% glycerol solution. We found that this combination greatly minimized internal reflection and refraction of the excitation and emission light.

The specimen holders have been chosen to match to the specimen's dimensions. Available are four different sizes of micro capillaries with various diameters (table 3.5.1).

mark(s) at μ l	Color-Code	inner \varnothing [mm]	Art.-No.
1/2/3/4/5*	white	0.29	7087 07
20	black	0.58	7087 18
50 + 100	blue	1.19	7087 45
100	blue	1.19	7087 44
200	red	1.6	7087 57

Fig. 3.4.1: Micro capillary sizes from intraMARK™

In case smaller dimensions are needed, the 1-5 μ l capillaries can be resized to smaller diameters using a micro pipette puller (Model: PN-30, Narishige Co. LTD, *Tokyo/Japan*).

The data acquisition took place under use of a custom programmed software in the LabView™ environment, for controlling the camera, the

stepper motor and the laser shutter, using a 3.6 GHz PC with 2GB RAM. The shutter was controlled so that sample illumination took only place during image acquisition in order to minimize fluorescence bleaching and reducing artifacts during the reconstruction procedure [21]. The reconstruction was based on a filtered back projection algorithm using a Hamming filter [56], by using the reconstructed variance to accurately find the center of rotation, as shown in Ref. [21]. Data acquisition consisted on 500 projections covering 360°, resulting in angle steps of 0.72°. Data sets were recorded for three channels with their corresponding background: fluorescence, excitation and white light illumination. The latter illumination mode offers anatomical information to improve visualization of the fluorescence data. In all cases, light was collected in the transmission mode (see Fig. 1). For low signal acquisition a 2x2 binning was applied to the CCD to reduce acquisition time and bleaching effects, resulting also in faster data reconstruction.

3.5 ABSORPTION COEFFICIENT

To estimate the capability of the OPT device to acquire data from within the body of a highly opaque sample, the mean absorption coefficient of *Drosophila melanogaster* has been defined experimentally. This was done by deep freezing some thousand adult wild type *Drosophila* in liquid Nitrogen. After evaporation of the Nitrogen, the deep frozen samples were grounded in a mortar generating a homogenous powder. This powder was quickly filled into a 2mm glass cuvette and the absorbance was measured in a spectrum analyzer. The results of the absorption coefficient in the wavelength range from 400nm to 850nm are presented in figure 3.5.1. The absorption coefficient of 5cm⁻¹ comprises, that for a sample thickness of 2mm it should be possible to detect approximately 35% of the incident light (compare fig. 2.1.2).

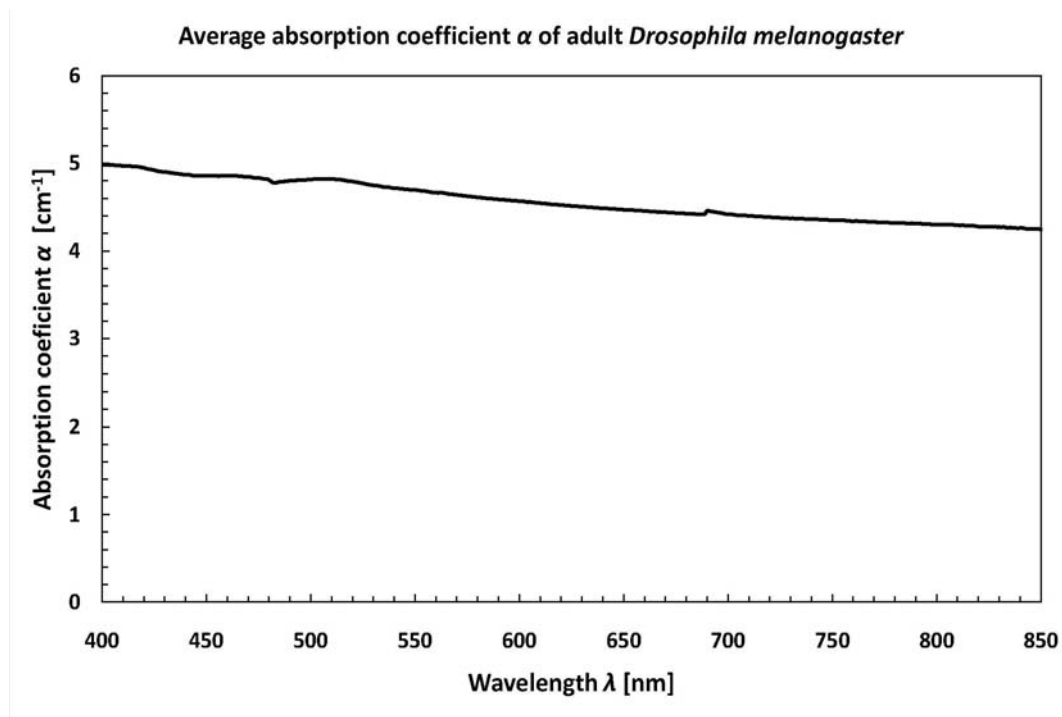


Fig. 3.5.1: Average absorption coefficient of grounded *D. melanogaster* samples. To date, there is no publication whatsoever of the absorption coefficient of *D. melanogaster* nor of Chitin in the visible wavelength region.

3.6 DATA RECONSTRUCTION

This subsection describes what features are implemented in the custom program of the OPT setup. It has been developed almost throughout the whole period of this thesis and it has shown that all characteristic implementations have made this software unique and helpful.

The data reconstruction was performed using a custom developed LabView™ program. Figures 3.6.1 – 3.6.4 exemplify screenshots of the GUI. First step after loading the data as a tif-stack (3.6.1 a) is to set the upper and lower threshold values corresponding to the dynamic range of the raw data (3.6.1 b). Visualization can be displayed and computed either with linear or logarithmic scale (3.6.1 d). In case of existing and loaded background data (3.6.1 c) (each background projection corresponds to an equivalent raw data

projection) it could automatically be subtracted from the raw data to minimize artifacts in the reconstruction.

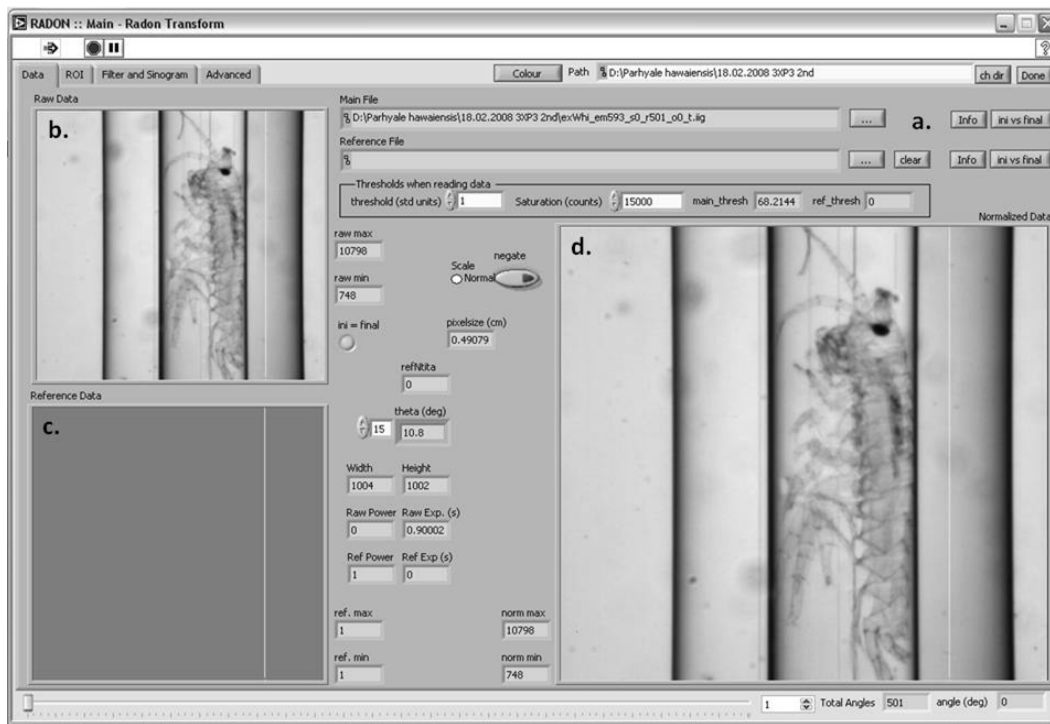


Fig. 3.6.1: Initial window of the general user interface (GUI), a) loading data, b) raw data, c) background data, d) thresholded and scaled data.

Another feature (fig. 3.6.2) is the verification of the initial projection (3.6.2 a) versus the final projection (3.6.2 b). This denotes a potential movement of the probe (3.6.2 c). The error can be displayed as the difference of the absolute values of the initial divided by the final projection (3.6.3 a), the ratio of the initial divided by the final projection (3.6.3 b) the inverse ratio corresponding to b) (3.6.3 c) and the normalized error of the initial and final projection in percent (3.6.3 d). Additionally to the tif-stack, the acquired data contains a header file comprising all settings of the experiment performed, e.g. acquisition time, gain settings, chip size, binning factor, excitation power, excitation wavelength, aperture size, sample information, employed excitation and fluorescence filters and fiducials. Apart from the camera settings, all further information has to be set manually.

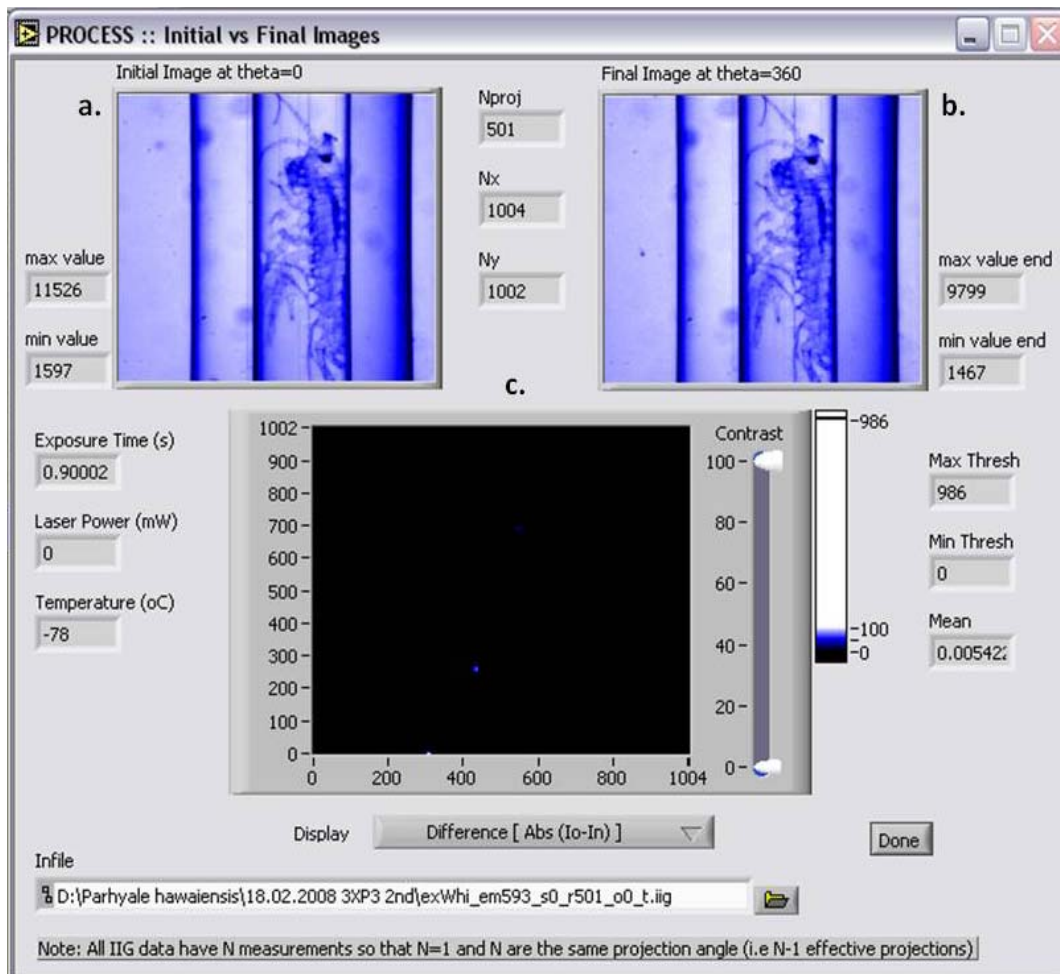


Fig. 3.6.2: Verification of the initial projection a) versus the final projection b). The error is displayed in the lower window c).

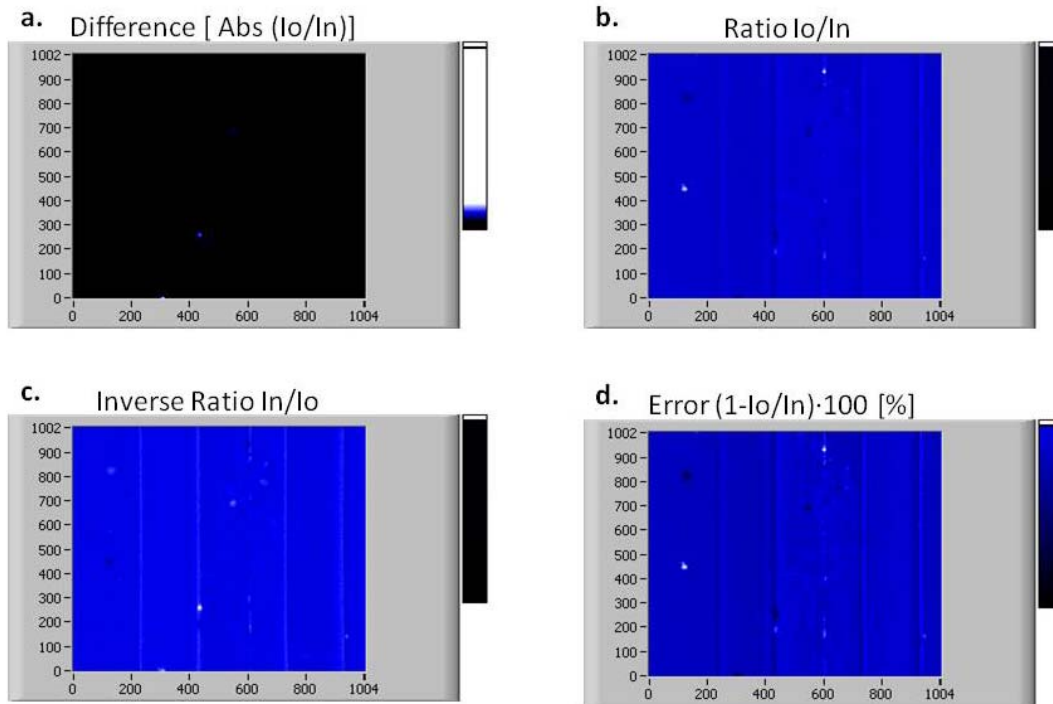


Fig. 3.6.3: Display of a) the difference of the absolute values of the initial divided by the final projection, b) the ratio of the initial divided by the final projection, c) the inverse ratio corresponding to b) and d) the normalized error of the initial and final projection in percent.

For reducing the reconstructed data size and minimize computational time, the next step is to define the region of interest (fig. 3.6.4 a) red lines and green lines) which is displayed and fine adjusted in brightness in b). The center of rotation (dashed white line) is roughly defined by scrolling through the projections and set the red and green x-cursors to the minimum and maximum positions of the probe's edges (as displayed in depiction 3.6.4 a)). The COR can be found within these positions. The fine tuning of the initial thresholds can be activated and applied by using the threshold bar and activation button (fig. 3.6.4 d).

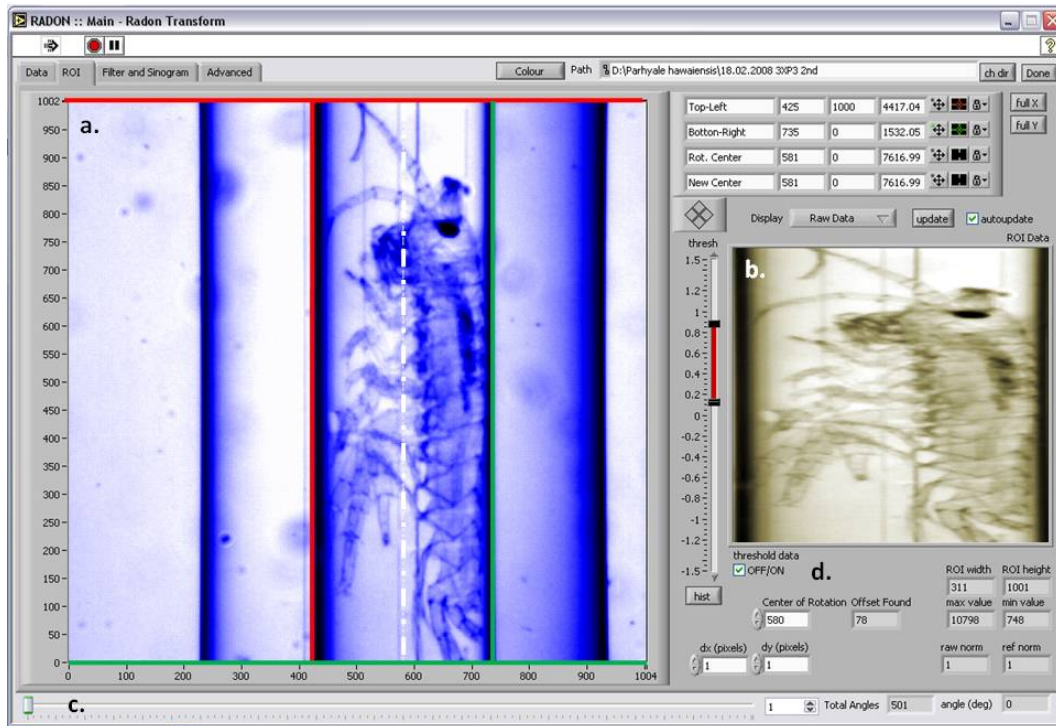


Fig. 3.6.4: a) definition of the ROI from the raw data and b) display of the ROI, c) projection scroll bar and d) fine tuning of the initial threshold values.

The next step is to find the correct center of rotation and frequency filter for the back projection. Fig. 3.6.5 represents the GUI of the settings of the radon transformation. Depiction 3.6.5 a) displays the ROI achieved in fig. 3.6.4 b)

To acquire a test slice of the raw data, a cursor can be set to the area of interest (yellow line in depiction 3.6.5 a). In the filter window (3.6.5 c) one chooses the desired radon filter for the filtered back projection. The sinogram of the area of interest defined in 3.6.5 a), is displayed in 3.6.5 b) and 3.6.5 d), while here, one now sets the initial (yellow vertical line) and final (green vertical line) position for the range settings required to calculate the variance for the correct COR (3.6.5 e). Inset 3.6.5 f) shows the result of the progress from the calculation in means of displaying the reconstructed slice in dependence of the COR.

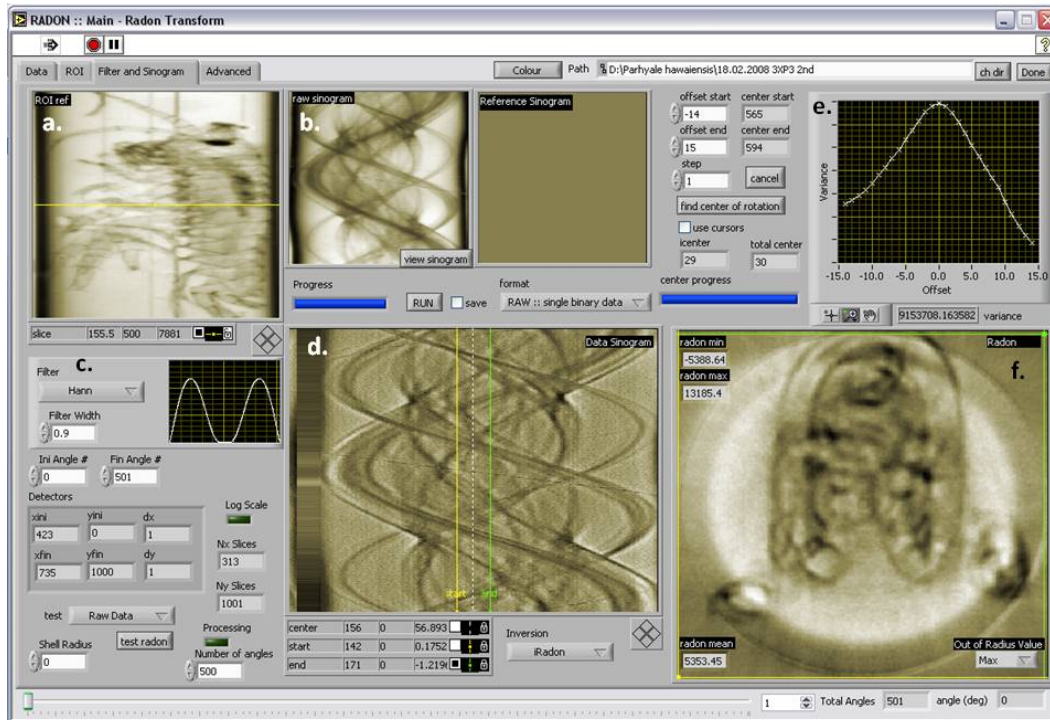


Fig. 3.6.5: GUI for radon transformation settings, a) acquired ROI from fig. 3.6.4 b), b) sinogram of depicted area of interest in a). Inset c.), filter window, d), initial (yellow vertical line) and final (green vertical line) position for range settings required to calculate the variance for the correct center of rotation (C.O.R.), e) calculation of the variance for calculating the C.O.R. (further described in fig. 3.6.6), f) result of progress from the calculation of the C.O.R.

The acquired data files of the reconstruction are stored as 32 bit raw data. Visualization can be performed using commercial available volumetric rendering software supporting large data sets. In the case of the reconstructed data shown in this thesis, volumetric data has been compressed from 32 bit real to 8 bit data sets.

A major but also easy to correct source of artifacts is the incorrectly defined center of rotation from sinograms which depend on the offset error. A severe (20 pixel offset) and minor (10 pixel offset) error is shown in figures 3.6.6 a) and 3.6.6 b). If the position of the rotational axis is not well known prior to data acquisition, it must be determined post-acquisition in order to minimize this artifact. The method used here is to predetermine the center of

rotation in the raw data by manually examining the projections. The correct center of rotation (C.O.R.) is found by defining a small area of +/- 20 pixels around the initial position in the sinogram and reconstruct this sinogram many times shifting the rotation center (in this case 41 times) to identify the correct position of the C.O.R.. Despite to the time consuming procedure, this step is necessary to avoid reconstruction artifacts as depicted in figure 3.6.6 a) and b). The reconstruction of a sinogram with a misaligned rotational axis can be considered to be a convolution of the correctly reconstructed image and an incorrect reconstructed point spread function of the system. This falsely reconstructed point spread function yields a circular shape and thus leads to artifacts as shown in figure 3.6.6 a) and b). The position of the rotational axis can then be determined by reconstructing a series of images with differently assumed positions of the rotational axis, and calculating the variance of each reconstruction.

If the center of rotation is not defined correctly, the projections do not overlap in the same point but around the C.O.R. thus resulting in a fuzzy image as shown in insets 3.6.6 a) and b). The further the offset from the C.O.R. is, the blurrier the image gets.

The reconstructed image that has the maximum variance is closest to the ideal reconstruction, as it is the least blurred. A similar 'autofocus' algorithm using the variance of the image has been previously used in standard microscopy [73]. We implemented this method and found it to be effective for identifying the centre of rotation to an accuracy of one pixel. The variance curve in figure 3.6.6 d) demonstrates the approach to the true location of the rotational axis. A reconstruction with the correct location of the rotational axis is shown in figure 3.6.6 c). This correction must precede this step as that artifact's presence can lead to erroneous results.

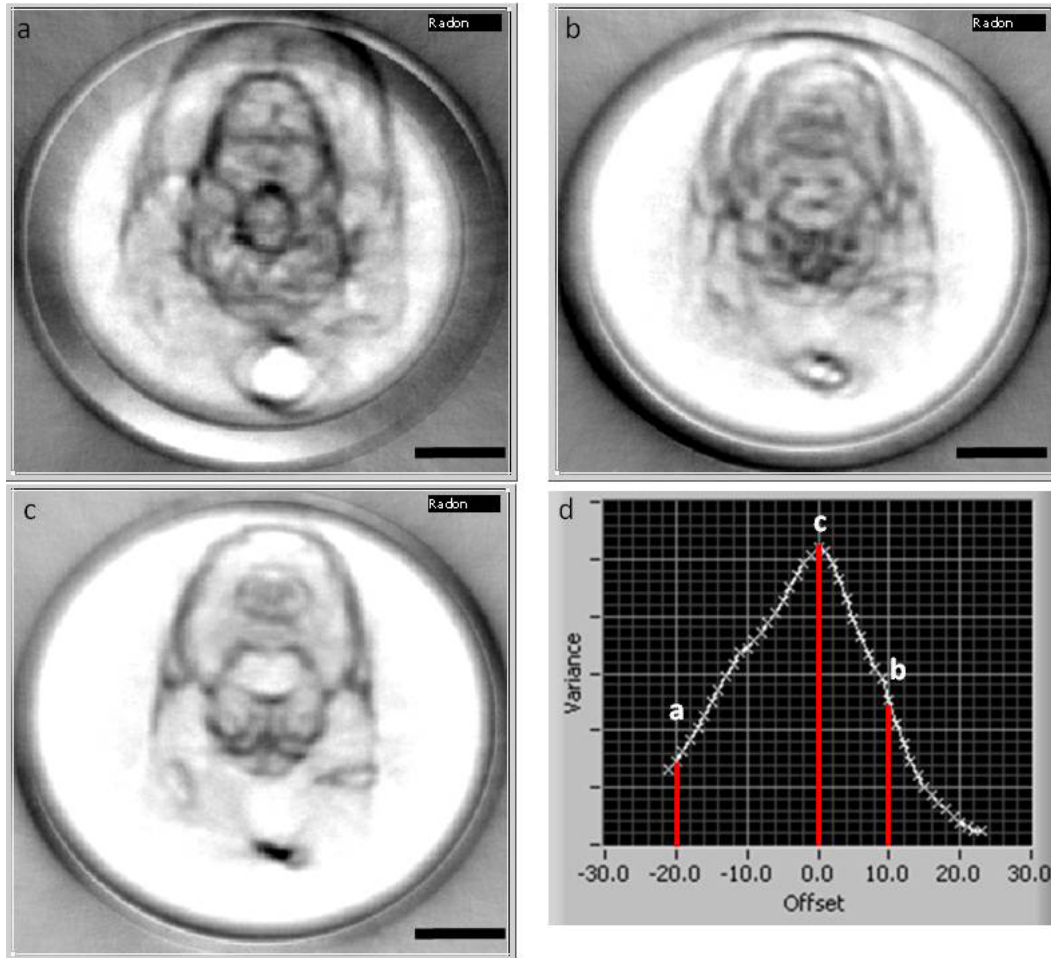


Fig. 3.6.6: Severe (a) or slight (b) artifacts during reconstruction arise from an incorrectly identified position of the rotational axis position, as demonstrated in these reconstructions in the exoskeleton of *Parhyale hawaiiensis*. If the center of rotation is not defined correctly, the projections do not overlap in the same point but around the C.O.R. thus resulting in a fuzzy image as shown in insets a) and b). The further the offset from the C.O.R. is, the blurrier the image gets. The reconstruction with the correctly identified rotational axis position is shown in c). The variance of a series of test reconstructions d) is a maximum at the true position of the rotational axis (red lines mark the offset of the reconstructions a, b and c). The scale bars represent 0.25 mm.

4 RESULTS AND DISCUSSION

4.1 DROSOPHILA MELANOGASTER

The *Drosophila melanogaster* samples were kindly provided by Prof. Charalampos Savakis and Dr. Athanasios Metaxakis from the Institute of Molecular Biology and Biotechnology at FORTH/GREECE. *Drosophila melanogaster* [74] is one of the world's most studied organisms belonging to the family of *Drosophilidae* together with more than 700 other species. The advantage of *Drosophila* is the ease and cost-effective breeding of an object of study with a bioavailability due to a short generation cycle of 9-14 days and an offspring of up to 400 individuals.

Ever since, lots of geneticists have studied this model organism and investigated numerous cognizance of genes and chromosomes in *Drosophila*'s genome. It was found that more than 70% of these genes have analogues in the human genome. This may reveal mechanisms responsible for a majority of human neurodegenerative disorders.

To date, most imaging techniques have been applied only to optically cleared and fixed *Drosophila* samples [54, 75]. OPT can help researchers to visualize the response of changes in the organism due to alterations in the normal activity of a specific gene without the risk of damaging tissue through dissection. However the absorption properties of the exoskeleton prevent the observer to gather information from inside the organism with standard microscope systems. In the past this lead researchers to dissect the fly which first is an arduously process, and second leads to the destruction of the specimen. Bleaching or better optical clearing of the exoskeleton has become a widely used method but contrarily is a vast intervention with the specimen's metabolism. The major objective here was to image complex organisms intact in the absence of hazardous clearing agents. One can easily observe the

alteration of *D. melanogaster's* opacity from the images of different developmental stages in life cycle shown in figure 4.1.1. As soon as it develops to the prepupal stage, it changes its opacity.

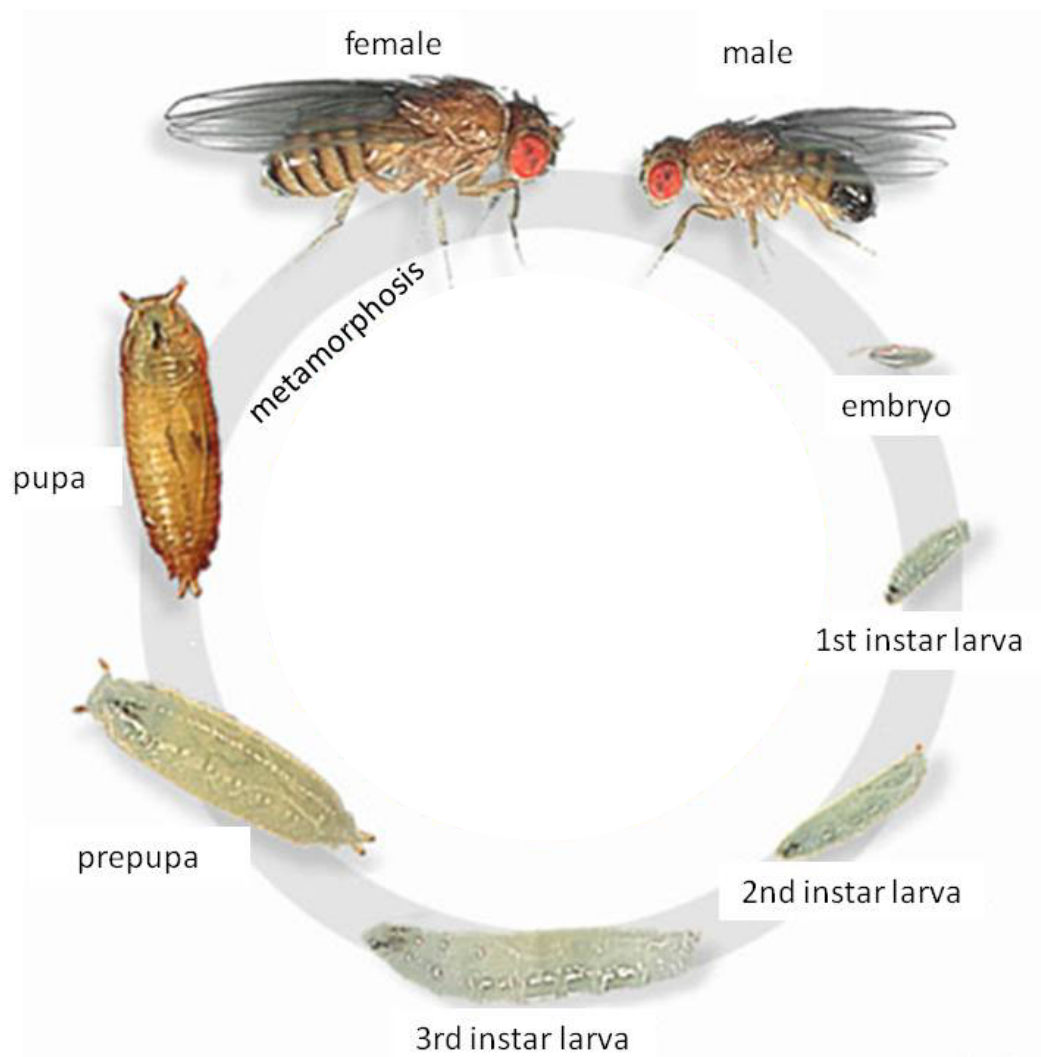


Fig. 4.1.1: Lifecycle of *Drosophila melanogaster*. Note that the first developmental stage of 3 hours starts from oviposition (source: <http://www.anatomy.unimelb.edu.au>).

The following images present raw and reconstructed images of *D. melanogaster* from the 3rd instar larval stage and the pupal stage in the absence of optical clearing agents.

Figure 4.1.2 depicts the acquired raw data with the OPT system using white light illumination, a) lateral, b) anterior view of a *Drosophila* larva in the 3rd instar larval stage.

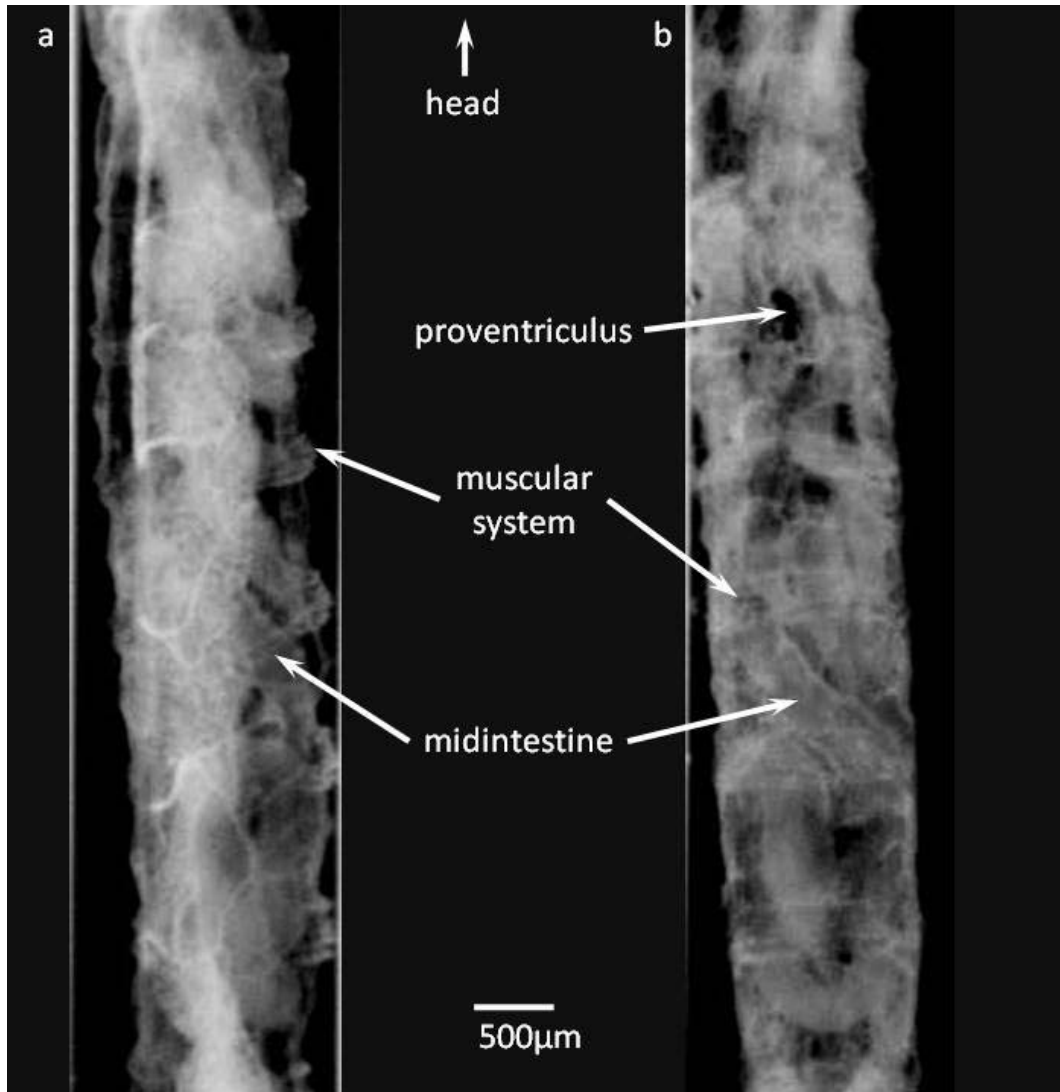


Fig. 4.1.2: White light raw images acquired with OPT, a) lateral, b) anterior view of a *Drosophila* larva in the 3rd instar larval stage.

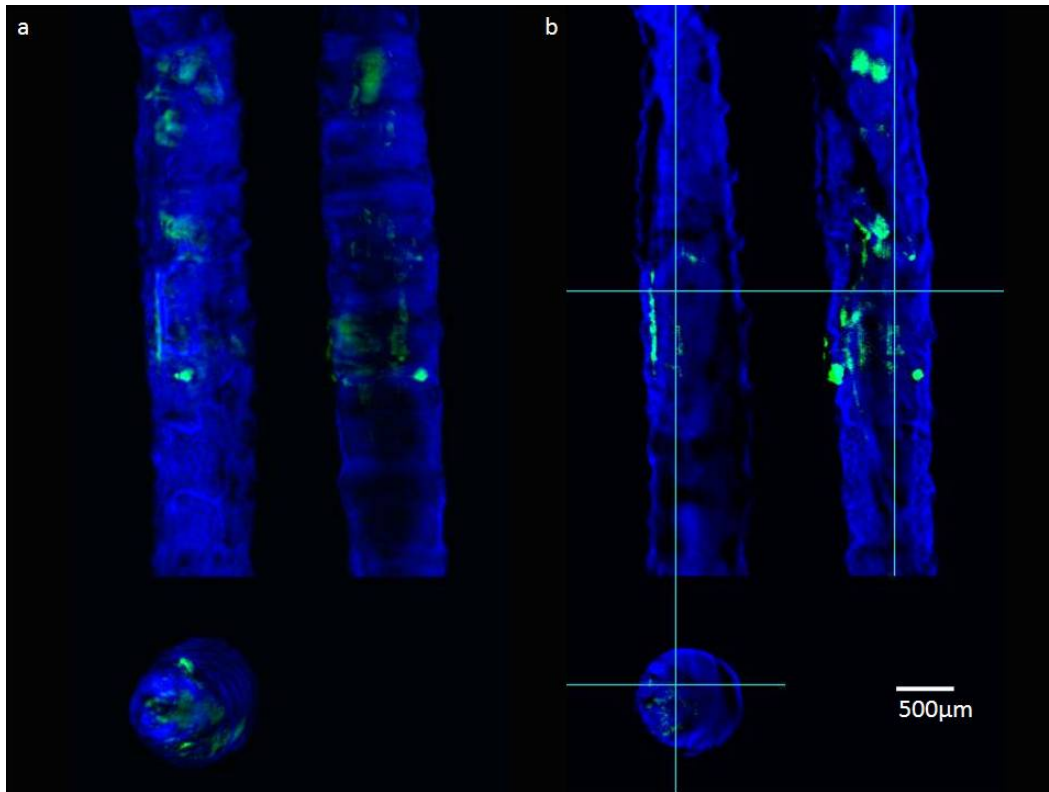


Fig. 4.1.3: Overlaid reconstruction of the white light (blue) and fluorescence (green) data taken *in vivo* from a day 5 state *Drosophila melanogaster* larva. GFP expression is controlled by MExT3e promoter, a) 3D overlay, b) internal sections longitudinal and transversal through the specimen. The larva shows significant GFP expression in the brain but also in the guts.

In-vivo results from an early stage (4-5th day) pupa of the *Drosophila melanogaster* enhancer trap line GR2x are shown in figure 4.1.4. The Gal4 / UAS system drives the expression of the GFP protein at the salivary glands during the larvae and early pupa stages [76]. The results show the reconstructed superposition of the GFP fluorescence in the salivary glands and the anatomy acquired with white light illumination (blue). The salivary glands are visible as green areas of fluorescence. In-vivo results from an early stage (4-5th day) pupa of the *Drosophila melanogaster* enhancer trap line GR2x. The Gal4 / UAS system drives the expression of the GFP protein at the salivary glands during the larvae and early pupa stages [76]. The results show the reconstructed

superposition of the GFP fluorescence in the salivary glands and the anatomy acquired with white light illumination (orange). The salivary glands are visible as green areas of fluorescence. Depictions a)-c) show the volumetric information of the whole specimen a) transversal, b) sagittal and c) coronal, while Figure d) represents the spatial view.

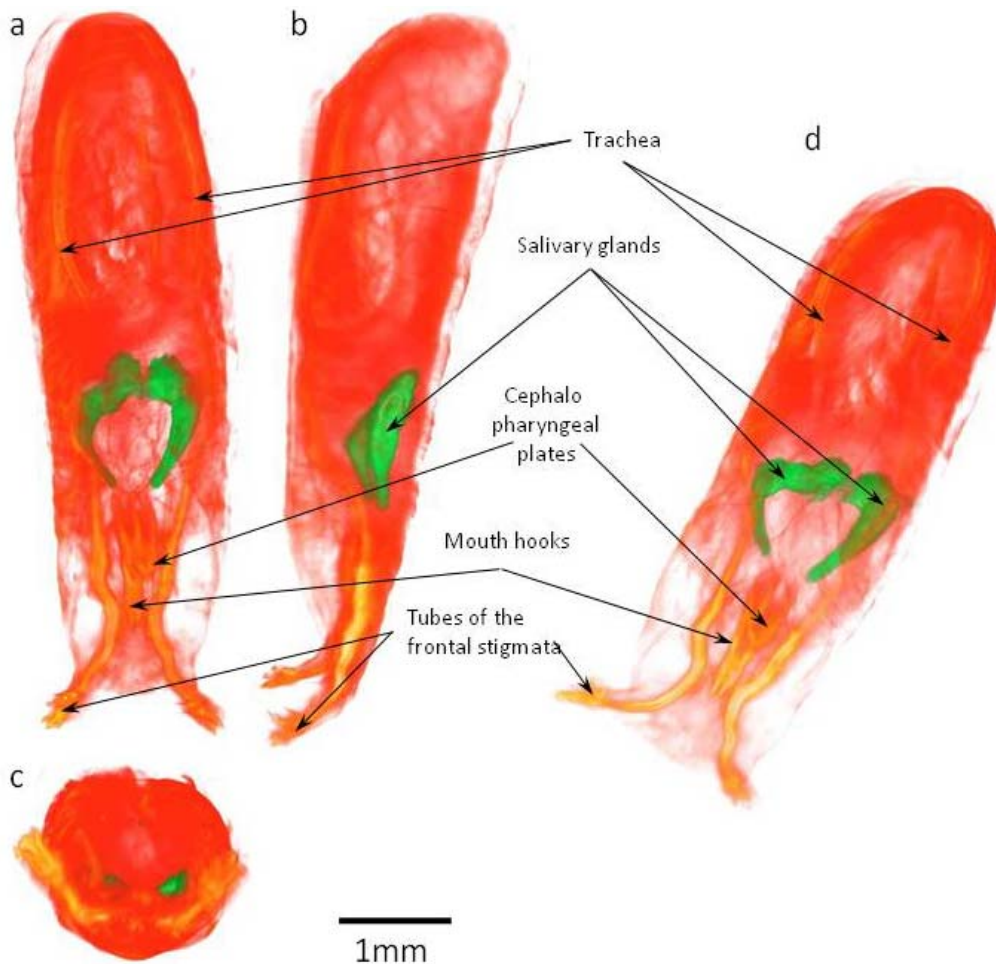


Fig. 4.1.4: In-vivo results from an early stage (4-5th day) pupa of the *Drosophila melanogaster* enhancer trap line GR2x [48]. The Gal4 / UAS system drives the expression of the GFP protein at the salivary glands during the larvae and early pupa stages [76]. The results show the reconstructed superposition of the GFP fluorescence in the salivary glands and the anatomy acquired with white light illumination (orange). The salivary glands are visible as green areas of fluorescence. Depictions a)-c) show the volumetric information of the whole specimen a) transversal, b) sagittal and c) coronal, while Figure d) represents the spatial view.

4.2 CAENORHABDITIS ELEGANS

The samples for the experiments with *Caenorhabditis elegans* were kindly provided by Matthias Rieckher who is under supervision of Prof. Nektarios Tavernarakis also at the IMBB facilities at FORTH/GREECE. *C. elegans* is a quite small (1mm in length and approximately 60 μ m in diameter) soil-found free-living nematode which can be easily reared on an *Escherichia Coli* diet under laboratory conditions. Its life cycle includes a period of embryonic development in the eggshell, four larval stages (L1-L4) and adulthood. With its fully discovered cellular system of 959 cells in the adult state [77, 78], with 302 complete determined neuronal cells, the knowledge of its full wiring diagram [79] and a possible life cycle of 2.5 days at 25°C, *C. elegans* can be easily propagated for use in genetic studies, since its amenability of genetic crosses and production of large number of progeny per adult. Its transparency makes it also quite suitable for any transillumination microscopic systems. The anatomical description of the whole animal has been completed at the electron microscopy level and its complete cell lineage, which is invariant between animals, has been established [77-79].

The preparation of the *C. elegans* samples was performed as follows: initial step is to shape the micro capillaries (1-5 μ l), thus the capillaries had to be cleaned using an ethanol imbued tissue to remove dirt and fuzzes. Then, the capillary was placed in a capillary puller (PN-30, Narishige Co. LTD, Tokyo/Japan) and resized to smaller diameters (80 – 100 μ m ID). A number of samples of desired developmental stage were picked and observed under a fluorescence microscope (Leica MZ-FLII, Leica Microsystems, Wetzlar/Germany) to confirm the required fluorescence pattern. Anesthetization was introduced by 10mM NaN₃ solution or 10mM Levamisole with an incubation time of 5 min. Afterwards the sample was transferred into a drop of Halocarbon oil on a cover slide, where the rest of the NaN₃ solution was completely removed from the worm in order to reduce

refractive index mismatch. It was then soaked into the capillary tip (pharynx ahead) so that it ended up approximately 0.5 cm away from the very tip. The capillary was cleaned again on the outside as described above and sealed with a tiny drop of quick glue, so that no index matching fluid could penetrate the capillary which would cause the destruction of the sample. The sample is now readily prepared and it should be immediately proceeded with recording.

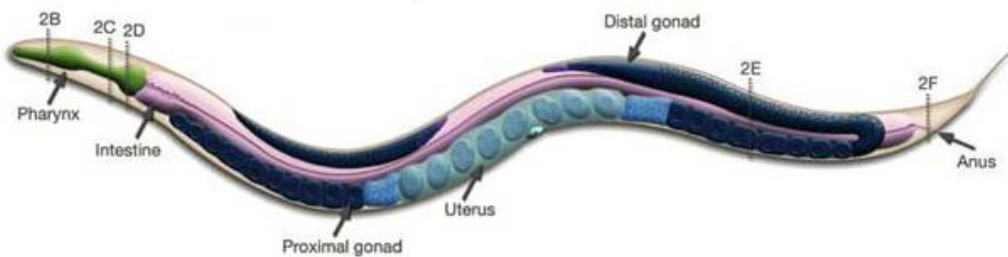


Fig. 4.2.1: Schematic presentation of *C. elegans*' anatomy (source: <http://www.wormatlas.org>)

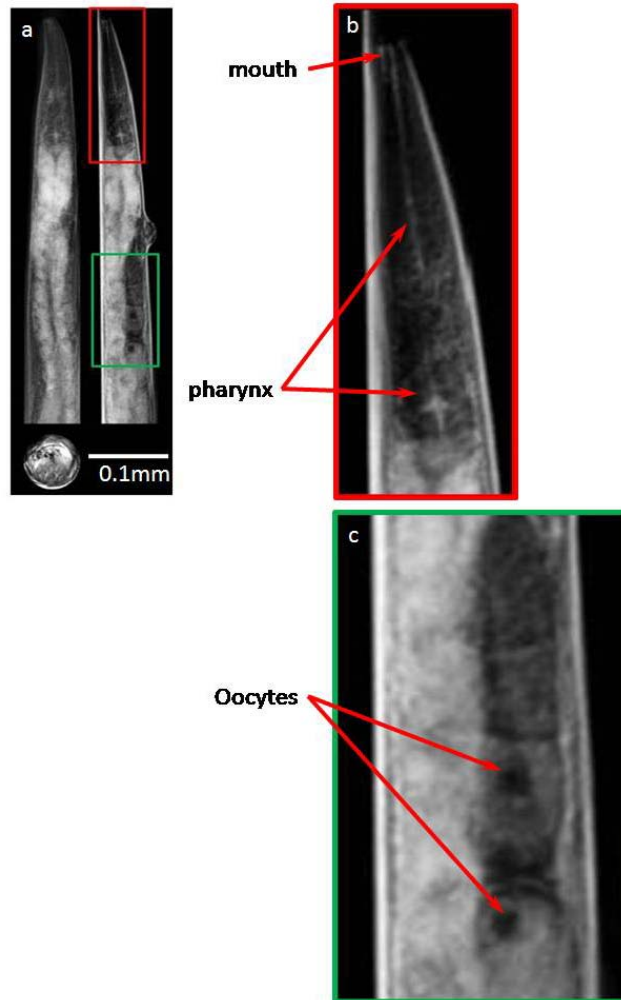
Imaging organisms in the size of *Caenorhabditis elegans* eases the data acquisition dramatically. Acquisition times range from 10ms (anatomical information received with application of white light illumination) to 50 ms (signal from GFP expression) respectively. This enables achievement of a complete data set of 500 projections within minutes.

The low acquisition time can be derived from the low opacity of the sample and the fact, that light undergoes almost no scattering events since the size of a *C. elegans* is below the scattering mean free path length of a photon.

Figure 4.2.2 presents the 3D anatomical information of an adult *C. elegans*. The reconstructed data is acquired with white light illumination from *C. elegans*, a) 3D reconstruction transversal (left), sagittal (right) and coronal (lower left), depiction b) shows the mouth and the pharynx, whole inset c) the oocytes are clearly visible. Data is based on white light images of the anterior part of the nematode (recorded through 10x lens) and can be sectioned *in*

in silico and reveals anatomical features (indicated by arrows). Insets b) and c) are digitally magnified.

Fig. 4.2.2: Reconstructed data acquired with white light illumination from *C. elegans*, a) 3D reconstruction transversal (left), sagittal (right) and coronal (lower left), depiction b) shows the mouth and the pharynx, whole inset c) the oocytes are clearly visible. Data is based on white light images of the anterior part of the nematode (recorded through 10x lens) and can be sectioned *in silico* and reveals anatomical features (indicated by arrows). Insets b) and c) are digitally magnified.



A major goal in applications for OPT microscopy is the 3D visualization of fluorescent expression patterns. Reconstructed white light and fluorescent image data were merged and *in silico* sectioning was performed to reveal the localization of expression. To demonstrate the functionality of the technique in these terms, worms stably expressing GFP under the control of the *unc-8* promoter were reconstructed and the expression pattern was compared to previously published data. The *unc-8* gene is expressed in neurons localized in the nerve ring at the pharynx and in motor neurons along the body [80].

Figure 4.2.3 exhibits the reconstruction of the same sample as in 4.2.2. Additionally it shows the 3D reconstructed GFP expression under control of the *unc-8* promoter in the neuronal system and the superposition of the anatomical and fluorescence data.

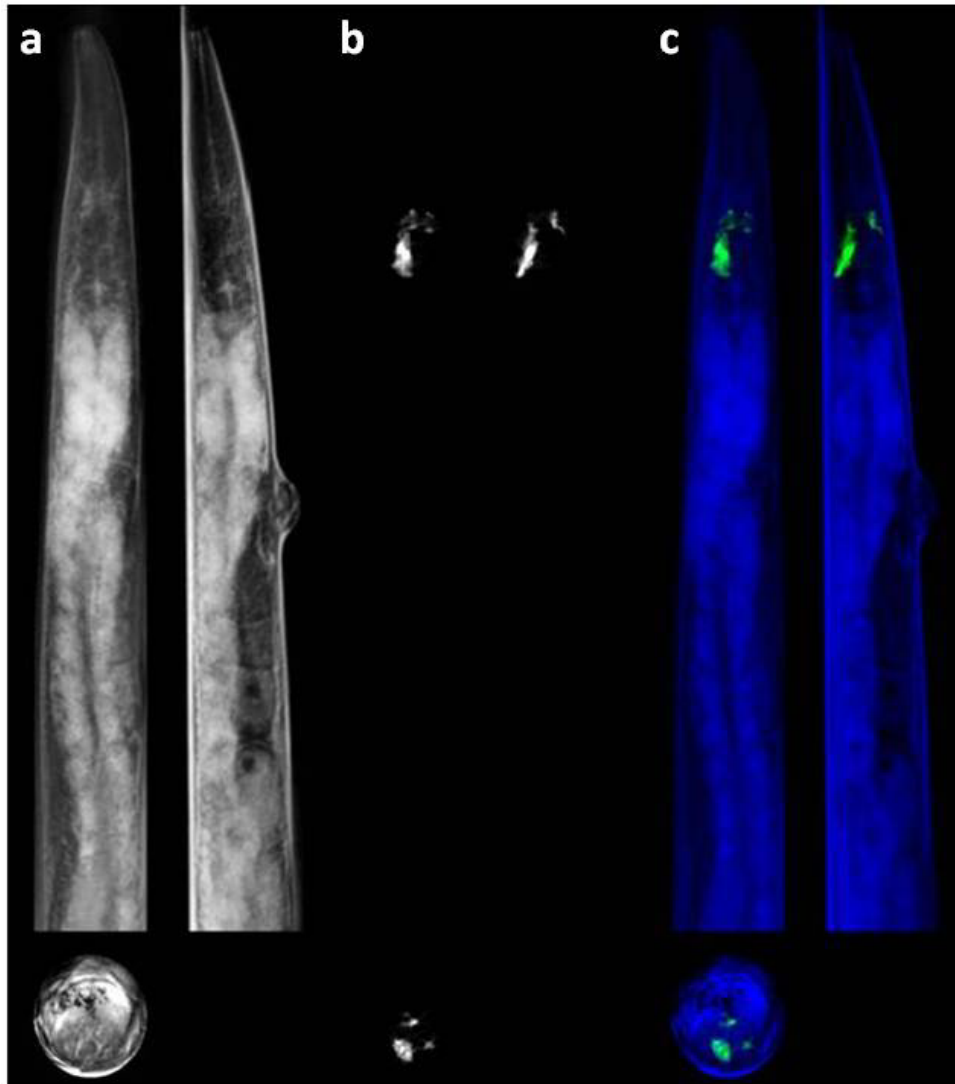


Fig. 4.2.3: 3D reconstruction of *Caenorhabditis elegans*, a) reconstruction from white light illumination transversal (left), sagittal (right) and coronal (lower left), depiction b) GFP fluorescence in the neuronal network, c) superimposed reconstruction of anatomical (blue) and GFP fluorescence data (green). The figure shows the expression of GFP under the control of the *unc-8* promoter with a strong signal in the pharynx region.

To show the ability of OPT to measure signals from two different fluorescent dyes, animals were recorded the stably co-express GFP and dsRed under the control of different promoters: the GFP labelled *daf-6* promoter is expressed in the amphid sheath glia, the phasmid sensory organ sheath and socket cells, cells of the excretory system and the vulva [81]. The fluorescent protein dsRed was put under the control of the *pqn-21* promoter which expresses in almost all somatic cells. The expression of those genes has been found to co-localize in some cells in the pharynx but has not been detected here. The results are illustrated in figure 4.2.4. Depiction 4.2.4 a) represents the *in silico* slices through the specimen of the absorption tomogram. The expression pattern of GFP and dsRed are shown in figure 4.2.4 c) - d) respectively.

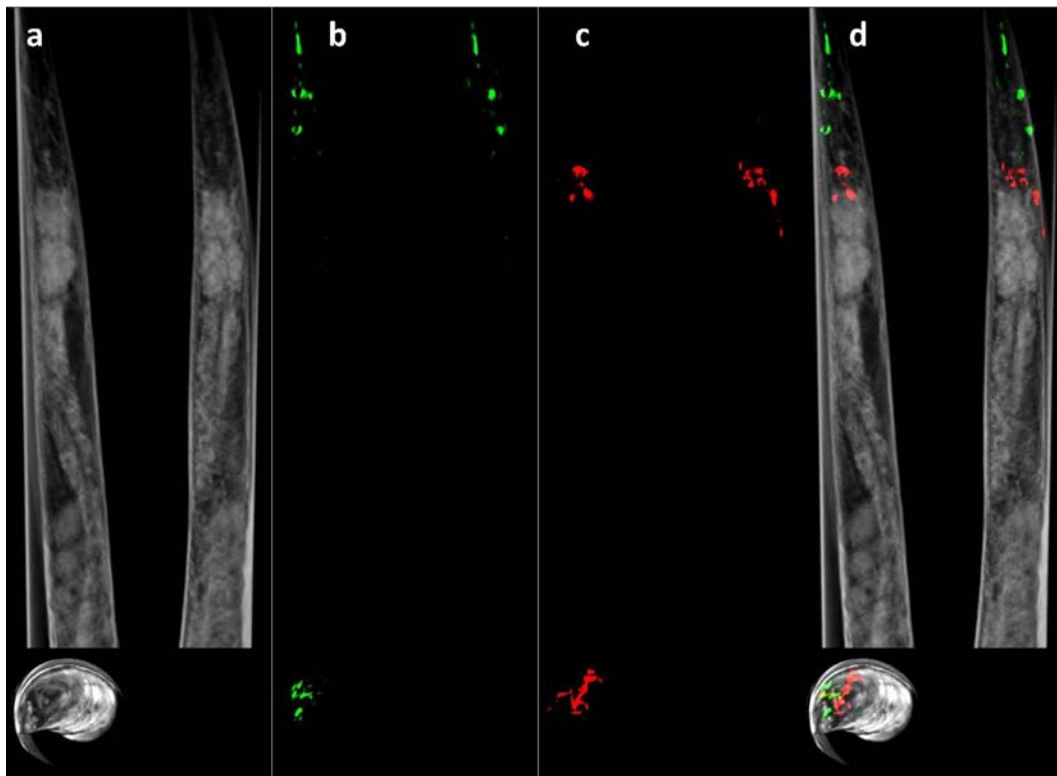


Fig. 4.2.4: *In silico* slice through *C. elegans*, a) White light image, b) GFP signal, c) dsRed signal and d) merge of 3D reconstructed data. GFP is expressed under the control of the *daf-6* promoter and dsRed under the control of *pqn-21* promoter.

The comparison of the reconstructed GFP fluorescence pattern achieved with OPT and Fluorescence Microscopy is illustrated in figure 4.2.5 respectively.

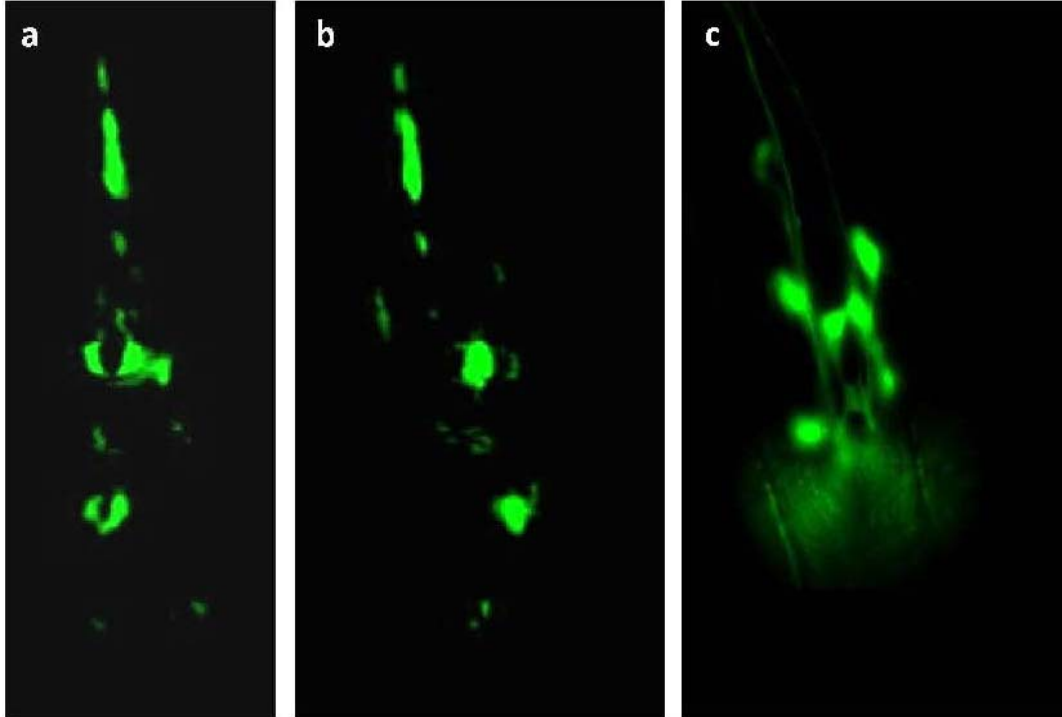


Fig. 4.2.5: 3D reconstruction of GFP expression under control of *daf-6* promoter, a) and b) transversal and sagittal view, c) 2D fluorescence microscopy of GFP expression under control of *daf-6* promoter in *C. elegans*.

4.3 PARHYALE HAWAIENSIS

Another model organism for studies in developmental biology has been found in the amphipod crustacean *Parhyale hawaiiensis*. The probes here were kindly provided by Dr. Michalis Averof and Alexandros Kiupakis also from the IMBB facilities at FORTH. Since its advance as an attractive organism for evolutionary developmental comparisons, there have been considerable efforts in isolating developmental genes and the studies of their expression patterns in *P. hawaiiensis*. The scope of using this model organism is the limitation by the inability to assess gene functions directly in non-model species, thus debarring

the characterization of new gene functions in non-model species. The objective is to appropriate comparative examinations of prospect genes from known and well established model organisms. One approach in developing techniques to overcome these limitations has been reported by Pavlopoulos and Averof [82-84] by the application of Minos transposable element for genetic transformation. The advantages of using *P. hawaiiensis* as a comparative model organism for genetic-developmental research are its ease of large numbered culturing in the laboratory and its relatively rapid lifecycle, which is approximately 2 month, and therewith its all stage accessible transparent embryos, which offer possibilities for genetic and developmental manipulations [85, 86]. The developmental stages of *P. hawaiiensis* are exhibited in figure 3.9.1 [87].

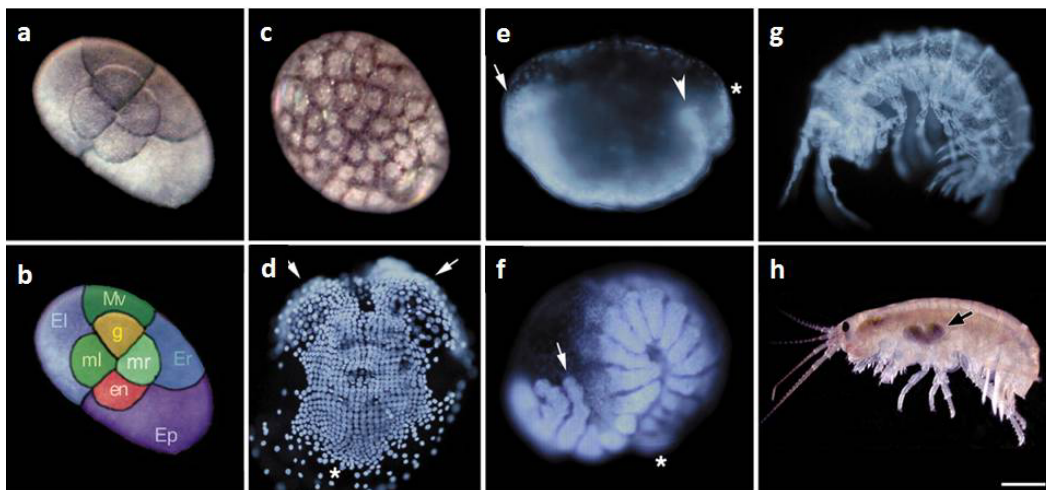


Fig. 4.3.1: Overview of *Parhyale* development. a) Living eight-cell embryo. Dorsal view, anterior upwards. b) The nomenclature of the macromeres and micromeres projected on the egg of a). c) Dorsal view of a living egg at 12 hours, d)-g) DAPI stained embryos. d) The early germband at day 3. Ventral view, anterior upwards. The first landmarks of the germ band are the head lobes (arrows). e)-h) Lateral views, anterior leftwards. e) Germband extension at day 4. f) The extended germband at day 5. g) The embryo at day 9. By this time, the adult morphology has been established as *Parhyale* is a direct developer (compare with h). h) A living gravid adult female carrying eggs in her ventral brood pouch (arrow). Scale bar: 100 μm in A-G; 2 mm in h) (source: [87]).

Since *P. hawaiiensis* is a salt water organism, immobilization was precipitated using low concentration of clove oil as an additive in artificial salt water. After duration of 5 min, the test object was placed in halo carbon oil to obtain a proper refractive index match to the capillary. Thus, it can be assumed that the measurements with *P. hawaiiensis* were performed *ex vivo*. However, degradation of the anatomy has not been observed, neither during nor directly after the measurement.

Cultured *P. hawaiiensis* [84, 85, 88, 89] are the courtesy of M. Averof and A. Kioupakis at IMBB-FORTH. The sample shown in figure 4.3.2 presents the superposition of autofluorescence (greenish-blue) signal of the exoskeleton and dsRed fluorescence on the muscular system.

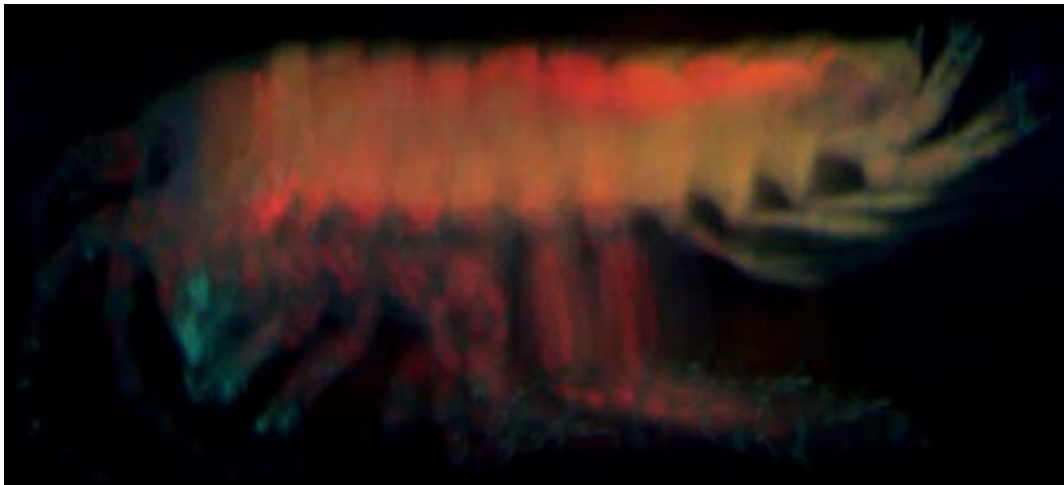


Fig. 4.3.2: 2D image acquired with a commercial fluorescence microscope. The exoskeleton shows autofluorescence (bluish-green) using a GFP excitation filter ($450 \pm 20\text{nm}$) while the muscular system is presented in red from the dsRed expression under control of 3XP3 promoter.

Note the single muscle strains in the legs. To that end, the only published volumetric data is that of the exoskeleton, which has been presented by Darrell et al. [89] and was achieved clearing the tissue in BABB and reconstructing the autofluorescence signal. The data presented in this section exhibits the first volumetric data reconstruction of the exoskeleton and the expression of dsRed in the muscular system as shown in figure 4.3.2 and

enlarged in 4.3.3 in the absence of optical clearing agents. Figure 4.3.4 represents the volumetric anatomical data of the exoskeleton using white light illumination, hence only data acquired due to tissue absorption.

Figure 4.3.3 exhibits the superimposed reconstructions of the exoskeleton (bluish-green) and the dsRed expression of the 3XP3 promoter in the muscular system of *Parhyale hawaiiensis*. Depictions a.-d.) represent the superimposed reconstruction while in depiction e.) the reduced opacity of the exoskeleton is shown for better visualization of the dsRed expression in the muscular system.

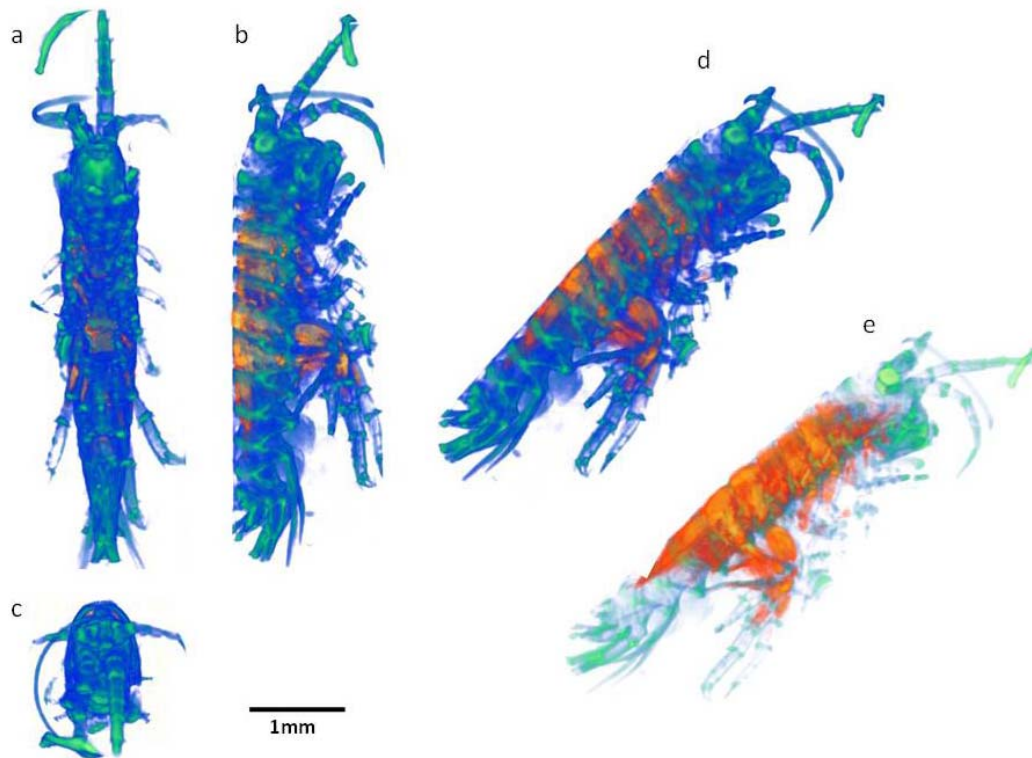


Fig. 4.3.3: a.-c-) frontal, sagittal and transversal view of the superimposed reconstruction of the exoskeleton (bluish-green) and dsRed expression from the 3XP3 promoter in the muscular system of a *Parhyale hawaiiensis*, d.) 3D spatial view, e.) same as d.) but with reduced opacity in the exoskeleton. The sample was kept in halo carbon oil to match the refractive index of the capillary.

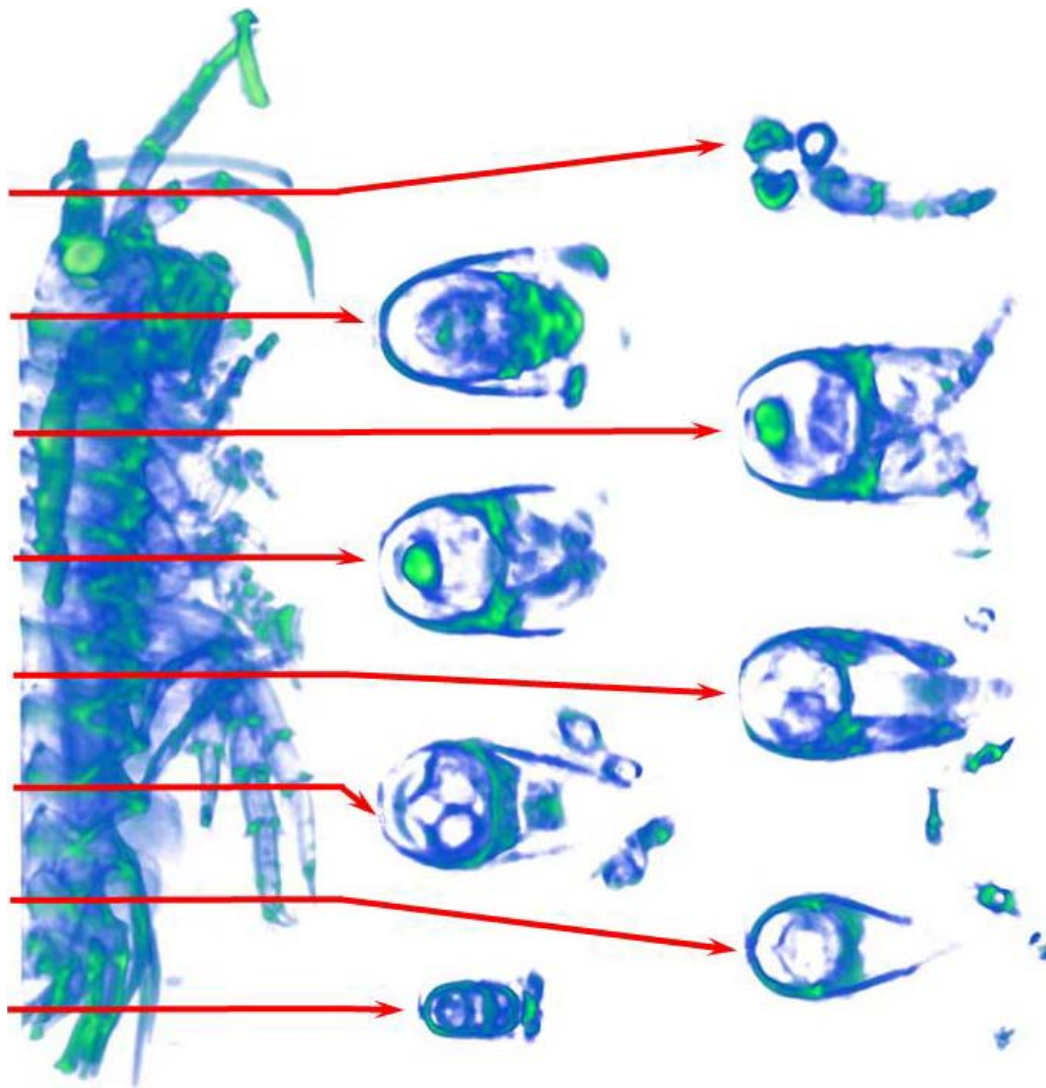


Fig. 4.3.4: 3D reconstruction of the exoskeleton of the *P. hawaiiensis* shown in figure 4.3.3. Red lines mark the transverse optical sections depicted on the right. Data acquired by white light illumination.

Figure 4.3.4 represents the reconstructed exoskeleton as presented in figure 4.3.3. The red lines mark the slices of interest as shown in the depictions on the right.

Data of the exoskeleton was acquired with white light illumination and represents the absorption of the chitin.

5 CONCLUSIONS AND FUTURE ASPECTS

5.1 CONCLUSION

To date, this is the first time OPT has been performed *in vivo* on living complex organisms. It has traditionally been assumed and practiced, that applying the Radon transform to mm sized objects requires the fixation and an optical clearing of the specimen. It is commonly believed, that imaging opaque samples will result in reduced resolution.

This thesis reports first time the capability of an OPT based setup not only in measuring fluorescence patterns in cleared *ex vivo* samples but also in opaque and low-scattering tissues, where scattering is negligible due to the mean free path length of scattered photons, thus enabling *in vivo* imaging in small specimens with tissue properties. Hence, this thesis presents the potential of OPT to image small biological model organisms during their development i.e. in the case of *D. melanogaster* throughout the different larvae and pupa stages.

It further represents high quality high resolution 3D reconstructions of the salivary glands and the brain of *Drosophila melanogaster* in the larva and the pupa state.

Apart from imaging *Drosophilidae*, the capability of the above described OPT setup was also established to image small specimens from adult *Caenorhabditis elegans* (approx. 1mm in length and 60-80 μ m in diameter) to larger and highly opaque samples such as *Parhyale hawaiensis* (3-4mm in length and approximately 1.2 – 2mm in diameter) respectively. This has been the first time that OPT was successfully applied to highly opaque specimens without changing their optical properties by clearing methods using organic solvents as i.e. BABB or MSBB.

OPT can be used to study morphology during the developmental stages delivering high ($< 5\mu\text{m}$) spatial resolution not only for cleared specimens but also living opaque organisms. With the addition of fluorescence imaging, OPT allows studies of fluorescence distribution *in vivo*, which could be used to image cell migration during the developmental stages of small specimens.

All results presented in this paper were produced by the filtered backprojection of 500 projections. It is well-known that reconstruction images of similar quality can be obtained from a smaller number of projections using other iterative reconstruction algorithms such as the Algebraic Reconstruction Technique [56] which offers the opportunity for a fuller model of light propagation. We are currently working towards this in order to greatly reduce the number of projections required for equivalent reconstructions, thereby reducing the total time required for the completion of an OPT imaging experiment. In principle, with very few projections and making use of more detection points (CCD cameras) or mirrors, it should be possible to obtain real-time 3D data acquisition of live samples.

Another planned improvement to the setup is a rapid filter changing mechanism that would allow multi-color imaging of the same specimen within the same experiment. Such an advance would allow the tracking of area-area interaction or even cell-cell interaction *in vivo* which could also be useful in cell migration studies.

5.2 FUTURE APPLICATIONS

During the previous two years, major progress has been achieved in the field of non-contact rotation using either optical rotators based on the principle of optical tweezers or other techniques adapted from micro fluidic systems and field cages, thus delivering the opportunity of keeping cells or small organisms in a complementary environment, thereby enabling the non-invasive

observation and collection of volumetric information. This enables the ability of reconstructing the development from the single cell to complex cell clusters.

Further research is directed towards the development of high resolution Optical Projection Tomography merging OPT with novel high resolution imaging systems, thus combining the advantages of systems and eliminating the disadvantages of one another.

Another goal in planned future work is to take *in vivo* fluorescence OPT one step further by facilitating quantitative fluorescence OPT reconstructions, first by accounting for absorption by dividing fluorescence images by their absorption counterparts and also by means of modified reconstruction algorithms that fully account for the physics of light propagation in emission OPT. Such quantitative reconstructions would allow the determination and comparisons of the amount of fluorescence in different regions of the same specimen.

Additional elaborations are pointed towards this quantification of fluorescent signals in reference to the position of the imaged fluorescence source relatively to the center of rotation. Recent publications [89-91] have shown great improvement in developing algorithms by accounting for the point source propagation of the fluorophore.

The first approach to quantify the emitted light of fluorescent probes in a sample is based on a weighted filtered backprojection algorithm which takes quantitative effects such as defocus and isotropic emission into account. In first simulations, this approach has shown excellent results.

ACKNOWLEDGEMENTS

This work has been supported by the E.U. Integrated Project "Molecular Imaging" LSHG-CT-2003-503259 and by Early Stage Training Marie Curie grant. I would like to thank Sascha Atrops for programming the visualization software for the reconstructed data. I am very happy to thank the research groups of developmental biology in the IMBB namely the group of Prof. Charalampos Savakis and especially Dr. Thanos Metaxakis who provided the *D. melanogaster* probes and the group of Prof. Nektarios Tavernarakis, where I would like to give special thanks to Matthias Rieckher, Giannis Voglis and Maria-Daphne Bazopoulou for providing the *C. elegans* samples and Matthias also for the really helpful discussions about the preparation of the probes and the amazing times in the lab we performed experiments. I would further like to thank Dr. Michalis Averof and Alexandros Kioupakis for the supply with *P. hawaiiensis* samples. I also have to thank Chrise Doxa and Aspasia A. Sterioti from the Hellenic Center of Marine Research (HCMR) for providing the *Ch. tritonis* samples. I would also like to mention the fruitful discussions with Dr. James Sharpe during the summer school of molecular imaging held in Kolympari/Crete.

Additionally I would like to acknowledge the useful discussions and times in the lab with Alex Darrell and Dr. Udo Birk who took over the device after my departure from Crete.

My very special thanks are directed towards Prof. Frank Grosveld who gave me the opportunity and the privilege to compose the here presented work under his supervision, and Prof. Claire Wyman, both from Medical Faculty of the Erasmus University Rotterdam. I would further like to thank Dr. Adriaan B. Houtsmuller and Dr. Niels J. Galjart for their advices and fruitful discussion. My very special thanks are directed towards Marike van Geest for her kindness and all the extraordinary help she provided throughout the years.

ACKNOWLEDGEMENTS

And what would I have been without the one person behind it, who made it all happen, always pulling the strings in the back, having an open ear at all times and who always had a hint in the back when I got stuck and encouraged me with invaluable suggestions ever since I came to Crete: Jorge, thank you so much! Thank you for all the guidance you gave at work and sometimes also in every day's life. The bad thing for me is that I'll never be able to return all this to you. Maybe someday I will be in the same position, having somebody to supervise and I can give him or her all the help that you gave to me.

What would an acknowledgement be without mentioning the people one spent more than five years together with, with whose I shared not only time in lab or in the office, but also in private, above and under water and with whose I had many valuable discussions: Giannis Zacharakis, Anikitos Garofalakis, Rosy Favicchio, Charalampos 'Charris' Gkikas, Georgia Fousteri, Clio Mamalaki, Constantinos Kalpouzios and last but not least the team of the workshop under supervision of Michalis Viskadourakis.

I would also like to mention the really nice weekends at the European Diving Center in Lygaria where I relaxed whenever my work allowed it. It has been a great time on this beautiful island. Even though I have spent almost 6 years there, I returned home almost as pale as I was the first time I went there.

Finally I would like to thank my family, which I'm deeply indebted to, who gave me an invaluable support throughout my studies and pushing me forward when it was needed.

Hannover, December 2009

Heiko Meyer

REFERENCES

1. Radon, J., *Über die Bestimmung von Funktionen durch ihre Integralwerte längs gewisser Mannigfaltigkeiten*. Ber. Verh. sächs. Akad. Wiss. Leipzig Math Phys., 1917. **69**: p. 262-277.
2. Radon, J., *On the determination of functions from their integral values along certain manifolds*. Ber. Verh. sächs. Akad. Wiss. Leipzig Math Phys., 1986. **69**: p. 262 - 277.
3. Sharpe, J., et al., *Optical projection tomography as a tool for 3D microscopy and gene expression studies*. Science, 2002. **296**(5567): p. 541-545.
4. Fauver, M., et al., *Three-dimensional imaging of single isolated cell nuclei using optical projection tomography*. Optics Express, 2005. **13**(11): p. 4210 - 4223.
5. Huang, D., et al., *Optical coherence tomography*. Science, 1991. **254**(5035): p. 1178-81.
6. Kikuchi, S., et al., *Three-dimensional computed tomography for optical microscopes*. Optics Communications, 1994. **107**: p. 432-444.
7. Barbour, R., et al., *MRI-guided optical tomography: Prospects and computation for a new imaging method*. IEEE Comp. Sci. & Eng., 1995. **2**(4): p. 63-77.
8. Kruger, R.A., et al., *Photoacoustic ultrasound (PAUS)- Reconstruction tomography*. Medical Physics, 1995. **22**(10): p. 1605-1609.
9. Haller, E.B., *Time-resolved transillumination and optical tomography*. J. Biomed. Opt, 1996. **1**: p. 7-17.
10. Arridge, S.R. and M. Schweiger, *Image reconstruction in optical tomography*. Philos Trans R Soc Lond B Biol Sci, 1997. **352**(1354): p. 717-26.
11. Cheng, X. and D.A. Boas, *Diffuse optical reflection tomography with continuous-wave illumination*. Optics Express, 1998. **3**(3): p. 118-123.
12. Arridge, S.R., *Optical tomography in medical imaging*. Inverse Problems, 1999. **15**(2): p. R41-R93.
13. Durduran, T., et al., *Algorithms for 3D localication and imaging using near-field diffraction tomography with diffuse light*. Optics Express, 1999. **4**: p. 247-262.
14. Ntziachristos, V., B. Chance, and A.G. Yodh, *Differential diffuse optical tomography*. Optics Express, 1999. **5**(10): p. 230-242.
15. Ntziachristos, V., *Concurrent diffuse optical tomography, spectroscopy and magnetic resonance of breast cancer.*, in *Bioengineering*. 2000, University of Pennsylvania: Philadelphia.

REFERENCES

16. Ntziachristos, V., et al., *Concurrent MRI and diffuse optical tomography of breast after indocyanine green enhancement*. Proc. Natl. Acad. Sci. U.S.A., 2000. **97**(6): p. 2767-72.
17. Boas, D., et al., *Imaging the Body with Diffuse Optical Tomography*. IEEE Signal Processing Magazine, 2001. **18**: p. 57-75.
18. Kerwin, J., et al., *3 dimensional modelling of early human brain development using optical projection tomography*. BMC Neuroscience, 2004.
19. Sharpe, J., *Optical Projection Tomography*. Annu. Rev. Biomed. Eng., 2004. **6**: p. 209 -228.
20. Sharpe, J., *Optical projection tomography as a new tool for studying embryo anatomy*. Journal of Anatomy, 2003. **202**: p. 175 - 181.
21. Walls, J.R., et al., *Correction of artefacts in optical projection tomography*. Phys. Med. Biol., 2005. **50**: p. 4645-4665.
22. Walls, J.R., et al., *Resolution improvement in emission optical projection tomography*. Physics in Medicine and Biology, 2007. **52**: p. 2775 - 2790.
23. Wang, Y. and R.K. Wang, *Optimization of image-forming optics for transmission optical projection tomography*. Applied Optics, 2007. **46**(27): p. 6815 - 6820.
24. Minsky, M., *Memoir on inventing the confocal microscope*. Scanning, 1988. **10**: p. 128-138.
25. Shaw, P.J., et al., *Tilted view reconstruction in optical microscopy: three dimensional reconstruction of Drosophila melanogaster embryo nuclei*. Biophys.J., 1989. **55**: p. 101-110.
26. Cogswell, C.J., K.G. Larkin, and H.U. Klemm, *Fluorescence microtomography: multi-angle image acquisition and 3D digital reconstruction*. Proc. SPIE, 1996. **2655**.
27. Kawata, S., *The optical computed tomography microscope*. Adv. Opt. Electron Microsc., 1994. **14**: p. 213-248.
28. Bradl, J., et al., *Resolution improvement in 3-D microscopy by object tilting*. Microsc. Anal., 1996b. **44**: p. 9-11.
29. Denk, W., J.H. Strickler, and W.W. Webb, *Two-photon laser scanning fluorescence microscopy*. Science, 1990. **248**(4951): p. 73-6.
30. Dodt, H.U., et al., *Ultramicroscopy: three-dimensional visualization of neuronal networks in the whole mouse brain*. Nat Methods, 2007. **4**(4): p. 331-6.
31. Lindek, S., J. Swoger, and E.H.K. Stelzer, *Single-lens theta microscopy: resolution, efficiency and working distance*. Journal of Modern Optics, 1999. **46**(5): p. 843-858.
32. Stelzer, E.H.K. and S. Lindek, *Fundamental reduction of the observation volume in far-field light microscopy by detection othogonal*

- to the illumination axis: confocal theta microscopy. *Optics Communications*, 1994. **111**: p. 536-547.
33. Stelzer, E.H.K., et al., *A new tool for the observation of embryos and other large specimens: confocal theta fluorescence microscopy*. *Journal of Microscopy*, 1995. **179**(1): p. 1-10.
 34. Engelbrecht, C.J., et al., *Three-dimensional laser microsurgery in light-sheet based microscopy (SPIM)*. *Opt Express*, 2007. **15**(10): p. 6420-30.
 35. Engelbrecht, C.J. and E.H. Stelzer, *Resolution enhancement in a light-sheet-based microscope (SPIM)*. *Opt Lett*, 2006. **31**(10): p. 1477-9.
 36. Abbott, A., *Cell culture: biology's new dimension*. *Nature*, 2003. **424**(6951): p. 870-2.
 37. Webb, D.J. and A.F. Horowitz, *New dimensions in cell migration*. *Nature Cell Biology*, 2003. **5**: p. 690-692.
 38. Streicher, J., et al., *Computer-based three-dimensional visualization of developmental gene expression*. *Nature Genetics*, 2000. **25**: p. 147 - 152.
 39. Potter, S.M., et al., *Multi-site two-photon imaging of neurons on multi-electrode arrays*. *Proceedings SPIE*, 2001. **4262**: p. 104 - 110.
 40. Krstajic, N. and S.J. Doran, *Focusing optics of a parallel beam CCD optical tomography apparatus for 3D radiation gel dosimetry*. *Physics in Medicine and Biology*, 2006. **51**: p. 2055-2075.
 41. Pawley, J.B., *Handbook of Biological Confocal Microscopy*. 1995: Plenum Press.
 42. Chalpua, L.M. and J.S. Warner, *Fundamentals of Light Microscopy and Digital Imaging*. 2001, New York: Wiley.
 43. Warger(II), W.C., et al. *Combining Optical Quadrature and Differential Interference Contrast to facilitate embryonic cell counting with Fluorescence Imaging for confirmation*. in *Proceedings of SPIE*. 2005.
 44. Hoeling, B.M., et al., *An optical coherence microscope for 3-dimensional imaging in developmental biology*. *Optics Express*, 2000. **6**(7): p. 136-146.
 45. Yelbuz, T.M., et al., *Optical Coherence Tomography. A New High-Resolution Imaging Technology to Study Cardiac Development in Chick Embryos*. *Circulation*, 2002. **106**(2771 - 2774).
 46. Huisken, J., et al., *Optical sectioning deep inside live embryos by selective plane illumination microscopy*. *Science*, 2004. **305**(5686): p. 1007-9.
 47. Engelbrecht, C.J. and E.H.K. Stelzer, *Resolution enhancement in a light-sheet-based microscope (SPIM)*. *Optics Letters*, 2006. **31**(10): p. 1477 - 1479.

REFERENCES

48. Meyer, H., et al., *Optical Projection tomography for in-vivo Imaging of Drosophila melanogaster*. *Microscopy & Analysis*, 2008. **22**(5): p. 19-22.
49. Boppart, S.A., et al., *Investigation of developing embryonic morphology using optical coherence tomography*. *Dev Biol*, 1996. **177**(1): p. 54-63.
50. Jacobs, R.E. and S.E. Fraser, *Magnetic resonance microscopy of embryonic cell lineages and movements*. *Science*, 1994. **263**(5147): p. 681-4.
51. Louie, A.Y., et al., *In vivo visualization of gene expression using magnetic resonance imaging*. *Nature Biotechnology*, 2000. **18**: p. 321 - 325.
52. Huisken, J. and D.Y. Stainier, *Even fluorescence excitation by multidirectional selective plane illumination microscopy (mSPIM)*. *Opt Lett*, 2007. **32**(17): p. 2608-10.
53. Huisken, J. and D.Y. Stainier, *Selective plane illumination microscopy techniques in developmental biology*. *Development*, 2009. **136**(12): p. 1963-75.
54. Becker, K., et al., *Ultramicroscopy: 3D reconstruction of large microscopical specimens*. *J Biophotonics*, 2008. **1**(1): p. 36-42.
55. Leischner, U., W. Ziegler, and H.U. Dodt, *Resolution of ultramicroscopy and field of view analysis*. *PLoS One*, 2009. **4**(6): p. e5785.
56. Kak, A. and M. Slaney, *Principles of Computerized tomographic imaging*. 1988, New York: IEEE Press.
57. Chen, K., et al., *Optical computed tomography in a turbid medium using early arriving photons*. *J Biomed Opt*, 2000. **5**(2): p. 144-54.
58. Davidson, D. and R. Baldock, *Bioinformatics beyond sequence: mapping gene function in the embryo*. *Nat Rev Genet*, 2001. **2**(6): p. 409-17.
59. Weninger, W.J. and T. Mohun, *Phenotyping transgenic embryos: a rapid 3-D screening method based on episcopic fluorescence image capturing*. *Nat Genet*, 2002. **30**(1): p. 59-65.
60. DeLaurier, A., R. Schweitzer, and M. Logan, *Pitx1 determines the morphology of muscle, tendon, and bones of the hindlimb*. *Developmental Biology*, 2006. **299**: p. 22 -34.
61. Oldham, M., et al., *Three-dimensional imaging of xenograft tumors using optical computed and emission tomography*. *Med.Phys.*, 2006. **33**(9): p. 3193-3202.
62. Caruana, G., R.J. Young, and J.F. Bertram, *Imaging the Embryonic Kidney*. *Experimental Nephrology*, 2006. **103**: p. e62 - e68.
63. Kulandavelu, S., et al., *Embryonic and Neonatal Phenotyping of Genetically Engineered Mice*. *ILAR*, 2006. **47**: p. 103 - 117.

64. Lee, K., et al., *Visualizing Plant Development and Gene Expression in Three Dimensions Using Optical Projection Tomography*. The Plant Cell, 2006. **18**: p. 2145-2156.
65. Bryson-Richardson, R.J., et al., *FishNet: an online database of zebrafish anatomy*. BMC Biology, 2007.
66. Arques, C.G., et al., *Cell tracing reveals a dorsoventral lineage restriction plane in the mouse limb bud mesenchyme*. Development, 2007. **134**: p. 3713 - 3722.
67. Rogers, R.A., *Method for imaging tissue*, R.I. Cooperation, Editor. 2002: United States.
68. Alanentalo, T., et al., *Tomographic molecular imaging and 3D quantification within adult mouse organs*. Nature Methods, 2007. **4**: p. 31 - 33.
69. Asayesh, A., et al., *Spleen versus pancreas: strict control of organ interrelationship revealed by analysis of Bapx1^{-/-} mice*. Genes and Development, 2006. **20**: p. 2208 - 2213.
70. Born, M. and E. Wolf, *Principles of Optics*. 7 ed. 1999, Cambridge: University Press.
71. Wang, Y. and R. Wang, *Imaging using parallel integrals in optical projection tomography*. Physics in Medicine and Biology, 2006. **51**: p. 6023 - 6032.
72. Hawley, S.W., K. Golic, and M. Ashburner, *Drosophila: A Laboratory Handbook* 2ed. 2004: Cold Spring Harbor Laboratory Press. 1330.
73. Groen, F.C.A., I.T. Young, and G. Ligthart, *A comparison of difference focus functions for use in autofocus algorithms*. Cytometry, 1995. **6**: p. 81-91.
74. Metaxakis, A., et al., *Minos as a genetic and genomic tool in Drosophila melanogaster*. Genetics, 2005. **171**(2): p. 571-81.
75. McGurk, L., et al., *Three-Dimensional Imaging of Drosophila melanogaster*. PLoS ONE, 2007(9).
76. Yang, M.Y., et al., *Subdivision of the Drosophila mushroom bodies by enhancer trap expression patterns*. Neuron, 1995. **15**(2): p. 245 - 247.
77. Sulston, J.E. and H.R. Horvitz, *Post-embryonic cell lineages of the nematode Caenorhabditis elegans*. Dev. Biol., 1977. **56**: p. 110-156.
78. Sulston, J.E., et al., *The embryonic cell lineage of the nematode Caenorhabditis elegans*. Dev. Biol., 1983. **100**: p. 64-119.
79. Brenner, S., *The genetics of Caenorhabditis elegans*. Genetics, 1974. **77**: p. 71-94.
80. Tavernarakis, N., et al., *unc-8, a DEG/ENaC family member, encodes a subunit of a candidate mechanically gated channel that modulates C. elegans locomotion*. Neuron, 1997. **18**(1): p. 107-19.

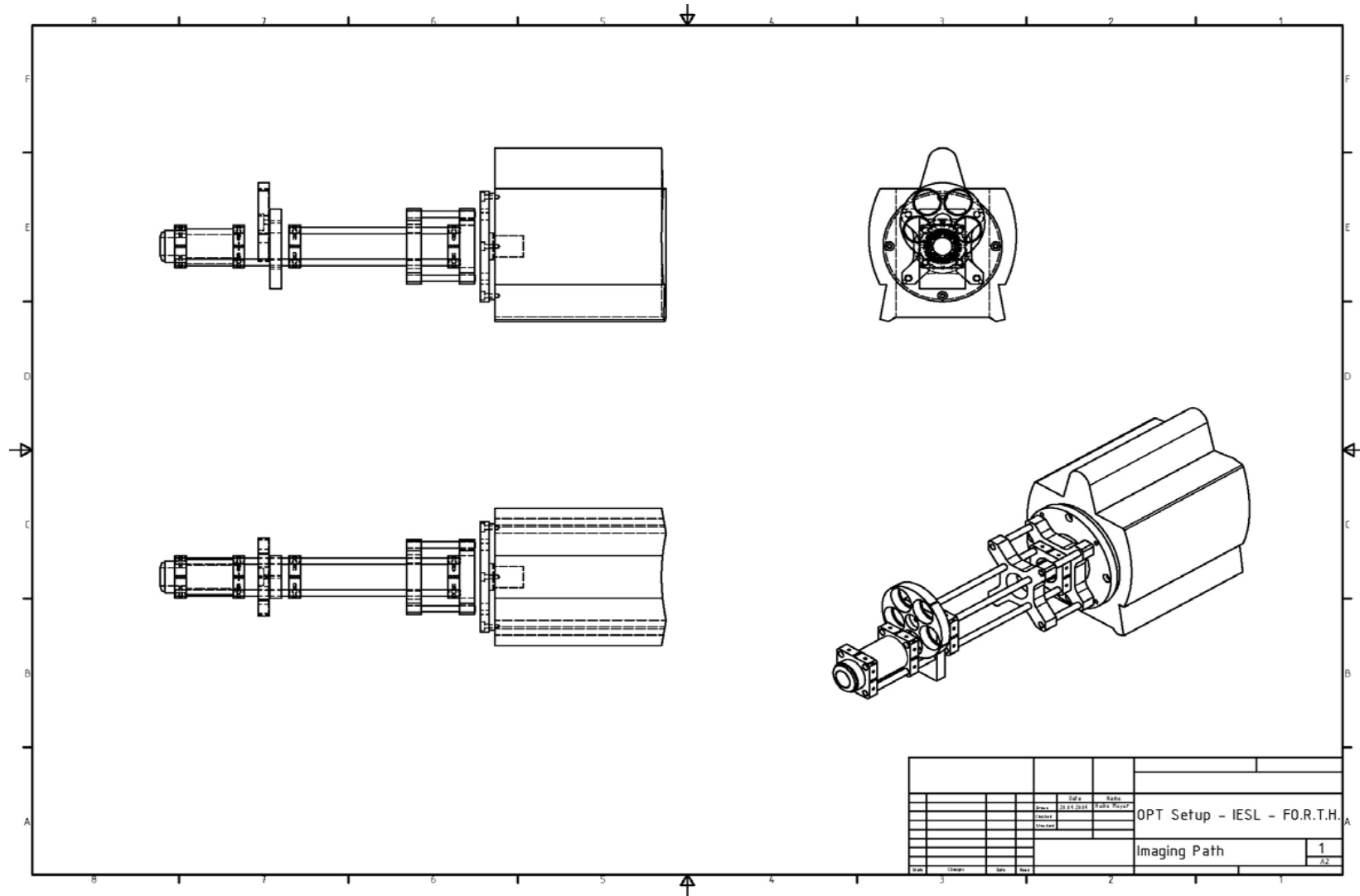
REFERENCES

81. Perens, E.A. and S. Shaham, *C. elegans daf-6 encodes a patched-related protein required for lumen formation*. Dev Cell, 2005. **8**(6): p. 893-906.
82. Averof, M., *Arthropod Hox genes: insights on the evolutionary forces that shape gene functions*. Curr Opin Genet Dev, 2002. **12**(4): p. 386-92.
83. Averof, M. and N.H. Patel, *Crustacean appendage evolution associated with changes in Hox gene expression*. Nature, 1997. **388**(6643): p. 682-6.
84. Pavlopoulos, A. and M. Averof, *Establishing genetic transformation for comparative developmental studies in the crustacean Parhyale hawaiiensis*. Proc Natl Acad Sci U S A, 2005. **102**(22): p. 7888-93.
85. Gerberding, M., W.E. Browne, and N.H. Patel, *Cell lineage analysis of the amphipod crustacean Parhyale hawaiiensis reveals an early restriction of cell fates*. Development, 2002. **129**(24): p. 5789-801.
86. Extavour, C.G., *The fate of isolated blastomeres with respect to germ cell formation in the amphipod crustacean Parhyale hawaiiensis*. Dev Biol, 2005. **277**(2): p. 387-402.
87. Sweet, H.C., M. Gehring, and C.A. Ettensohn, *LvDelta is a mesoderm-inducing signal in the sea urchin embryo and can endow blastomeres with organizer-like properties*. Development, 2002. **129**(8): p. 1945-55.
88. Browne, W.E., et al., *Stages of embryonic development in the amphipod crustacean, Parhyale hawaiiensis*. Genesis, 2005. **42**(3): p. 124-49.
89. Darrell, A., et al., *Improved fluorescence optical projection tomography reconstruction*. Proceedings SPIE, 2008. **Biomedical Optics & Medical Imaging**.
90. Darrell, A., et al., *Accounting for Point Source Propagation Properties in 3D Fluorescence OPT*. IEEE 2006. **International Conference of the Engineering in Medicine and Biology Society (EMBC 2006)**(New York City, New York).
91. Darrell, A., et al., *Weighted filtered backprojection for quantitative fluorescence optical projection tomography*. Phys Med Biol, 2008. **53**(14): p. 3863-81.

BLUEPRINTS

This chapter contains the copyrighted blue prints without indicated dimensions. All here presented work has been designed, manufactured and assembled at the Institute of Electronic Structure and Laser at the Foundation of Research and Technology Hellas. Due to third party copyrights (*i.e. Thorlabs Inc., Edmund Optics, STANDA*), some elements of the illumination path are not represented in the following printouts. For the originals and part lists from third parties, please contact either Heiko Meyer (heimeyer@iesl.forth.gr) or Jorge Ripoll at IESL-FORTH (jripoll@iesl.forth.gr).

BLUE PRINTS



		Date		Name	
		20.04.2018		F0.R.T.H.	
		Drawing		OPT Setup - IESL - F0.R.T.H.	
		Drawing		Imaging Path	
		Scale		1	
		Sheet		A2	

CURICULLUM VITAE

PERSONAL INFORMATION

Name: Heiko
Surname: Meyer
Date of Birth: March 3rd 1974
Nationality: German
Home address: Auf dem Orthe 22
D-31840 Hessisch Oldendorf

Business address: Laser Zentrum Hannover e.V.
Biophotonics Group
Department of Biomedical Optics
Hollerithallee 8
D-30419 Hannover

Tel: +49 511 2788 231
Fax: +49 511 2788 100
e-mail: h.meyer@lzh.de

EDUCATION - TRAINING

Mar. 2008 - Researcher at Laser Zentrum Hannover e.V.,
Biophotonics group
Department of Biomedical Optics

Dec. 2007 – Feb. 2008 Researcher at IESL-FORTH, Biomedical Imaging Group,
Project: In-vivo fluorescence optical projection tomography

Dec. 2004 – Nov. 2007 PhD student at the Erasmus University Rotterdam,
Marie Curie EST fellowship

Jan.2004 – Nov. 2004 Researcher at IESL-FORTH, Biomedical Imaging Group,
Project: Fluorescence Mediated Tomography on small
Animals

Oct.2003 Graduation at University of Applied Sciences, Emden, Germany,
Dipl.Ing. (FH) in Applied Laser Technology.
Graduation at Hanzehogeschool van Groningen, Ing. in
Mechanical Engineering, main subject Medical Product
Development.

Language Skills

German:	Mothers language
English:	Fluently spoken and written
Greek:	some
Spanish:	some

RESEARCH ACTIVITIES

Oct.2003 – Jan.2004	Laboratory Assistant, University of Applied Sciences, Emden Germany
Jan.2004 – Nov.2004	Laboratory Assistant, Biomedical Applications, IESL-FORTH

RESEARCH EXPERIENCE

- Optical characterization of tissue
- Time Resolved Fluorescence Spectroscopy
- Laser Induced Fluorescence Spectroscopy
- Design, Development & Implementation of Optical Imaging Systems

PUBLICATIONS

PARTICIPATION TO CONFERENCES

1. **H. Meyer**, A. Garofalakis, G. Zacharakis, E.N. Economou, C. Mamalaki, S. Papamatheakis, V. Ntziachsitos, J. Ripoll, "*A multi-projection non-contact Tomography setup for imaging arbitrary geometries*", oral presentation, Photonics West, Biomedical Optics (2004), San Jose, CA, USA
2. **H. Meyer**, A. Garofalakis, G. Zacharakis, E.N. Economou, C. Mamalaki, G. Fousteri, D. Kioussis, V. Ntziachsitos, J. Ripoll, "*High resolution fast surface reconstruction for in-vivo small animal imaging*", poster presentation, 4th Annual Meeting of the Society for Molecular Imaging, (2005), Cologne, Germany
3. A. Garofalakis, G. Zacharakis, **H. Meyer**, E.N. Economou, C. Mamalaki, D. Kioussis, V. Ntziachristos, J. Ripoll, "*3D in-vivo imaging of GFP-expressing T-cells in mice with non-contact Fluorescence Molecular Tomography*", poster presentation, 4th Annual Meeting of the Society for Molecular Imaging, (2005), Cologne, Germany
4. G. Zacharakis, A. Garofalakis, **H. Meyer**, E.N. Economou, C. Mamalaki, D. Kioussis, V. Ntziachristos, J. Ripoll, "*3D mapping of Skin Autofluorescence in Whole Animals*", poster presentation, 4th Annual Meeting of the Society for Molecular Imaging, (2005), Cologne, Germany

5. **H. Meyer**, Metaxakis A., Darrell A., Atrops S., Savakis B., Ripoll J., “*3D Imaging of fluorescence patterns in Drosophila melanogaster with OPT*”, poster presentation, 1st International European Society for Molecular Imaging, (2006), Paris, France
6. **H. Meyer**, Metaxakis A., Darrell A., Atrops S., Savakis B., Ripoll J., “*3D Imaging of fluorescence patterns in Drosophila melanogaster with OPT*”, poster presentation, International Symposium Optical Analysis of Biomolecular Machines, (2006), Berlin, Germany

CONTRIBUTION TO CONFERENCE PROCEEDINGS

1. **H. Meyer**, A. Garofalakis, G. Zacharakis, C. Mamalaki, E. N. Economou, “*Multi-projection non-contact fluorescence tomography setup for imaging arbitrary geometries*”, Proceedings of SPIE Volume 5693, pp. 246-254 (2005), Photonics West Meeting, BiOS 2005, San Jose, California, USA
2. **H. Meyer**, A. Garofalakis, G. Zacharakis, E.N. Economou, C. Mamalaki, S. Papamatheakis, V. Ntziachristos, J. Ripoll, “*A multi-projection non-contact Tomography setup for imaging arbitrary geometries*”, Proceedings of SPIE Vol. 5771, 244-251, Saratov Fall Meeting (2004)
3. A. Garofalakis, **H. Meyer**, G. Zacharakis, E.N. Economou, C. Mamalaki, J. Papamatheakis, V. Ntziachristos, J. Ripoll, “*3D in-vivo imaging off GFP-expressing T-cells in mice with non-contact Fluorescence Molecular Tomography*”, Proceedings of SPIE Vol. 5771, 120-129, Saratov Fall Meeting (2004)
4. A. Garofalakis, G. Zacharakis, **H. Meyer**, S. Psycharakis, C. Mamalaki, G. Fousteri, J. Papamatheakis, D. Kioussis, V. Ntziachristos, E. N. Economou, and J. Ripoll, “*Two-Color in vivo Imaging of Fluorescent Cells in Mice*”, in Biomedical Optics, Technical Digest (CD) (Optical Society of America, 2006), paper TuC5.
5. G. Zacharakis, A. Garofalakis, S. Psycharakis, **H. Meyer**, C. Mamalaki, G. Fousteri, J. Papamatheakis, D. Kioussis, V. Ntziachristos, E. N. Economou, and J. Ripoll, “*Autofluorescence Removal from Fluorescence Molecular Tomography Data*”, in Biomedical Optics, Technical Digest (CD) (Optical Society of America, 2006), paper TuG6.

LIST OF PUBLICATIONS

1. K. Marias, J. Ripoll, **H. Meyer**, V. Ntziachristos, and S. Orphanoudakis, “*Image Analysis for Assessing Molecular Activity Changes in Time-Dependent Geometries*”, IEEE Transaction on medical imaging (2005).
2. **H. Meyer**, A. Garofalakis, G. Zacharakis, C. Mamalaki, D. Kioussis, E.N. Economou, V. Ntziachristos & J. Ripoll, “Non-contact Optical Imaging in Mice with Full Angular Coverage and Automatic Surface Extraction”, Applied Optics, (2007).
3. **H. Meyer**, A. Darrell, a. Metaxakis, C. Savakis, J. Ripoll, “ Optical Projection Tomography for In-Vivo imaging of Drosophila melanogaster”, Microscopy & Analysis, (2008)
4. A. Martin, J. Aguirre, A. Sarasa-Renedo, D. Tsoukatou, A. Garofalakis, **H. Meyer**, C. Mamalaki, J. Ripoll, A. M. Planas, “Imaging Changes in Lymphoid Organs In Vivo after Brain Ischemia with Three-Dimensional Fluorescence Molecular Tomography in Transgenic Mice Expressing Green Fluorescent Protein in T Lymphocytes”, Molecular Imaging, (2008)
5. A. Darrell, **H. Meyer**, K. Marias, M. Brady and J Ripoll, “Weighted filtered backprojection for quantitative fluorescence optical projection tomography”, Phys. Med. Bio., 53(14): 3863-81 (2008).
6. J. Ripoll, **H. Meyer**, A. Garofalakis, “In vivo optical tomography: From diffusion to ballistic”, Optical Materials 31, (2009)

PARTICIPATION TO EST COURSES

1. Diagnostic Molecular Imaging (DiMI), “Microscopical research techniques in biomedical applications”, 20/ - 24/03/2006, Antwerp (BELGIUM)